SCUOLA INTERNAZIONALE
SUPERIORE di STUDI AVANZATI
International School
for Advanced Studies

MAGNETIC FIELDS IN PROTO-NEUTRON STARS AND IN ACCRETION DISCS AROUND NEUTRON STARS

Thesis submitted for the degree of
"Doctor Philosophiæ"

15 August 2009

CANDIDATE

Luca Naso

SUPERVISORS

John C. Miller

Alfio Bonanno

Via Beirut 2-4, 34151 Trieste, Italy
E-mail: naso@sissa.it

Provando e riprovando
(motto della Societá Italiana di Fisica)

Contents

Collaborations

The research presented in this thesis was mainly conducted at SISSA in Trieste with Prof. John C. Miller and at the Catania Astrophysical Observatory with Dr. Alfio Bonanno, between November 2005 and August 2009. There was also an important collaboration with Dr. Detlef Elstner of the Potsdam Astrophyscial Institute.

This thesis is the result of my own work, as well as the outcome of the scientific collaborations stated below, except where explicit reference is made to the results of others.

- Chapter 3:
  - Naso L., Rezzolla L., Bonanno A. & Paternò, *Magnetic field amplification in proto-neutron stars – The role of the neutron-finger instability for dynamo excitation*, 2008, A&A, 479, 167 [arXiv:0711.1498 astro-ph]
- Chapter 4:
  - Naso L. & Miller J. C., *Stationary magnetic field configurations in accretion discs around neutron stars – the role of velocity and diffusivity*, submitted [arXiv:0906.5082 astro-ph.SR]
  - Naso L. & Miller J. C., *Stationary magnetic field configurations in accretion discs around neutron stars – II analysis of the toroidal component*, in preparation
- Chapter 5 and 6:
  - Naso L, Bonanno A. & Elstner D., *Magnetic field amplification in proto-neutron stars – a non linear 2-dimensional model for the mean field dynamo*, in preparation

Chapter 1

General introduction

The main characters of this thesis are the magnetic field, the plasma velocity field, the turbulent magnetic resistivity and the numerical codes. They act on two different stages and on two different levels and occasionaly there are other bit players, e.g. the α-effect, the quenching, the differential rotation, the magnetic stream function, the magnetic Reynolds number, the Interactive Data Language and even ZEUS. All of them are led by the same invisible hand with the purpose of understanding better the intricate topic of the magnetic field - plasma relation.

The two stages of the scene could not be more different, in one case everything is done in less than a minute inside a proto-neutron star soon after a supernova explosion, in the other case there is no time evolution at all and an equilibrium configuration is looked for inside a disc of matter spiraling around a neutron star. Nevertheless the same set of equations can describe the behaviour of the characters on both stages, this set is composed of the equations of the electromagnetic field plus the fluid equations.

However knowing that the answers to all of your questions are written inside only one book, does not mean that you are able to read that book ... It is at this moment that the numerical codes come into the scene, offering you a way of translating the book in a language that you know. Unfortunately they like playing tricks and you cannot trust their translations unless you take many precautions every time.

Eventually, after the equations have been solved, comes the art of interpreting the results; a task that might seem quite simple in comparison with the difficulties overcome on the path to get there, but that requires a deep knowledge of what has already been done and a good intuition about what can possibly happen later on.

We do not presume to have made big leaps forward in the process of understanding the behaviour of the magnetic field in the cases considered here, nonetheless thanks to our simplified models we were able to grasp the fundamental aspects of the phenomena being considered, to gain some insights and to propose new falsifiable ideas. At the same time we have also developed new tools for making our models more elaborate and realistic. Therefore we expect to find even more characters in the future Chapters of this

analysis, but that is another story, and will be told another time.

1.1 Mean field dynamo

The first of the two stages where we see the magnetic field in action is inside proto-neutron stars, in the ambit of the mean field dynamo theory.

Literally a dynamo is a generator of direct current, which exploits the mechanical motion of a conductor immersed in a magnetic field to generate an electric current via Faraday's law of induction, according to which the induced electromotive force in any closed circuit is equal to the time rate of change of the magnetic flux through the circuit.

In the astrophysical context one speaks of a dynamo if a magnetic field is generated or maintained due to motions inside an electrically conducting fluid medium. Therefore the dynamo is considered as a means of converting kinetic energy into magnetic energy, and according to the kind of motions which are activating the dynamo one has laminar or turbulent dynamos.

We shall consider here only turbulent dynamos, which we approach by direct numerical simulations in the ambit of mean field theory. When a dynamo is active and the magnetic field is growing, it inevitably continues to grow as long as the motions remain unchanged. In reality however the motions are influenced by the Lorentz force which appears as a consequence of the magnetic field. As long as the magnetic field is sufficiently weak this influence may be neglected. If the field becomes stronger this influence will be of crucial importance. It prevents the incessant increase of the field and determines its magnitude in the final state. In the kinematic dynamo model the motions are kept fixed, therefore the back-reaction of the magnetic field on to the motions is neglected. Kinematic models are usually appropriate for studying the onset of the dynamo, while they cannot provide useful information about the final intensity of the magnetic field. However it is possible to include a quenching function which has the scope of mimicking the saturation effect which is naturally provided by the magnetic feedback on the fluid motion, thus allowing for following the magnetic field evolution until it saturates. This is exactly what is done here, in fact we are interested in knowing the magnetic field intensity at the birth of the neutron star, and in order to estimate this we simulate a mean field dynamo inside the star just before it becomes a neutron star, i.e. when it is a proto-neutron star.

A proto-neutron star is a transient phase that a star undergoes after it has been produced in a supernova explosion and before it becomes a stable neutron star. It is a very swift transition lasting about a minute, during which the star cools very rapidly, mainly radiating away neutrinos, and shrinks, reaching the final size of the neutron star (about 10 km radius). During this phase the inside of the star is thought to be subject to two hydrodynamical instabilities that can generate some turbulence, the convective instability and the neutron finger instability. Therefore this environment is particularly suitable for the onset of a dynamo action, which requires a conductive medium and an electromagnetic field.

Thompson and Duncan (1993) studied the evolution of the magnetic field in the pres-

ence of only the convective instability, and they found that a small scale dynamo is activated. Bonanno et al. (2003) considered instead the case of the neutron finger instability: in this case a mean field dynamo can be excited and therefore a large scale field can be produced. In essence the reason why one instability generates one kind of dynamo and the other instability generates another type, is the time scale of the turbulent eddies. When it is comparable to the spin period of the star then it is possible to have some kind of interaction between the two different scales: the small one of the turbulence and the large one of the rotating star. The main consequence of this interaction is that the turbulence will lose mirror symmetry because of the Coriolis force, and produce the so-called α-effect. In Chapter 2, Section 2.3, we write explicitly the equations that describe this interaction.

Our interest is in continuing the analysis of the mean field dynamo generated in the neutron finger unstable region. Our approach is to begin with a one dimensional model and take advantage of this simplification in order to include some physical ingredients previously neglected. We in fact include the treatment of the α- and η- quenching and we also allow the neutron finger instability to vary its size with time.

In the next act of this analysis we use a two dimensional (axisymmetric) model. The greater modification is in the numerical part of the work. In the first model, the one presented here, we have used a code designed for solving the induction equation in one dimension and in the kinematic approximation, while for the future we would like to have something that allows us not only to use more dimensions and but also to solve the fluid equations as well. In order to achieve this goal we have decided not to write a brand new code, but to start from a publically available one and add to it the bits that are necessary for our purposes. Our choice is to use the ZEUS-MP code, and modify it in such a way that it can solve not only ideal magnetohydrodynamics (MHD), but also resistive MHD in the mean field theory.

All of these steps and successive models have the same final aim, which is that of understanding better the magnetic field that neutron stars have at birth. Although neutron stars were originally discovered as pulsars (bright pulsating radio sources), isolated neutron stars have now been observed across the entire electromagnetic spectrum, up to high-energy gamma-rays. They exhibit a phenomenology so complex and diversified that there is a zoo of different classes: standard radio pulsars, rotating radio transients, soft gamma repeaters and anomalous X-ray pulsars (these two classes are the so-called magnetars since they are supposed to host an hyper-magnetized neutron star), central compact objects in supernova remnants (suggested to be antimagnetars, i.e. low-magnetized neutron stars) and X-ray dim isolated neutron stars. It is presently unknown whether the phenomenology we observe in these different sources and our classification thereof, reflects differences in intrinsic properties (for example progenitors with different masses, or different spin periods and/or magnetic field strengths at the NS birth) or an evolutionary process. We aim at solving a part of this challenge, the one regarding the magnetic field intensity and configuration, and we already have a suggestion that it could be possible to reproduce all of the observed values for the intensity of the magnetic fields (from those of low magnetized to hyper magnetized neutron stars, i.e. from

the anti-magnetars to magnetars) just by assuming a difference in the Reynolds dynamo numbers during their formation. Can this really be a universal scenario? And can it account also for the magnetic field topology? This is the main legacy that this thesis work is leaving us: more questions to be answered with more realistic models.

1.2 Accretion disc

The second scene of action is an accretion disc around a magnetised neutron star.

An accretion disc is nothing more than a collection of matter gravitationally bound around a central object and, because of the large angular momentum, the matter takes the disc-like form. In addition this matter is spiraling inwards, eventually accreting onto the central object. Finally the matter can also have some velocity along the direction perpendicular to the disc and if it leaves the disc it is said to form a wind.

Accretion discs are ubiquitous in the universe. They regulate the energy generation and angular momentum transport in stellar and proto-stellar systems and in active galactic nuclei. It is now generally accepted that magnetic fields play a pivotal role in the accretion-disc physics. Microscopically, they generate turbulence via magneto-rotational instability (MRI), and the turbulence in turn drives the accretion process. Macroscopically, they may determine the flow dynamics, modify the accretion geometry and provide a means to collimate the jet outflows. They also affect the radiative processes, leading to a variety of observational phenomena, such as radiation collimation (pulsar lighthouse effect) and spectral line production through cyclotron and synchrotron emission.

We shall consider here only accretion discs around neutron stars, which are taken to have a dipolar magnetic field. In this case the matter in the disc is in the plasma state and the magnetic field-plasma interaction can be described by the MHD equations. As for the isolated neutron stars, there is a plethora of accreting neutron stars and we investigate the roles of magnetic fields in the accretion of X-ray pulsars and old neutron stars. The primary objective is to resolve a long standing issue, that is, how are accreting neutron stars spun up to become millisecond pulsars? In addition, I also aim to explain the puzzling observation that no neutron star has been found to rotate with an spin-angular velocity near the break-off limit. In both cases it is essential to know the magnetic field configuration and the disc-geometry.

Shakura & Sunyaev developed in 1973 a model for non-magnetised accretion discs which is now considered as a standard model, usually called the α disc model, because the $r\,\phi$ component of the viscous tensor is taken to be proportional to the total pressure with proportionality constant α. There is no standard model for magnetised accretion discs, although the subject has been deeply studied since Ghosh & Lamb (1979). When the magnetic field was at first included in the accretion disc models it was not even sure whether it was able to penetrate the disc or not, because of the generation of screening currents on the surface of the disc. Ghosh and Lamb (1979a) pointed out that there are at least three physical processes preventing the magnetic field being completely shielded by the accretion disc: magnetic reconnection, turbulent magnetic diffusion and the Kelvin–

Helmholtz instability. Ghosh and Lamb divided the disc into two main subregions: an interaction region, where the disc is threaded by the magnetic field, and an external region, which is instead completely shielded from the magnetic field. The interaction region is furthermore divided into two parts: a boundary layer at the inner edge of the disc, where the magnetic field is overwhelming the viscous force and matter leaves the disc vertically; and a broad transition zone, where, even if the magnetic field is present, the accretion flow is similar to the standard α-disc.

In addition to considering the magnetic field configuration, Ghosh and Lamb also addressed the issue of the spin history of the central neutron star. In fact the magnetic connection between the star and the disc in the interaction region generates a magnetic torque acting on the star, that can be spun-up or even spun-down according to the position of the inner edge of the disc, the spin of the star and the intensity of the magnetic field. The main uncertainty in the calculation for the magnetic torque is in the toroidal component. Wang (1987) and Campbell (1987) added important pieces to the puzzle of the magnetic field configuration inside the disc. They found an analytic expression for the toroidal component of the magnetic field by using the induction equation. Because of its simplicity and plausibility, this expression is still used nowadays, although it was obtained in a very simplified case. Nevertheless it still remains the result of a toy-model and we would like to improve this model in order to produce a more accurate expression for all of the components of the magnetic field.

At the same time we want our model to remain simple enough to let us understand the physics of this complex system. Including all of the ingredients, in fact, can indeed produce a better phenomenological description of the particular setup under examination, but will make it very hard to understand the role played by the various physical quantities and consequently will fail to predict what can happen for a setup different from the one studied. In our model we assume that the neutron star magnetic field is a simple dipole, whose axis is aligned with the rotation axis, and that the fluid flow is steady and has axial symmetry everywhere. At the same time we also include a coronal layer on the top and bottom surface of the disc, a non-zero radial velocity, a wind starting from the surface of the disc and a non-constant turbulent magnetic diffusivity. Within this two dimensional model the induction equation is solved without making any vertical integration or leading order expansion.

The results of the numerical simulations indicate that the fields are increasingly distorted and deviate away from a dipolar structure when the radial infall velocity increases. The distortion is, however, suppressed if the turbulent magnetic diffusivity increases. Generally, the field distortion may be characterized using the magnetic Reynolds number $R_{\rm m}$, which specifies how far flux freezing is achieved and how much the field is being dragged by the plasma motion. In accretion discs the radial motion is usually many orders of magnitude smaller than the azimuthal motion, and for this reason two magnetic Reynolds numbers should be used to better characterize the magnetic field–plasma interaction in the two directions. Because of the complexities in the system and the large dynamical ranges in the magnetic diffusivity and flow velocity through the accretion disc, using a single value $R_{\rm m}$ is insufficient to describe the process even along the ra-

dial direction only. To overcome this, we introduce a magnetic distortion function $D_{\rm m}$, which is more general than the magnetic Reynolds number as it takes into account the local properties of the system dynamics and kinematics. Field distortion is more severe in regions where $D_{\rm m} \ll 1$, and vice versa.

In order to complete these analyses, the toroidal magnetic field has to be calculated. With all of the components of the magnetic field determined, the magnetic energy, pressure and torque, and hence the location of the inner edge of the accretion disc will be calculated. In this way it will be possible to address the issue of the spin history of the accreting neutron star.

Future analysis will be oriented to including within the model the magnetic feedback on the velocity field. We plan to do this by coupling the numerical code used in these analyses with a purely hydro code, properly modified with the inclusion of the Lorentz force. We will employ an iterative approach. The modified hydro code will be used to obtain a stationary accretion flow consistent with the Lorentz force term obtained in the earlier stage of the magnetic-field structure analysis. The resulting new velocity field of the flow will then be used to calculate again the magnetic field configuration and hence the Lorentz force. The results will then be used as the inputs for the next iterative calculations.

All of this work is focused on obtaining self-consistent stationary solutions. As a successive development, the stability of the field configuration can be investigated by means of a time-dependent calculations using the ZEUS-MP code, which can also be used to probe the outflow process in more detail.

1.3 Numerics

Both in the context of dynamos and of accretion discs the magnetic diffusivity cannot be neglected and one has to abandon the ideal magneto-hydrodynamics (MHD) in favour of the so called resistive MHD. In the kinematic approximation one does not need to consider all of the MHD equations in order to describe the interaction of the magnetic field with the plasma, but one considers only the induction equation, as obtained from Maxwell's equation and Ohm's law, or the mean induction equation, which is used in the mean field approach and contains the turbulent electromotive force and the turbulent magnetic diffusivity.

It is now time to introduce the last of the main characters of this thesis: the numerical codes. We have presented them as the translators at the beginning of the Chapter and as a matter of fact we have used fortran90 to develop new, purpose-built codes, in order to solve the equations we are interested in. This part of the work has been done on a different level from the previous ones. For developing our codes in fact we have abandoned the field of Physics in favour of the field of Numerics, where we do not try to understand why an X-ray pulsar can be spun up and down, or why a neutron star can have a magnetic field of a certain intensity and topology, but instead we focus on how to discretize the equations, which time step to use, how to handle the data, how to im-

plement the boundary conditions, how to increase the efficiency, how to reduce the wall clock time, how to solve bug number 1, number 2, ... number i, ..., number N, which program to use for visualizing the final solution, how to store the data for improving the visualization process, ...

The induction equation consists of three (scalar) partial differential equations (pdes) of second order and of mixed type. In order to solve these equations the numerical codes exploit a finite difference technique, approximating the operators by discretizing the functions over a grid with the FTCS scheme (Forward-in-Time and Centered-in-Space) for simulating the dynamo in PNSs and with the Gauss-Seidel relaxation method for the case of accretion discs (in this case the equation to be solved is an elliptic pde). Both codes have been carefully checked for stability, convergence and accuracy. Tests against known results have also been performed whenever possible.

For studying more advanced models we have decided to use the publically available ZEUS-MP code. This is the latest addition to the ZEUS line of community application codes developed by the Laboratory for Computational Astrophysics (LCA) of the National Center for Supercomputing Applications (NCSA) at the University of Illinois. The MP suffix denotes the multi-physics, massively parallel, and message passing aspects of the code. The physics suite in this release of ZEUS-MP includes gas hydrodynamics, ideal MHD, flux-limited radiation diffusion, self gravity, and multispecies advection. Since it cannot solve the resistive MHD equations, we have worked on an extension of this code in order to include both the magnetic diffusivity and the mean electromotive force. This has required, and still does require, careful work on some subroutines of the ZEUS code, especially on that for the boundary conditions. In fact, boundary conditions are not imposed on the magnetic fields but on the electric fields, which contain the new terms that we want to include in the code (i.e. the α effect and the magnetic diffusivity). Moreover, since we want the code to work also in spherical coordinates, we have to deal with boundary conditions imposed on the rotation axis of the star as well.

At present the modified version of the code is able to solve properly the mean induction equation for PNSs in axisymmetric models. We aim to include also the third dimension so that the axisymmetry assumption can be released, and a lot of other problems can be addressed (e.g. the case of a magnetic dipole non-aligned with the rotation axis). And successively we want to switch the fluid equations on, so as to release also the kinematic approximation and avoid the use of quenching functions.

Bibliography

[1] Bonanno A., Rezzolla L., & Urpin V. 2003, A&A 410, L33

[2] Campbell C.G., 1987, MNRAS, 229, 405

[3] Ghosh P. & Lamb F.K. 1979, ApJ, 232, 259

[4] Ghosh P. & Lamb F.K. 1979, ApJ, 234, 296

[5] Shakura N.I. & Sunyaev R.A. 1973, A&A, 24, 337

[6] Thompson C. & Duncan R. 1993, ApJ 408, 194

[7] Wang Y.-M. 1987, A&A, 183, 257

Chapter 2

Magnetohydrodynamics equations

The word magnetohydrodynamics (MHD) is derived from "magneto" meaning magnetic field, "hydro" meaning water, but used to mean fluid in general, and "dynamics" meaning movement. It refers to the academic discipline which studies the dynamics of electrically conducting fluids. When such fluids are threaded by a magnetic field, an additional force is present with respect to those considered in the ambit of hydrodynamics: the Lorentz force. Because of this force, a magnetic pressure and a magnetic tension appear in the Euler equation describing the motion of the fluid. Also, at the same time the configuration of the magnetic field feels the presence of the fluid and is consequently modified.

The full set of MHD equations consists of the fluid equations (equation of motion, continuity equation and energy equation), the equations for the electromagnetic field (Maxwell's equations and Ohms' law) and some closure equations (equation of state and equation for the viscous stress tensor).

All of the analyses presented in this thesis have been made within the kinematic approximation, i.e. the velocity field is supposed not to change in time or in response to the magnetic field and only the modifications induced by the fluid motion on the magnetic field are considered. In the case of the mean field dynamo in proto-neutron stars, we have solved the induction equation (this equation will be derived later in this Chapter) to study the time evolution of an initial magnetic field when the star is differentially rotating; in the case of accretion discs around magnetised neutron stars, the induction equation is used to find a stationary configuration of the magnetic field for a given velocity profile of the matter in the disc.

Our main interest is therefore in the induction equation and for this reason the major part of this Chapter is devoted to this equation. However, for the sake of completeness, in the last Section we give the full set of the MHD equations, including also the equations that are not solved in the kinematic approximation.

2.1 The MHD assumptions

In order for interaction between the electromagnetic field and the fluid to be relevant, the fluid has to be an electrically conducting one. In many astrophysical environments (including the ones which we are treating in this work) the matter is in the plasma state. Plasma is the fourth state of matter. It is a partially ionized gas, in which a certain proportion of electrons are free rather than being bound to an atom or molecule. The ability of the positive and negative charges to move somewhat independently makes the plasma electrically conductive so that it responds strongly to electromagnetic fields. A more rigorous definition can be given in terms of the following three criteria that characterize matter in the plasma state:

1. Quasi neutrality: $\lambda_{\mathrm{D}} \ll L$
   Even if electrons are free to move, the distance over which significant charge separation can occur (the Debye screening length, λ_{D}) is much smaller than the physical size of the plasma, L. This also means that interactions in the bulk of the plasma are more important than those at its edges, where boundary effects may occur;

2. Collective interactions: $\Lambda \gg 1$
   Charged particles must be close enough so that each particle influences many nearby charged particles, rather than just interacting with the closest particle. This condition is met when the number of charge carriers within the sphere of influence (i.e. a sphere whose radius is the Debye screening length) is much larger than unity so as to provide collective behaviour of the charged particles. The average number of particles in the Debye sphere is given by the plasma parameter Λ;

3. Electromagnetic forces: $\sigma_{\mathrm{ei}} \gg \sigma_{\mathrm{en}}$
   Free electrons in a plasma can interact both with ions and with neutral atoms. In order for the charged particle dynamics to be governed by electromagnetic forces rather than hydrodynamic ones, the rate of electron-ion collisions, with cross section σ_{ei}, has to be much larger than electron-neutral collisions, with cross section σ_{en}.

To completely describe the state of a plasma, one would need to write down all of the particle locations and velocities, and describe the electromagnetic field in the plasma region. However, it is neither practical nor necessary (generally) to keep track of all of the particles in a plasma, and two main approaches have been developed that do not require this level of detail: the kinetic model and the fluid model.

Kinetic models describe the particle velocity distribution function at each point in the plasma, and therefore do not need to assume any particular distribution, e.g Maxwell–Boltzmann. A kinetic description is often necessary for collisionless plasmas. There are two common approaches to the kinetic description of a plasma. One is based on representing the smoothed distribution function on a grid in velocity and position space. The other, known as the particle-in-cell (PIC) technique, includes kinetic information by following the trajectories of a large number of individual particles. Kinetic models are

generally more computationally intensive than fluid ones. The Vlasov equation may be used to describe the dynamics of a system of charged particles interacting with an electromagnetic field.

Fluid models describe plasmas in terms of smoothed quantities like density and averaged velocity around each position. MHD is a fluid model and treats the plasma as a fluid governed by a combination of electromagnetic equations and modified fluid Navier–Stokes' equations. A more general description considers the plasma as being composed of two fluids, where ions and electrons are described separately. Fluid models are accurate when collisionality is sufficiently high to keep the plasma velocity distribution close to a Maxwell-Boltzmann distribution, and when the mean free path of collisions is much smaller than any characteristic length scale of the fluid (e.g. the Larmor radius).

In the remainder of this thesis we will always assume that the matter is in the plasma state (both inside proto-neutron stars and in the accretion discs) and we will follow the MHD fluid model to describe the interaction between the electromagnetic field and the plasma.

2.2 The induction equation

The induction equation is a vector equation which relates the time evolution of the magnetic field with the properties of the fluid under consideration, in terms of velocity and conductivity. It can easily be derived from Maxwell's equations and Ohm's law.

First of all, we consider Maxwell's equations in their differential form (in SI units):

$$\nabla \cdot \mathbf{B} = 0 \tag{2.1}$$

$$\nabla \cdot \mathbf{E} = \frac{\rho_e}{\epsilon} \tag{2.2}$$

$$\nabla \times \mathbf{B} = \mu \mathbf{J} + \mu \epsilon \partial_t \mathbf{E} \tag{2.3}$$

$$\nabla \times \mathbf{E} = -\partial_t \mathbf{B} \tag{2.4}$$

where $\mathbf{B}$ is the magnetic flux density (usually referred to simply as the magnetic field), $\mathbf{E}$ is the electric field, $\mathbf{J}$ is the current density, μ is the permeability and ϵ is the permittivity.

We consider also the standard Omh's law in a fixed frame of reference:

$$\mathbf{J} = \sigma(\mathbf{E} + \mathbf{v} \times \mathbf{B}) \tag{2.5}$$

where $\mathbf{v}$ is the fluid velocity field and σ is the electric conductivity.

The first step in the derivation is to show that for non relativistic flows the Faraday displacement current in equation (2.3) can be neglected. For doing this we note that the interaction between the electromagnetic field and the fluid velocity field is important only when the ratio between the characteristic length scale of the electromagnetic field, L, and its characteristic time of variation, τ, is comparable to the characteristic velocity of

a generic fluid element, v, i.e. when:

$$\frac{L}{\tau} \sim v \tag{2.6}$$

From equation (2.4) it follows that:

$$\frac{E}{L} \sim \frac{B}{\tau} \tag{2.7}$$

and so the above condition gives:

$$\frac{E}{B} \sim v \tag{2.8}$$

Consider now equation (2.3) and take the ratio between the left- hand side and the second term on the right-hand side:

$$\frac{\nabla \times \mathbf{B}}{\epsilon\mu\partial_t \mathbf{E}} \sim \frac{B/L}{E/c^2\tau} \sim \frac{B}{E}\frac{\tau}{L}c^2 \tag{2.9}$$

which inserting (2.6) and (2.8) gives:

$$\frac{\nabla \times \mathbf{B}}{\epsilon\mu\partial_t \mathbf{E}} \sim \frac{c^2}{v^2} \tag{2.10}$$

Therefore in the non-relativistic regime ($v \ll c$) the Faraday displacement current always gives a negligible contribution and equation (2.3) can be replaced by the following one:

$$\nabla \times \mathbf{B} = \mu\mathbf{J} \tag{2.11}$$

The same result can also be obtained in another way. Consider equation (2.3) and eliminate **J** by using Ohm's law (2.5):

$$\nabla \times \mathbf{B} \quad = \quad \mu\sigma\mathbf{E} + \mu\sigma(\mathbf{v} \times \mathbf{B}) + \frac{1}{c^2}\partial_t \mathbf{E} \tag{2.12}$$

Re-arranging then gives

$$\mathbf{E} + \frac{1}{\mu\sigma}\frac{1}{c^2}\partial_t \mathbf{E} \quad = \quad \frac{1}{\mu\sigma}\nabla \times \mathbf{B} - \mathbf{v} \times \mathbf{B} \tag{2.13}$$

and

$$\mathbf{E} + \frac{\eta}{c^2}\partial_t \mathbf{E} \quad = \quad \eta\nabla \times \mathbf{B} - \mathbf{v} \times \mathbf{B} \tag{2.14}$$

where we have introduced the magnetic diffusivity $\eta \equiv 1/\mu\sigma$ in the last line. The time derivative term on the left-hand side of equation (2.14) can be neglected when the Fara-

day time, $\tau_{\rm Far} \equiv \eta/c^2$, is smaller than the characteristic time for the electromagnetic field variation τ. For the cases considered in this thesis, η ranges between 10^{11} cm^2/s and 10^{14} cm^2/s, and so $\tau_{\rm Far} \sim 10^{-11} - 10^{-7}$ s, while τ is of the order of a second for the mean field dynamo in proto-neutron star and can be as small as 10^{-3} s for accretion flows onto compact objects. Therefore the condition $\tau_{\rm Far}/\tau \ll 1$ is always satisfied.

In order to proceed further and to express the time evolution of the magnetic field in terms of the fluid properties we combine equations (2.4), (2.5) and (2.11). We first substitute **J** in equation (2.11) with the expression given in equation (2.5) to obtain:

$$\nabla \times \mathbf{B} = \mu\sigma(\mathbf{E} + \mathbf{v} \times \mathbf{B}) \tag{2.15}$$

Re-arranging then gives:

$$\mathbf{E} = \frac{1}{\mu\sigma}\nabla \times \mathbf{B} - \mathbf{v} \times \mathbf{B} \tag{2.16}$$

and then we put this expression for **E** into equation (2.4) to get the induction equation:

$$\partial_t \mathbf{B} = \nabla \times (\mathbf{v} \times \mathbf{B}) - \nabla \times (\eta \nabla \times \mathbf{B}) \tag{2.17}$$

With this equation it is possible to calculate the time evolution of an initial magnetic field **B**, which is threading a fluid characterized by a velocity field **v** and a magnetic diffusivity η.

There are two main evolutionary scenarios, according to which term predominates on the right-hand side of equation (2.17). The ratio of these two terms defines the magnetic Reynolds number:

$$\mathrm{R_m} \equiv \frac{\nabla \times (\mathbf{v} \times \mathbf{B})}{\nabla \times (\eta \nabla \times \mathbf{B})} = \frac{v_0 \cdot l_0}{\eta_0} \tag{2.18}$$

where v_0, l_0 and η_0 are respectively a characteristic velocity, length and diffusivity of the system under consideration.

When $\mathrm{R_m} \gg 1$ the induction equation reduces to:

$$\partial_t \mathbf{B} \approx \nabla \times (\mathbf{v} \times \mathbf{B}) \tag{2.19}$$

and under these circumstances, i.e. vanishing resistivity (this regime is called ideal MHD), the magnetic flux through a surface moving with the fluid remains constant (Alfven frozen-flux theorem). This means that the magnetic field lines are frozen into the fluid, in the sense that any motion orthogonal to the field lines is prohibited. This is the reason why the connection between magnetic field lines and the fluid in ideal MHD fixes the topology of the magnetic field in the fluid.

In the opposite regime, $\mathrm{R_m} \ll 1$, the induction equation reduces to:

$$\partial_t \mathbf{B} \approx -\nabla \times (\eta \nabla \times \mathbf{B}) \tag{2.20}$$

$$= \eta \nabla^2(\mathbf{B}) \tag{2.21}$$

where to go from equation (2.20) to (2.21) we have assumed η to be constant in space and we have used the vectorial identity: $\nabla \times (\nabla \times \mathbf{C}) = -\nabla^2 \mathbf{C} + \nabla(\nabla \cdot \mathbf{C})$, which holds for any vector $\mathbf{C}$. In this regime the time evolution of the magnetic field is just a diffusion with diffusion coefficient η.

2.3 Mean field induction equation

When the fluid is characterized by a turbulent motion then the fields considered up to now will vary irregularly in space and time. One of the possible ways to treat this situation is to use mean field theory. Within this theory a generic fluctuating field $\mathbf{F}$, considered as a random function, has a corresponding mean field, $\overline{\mathbf{F}}$, that is defined as the expectation value of $\mathbf{F}$ in an ensemble of identical systems, and $\mathbf{F}'$ is used to denote the difference between the fluctuating field and its mean component. The following relations, the Reynolds relations, hold:

$$\mathbf{F} = \overline{\mathbf{F}} + \mathbf{F}', \quad \overline{\overline{\mathbf{F}}} = \overline{\mathbf{F}}, \quad \overline{\mathbf{F}'} = 0, \tag{2.22}$$

$$\overline{\mathbf{F} + \mathbf{G}} = \overline{\mathbf{F}} + \overline{\mathbf{G}}, \quad \overline{\overline{\mathbf{F}}\,\overline{\mathbf{G}}} = \overline{\mathbf{F}}\,\overline{\mathbf{G}}, \quad \overline{\overline{\mathbf{F}}\mathbf{G}'} = 0 \tag{2.23}$$

where $\mathbf{G}$ is another fluctuating field. The averaging operator commutes with the differentiation and integration operators in both space an time, i.e. for the differentiation:

$$\overline{\partial_t \mathbf{F}} = \partial_t \overline{\mathbf{F}}, \quad \overline{\partial_{x_i} \mathbf{F}} = \partial_{x_i} \overline{\mathbf{F}}. \tag{2.24}$$

Instead of averaging over an ensemble, we may also define mean values by integration over space or time. Some of the Reynolds relations are then only approximate, although they will be the more accurate the less the means vary over the considered integration range.

In the derivation of the mean field induction equation we shall not need to refer to the nature of the averaging operation, but only to the properties (2.22)-(2.23) and to the commutation rules just mentioned. Firstly we have to use these relations to write Maxwell's equations and Ohm's law for the mean fields. For Maxwell's equations, we find that they have the same form as for the total fields, and one just has to substitute the fields with their mean components. For Ohm's law instead we obtain an additional term:

$$\overline{\mathbf{J}} = \sigma(\overline{\mathbf{E}} + \overline{\mathbf{v}} \times \overline{\mathbf{B}} + \overline{\mathbf{v}' \times \mathbf{B}'}) \tag{2.25}$$

The additional term:

$$\overline{\mathcal{E}} \equiv \overline{\mathbf{v}' \times \mathbf{B}'} \tag{2.26}$$

is the mean (or turbulent) electromotive force. Once Maxwell's equations and Ohm's law for mean fields are at hand, one can proceed as done in the previous section and derive the induction equation for mean fields:

$$\partial_t \overline{\mathbf{B}} = \nabla \times \left(\overline{\mathbf{v}} \times \overline{\mathbf{B}}\right) + \nabla \times \left(\overline{\mathcal{E}}\right) - \nabla \times \left(\eta \nabla \times \overline{\mathbf{B}}\right) \tag{2.27}$$

Finding an expression for $\overline{\mathcal{E}}$ in terms of the mean fields is a standard closure problem which is at the heart of mean field theory. One generally assumes that $\overline{\mathcal{E}}$ can be expanded in powers of the gradients of the mean magnetic field. This suggests the rather general expression:

$$\overline{\mathcal{E}}_i = \alpha_{ij}(\dots)\overline{\mathbf{B}}_j + \eta_{ijk}(\dots)\partial_{x_k}\overline{\mathbf{B}}_j + \dots \tag{2.28}$$

where the tensor components α_{ij} and η_{ijk} are referred to as turbulent transport coefficients. They depend on the stratification, angular velocity, and mean magnetic field strength. They may also depend on correlators involving the small scale magnetic field, for example the current helicity of the small scale field.

The simplest way of calculating the turbulent transport coefficients is the first order smoothing approximation (FOSA), which consists of linearizing the equations for the fluctuating quantities and ignoring quadratic terms that would lead to triple correlations in the expressions for the quadratic correlations.

In the FOSA one considers the induction equation for the fluctuating part of the magnetic field, which is obtained by taking the difference between the induction equation for the total fields (2.17) and the one for the average fields (2.27). Successively this equation is linearized and some additional terms are neglected by assuming that the magnetic Reynolds number is small or that the correlation time $\tau_{\rm cor}$ of the turbulence is small with respect to that associated to the total random field $\mathbf{v}$. Then this simplified equation is integrated to get $\mathbf{B}^{'}$, and the average of the cross product with $\mathbf{v}^{'}$ is calculated to get $\overline{\mathcal{E}}$, following equation (2.29). If one finally assumes that the turbulence is isotropic and not mirrorsymmetric[1], and that $\overline{\mathbf{B}}$ is a slowly varying function of time, one eventually obtains:

$$\overline{\mathcal{E}} = \alpha \overline{\mathbf{B}} - \eta_t \nabla \times \overline{\mathbf{B}} \tag{2.29}$$

where the pseudo-scalar α and the scalar $\eta_{\rm t}$ are given by:

$$\alpha = -\frac{1}{3}\int_0^t \overline{\mathbf{v}^{'}(t)\cdot\omega^{'}(t^{'})}dt^{'} \approx -\frac{1}{3}\tau_{\rm cor}\overline{\mathbf{v}^{'}\cdot\omega^{'}} \tag{2.30}$$

$$\eta_{\rm t} = \frac{1}{3}\int_0^t \overline{\mathbf{v}^{'}(t)\cdot\mathbf{v}^{'}(t^{'})}dt^{'} \approx \frac{1}{3}\tau_{\rm cor}\overline{\mathbf{v}^{'2}} \tag{2.31}$$

where $\omega^{'} \equiv \nabla \times \mathbf{v}^{'}$ is the helicity of the velocity fluctuations.

[1] A turbulent field is said to be mirror-symmetric if the mean quantities derived from it are invariant if the field is reflected in an arbitrary plane.

The mean field induction equation can then be written as:

$$\partial_t \overline{\mathbf{B}} = \nabla \times \left(\overline{\mathbf{v}} \times \overline{\mathbf{B}}\right) + \nabla \times \left(\alpha \overline{\mathbf{B}}\right) - \nabla \times \left(\eta_{\mathrm{T}} \nabla \times \overline{\mathbf{B}}\right) \tag{2.32}$$

where $\eta_{\mathrm{T}} = \eta + \eta_{\mathrm{t}}$. Generally the turbulent magnetic diffusivity is much larger than the standard diffusivity and $\eta_{\mathrm{T}} \approx \eta_{\mathrm{t}}$.

In comparison with the standard induction equation (2.17), the one for mean fields (2.32) has a new term: $\nabla \times \left(\alpha \overline{\mathbf{B}}\right)$. In the derivation of this term the assumption of non-mirrorsymmetry is crucial. In fact, suppose that the velocity field is mirrorsymmetric, and carry out a reflection of the entire system. On the one hand α and η_{t} cannot change because the system is unchanged (given that it is mirrorsymmetric), on the other hand however α must change because it is a pseudo-scalar. Therefore, for homogeneous, isotropic and mirror-symmetric turbulence, α is zero.

If we substitute equation (2.29) into equation (2.25) and use equation (2.3) we obtain:

$$\overline{\mathbf{J}} = \sigma_{\mathrm{t}} (\overline{\mathbf{E}} + \overline{\mathbf{v}} \times \overline{\mathbf{B}} + \alpha \overline{\mathbf{B}}) \tag{2.33}$$

where $\sigma_{\mathrm{t}} = \sigma / (1 + \eta_{\mathrm{t}} / \eta)$. Therefore in the non-mirrorsymmetric case an electromotive force $\alpha \overline{\mathbf{B}}$ appears in Ohm's law for the mean fields, which is parallel or antiparallel to the mean magnetic field, according to the sign of α. This new effect, called α-effect, is due to the turbulent motion and is of great importance in dynamo theory.

2.4 The full set of MHD equations

In the previous Sections we have considered the equations for the electromagnetic field, and have derived the induction equation. This is all that we are going to need in our calculations, since we are working in the kinematic approximation, where the velocity field is taken as fixed. However for the sake of completeness we here report all of the remaining equations from the full set of MHD equations, i.e. the equation of motion, the continuity equation, the energy equation and the equation of state.

- Equation of motion:

$$\rho \, D_t \mathbf{v} = -\rho \, \nabla \psi - \nabla \left(p + \frac{B^2}{2\mu} \right) + \frac{1}{\mu} (\mathbf{B} \cdot \nabla) \mathbf{B} + \nabla \cdot \tau \tag{2.34}$$

  where $\mathrm{D}_t \equiv \partial_t + \mathbf{v} \cdot \nabla$ is the Lagrangian, or convective, derivative and ∂_t is the Eulerian derivative; ψ is the gravitational potential; ρ is the mass density; p is the pressure of the fluid; and τ is the viscous stress tensor.

  Note that in comparison with the standard Navier-Stokes equation, equation (2.34) contains an additional term: the Lorentz force $\mathbf{J} \times \mathbf{B}$, which has been decomposed into the magnetic pressure and tension: $\frac{B^2}{2\mu}$ and $\frac{1}{\mu}(\mathbf{B} \cdot \nabla)\mathbf{B}$ respectively.

- mass conservation equation or continuity equation:

$$\mathrm{D}_t\rho + \rho\nabla\cdot\mathbf{v} = 0 \tag{2.35}$$

- energy equation:

$$\rho T\mathrm{D}_t s = \rho\mathrm{D}_t u + p\nabla\cdot\mathbf{v}\ (=-L) \tag{2.36}$$

  where u is the specific internal energy; s is the specific entropy; and L is the rate of energy loss per unit volume

- equation of state:

$$p = p(\rho, T, \dots) \tag{2.37}$$

  the precise expression for this depends on the nature of the matter in the system under consideration. The equation of state gives the pressure in terms of other quantities characterizing the fluid, which could include density, entropy, chemical composition, ...

Finally an equation for the viscous force ($\nabla\cdot\tau$) is needed in order to close the system, which in total is composed of 18 equations – the induction equation, two Maxwell equations, the equation for the viscous force, the equation of motion, the continuity equation, the energy equation and the equation of state – for 18 unknowns – velocity, electromagnetic field, viscous force, pressure, mass density, temperature, specific internal energy, specific entropy and charge density.

Bibliography

[1] Brandenburg A. & Subramanian K., 2005, Phys. Rep., 417, 1

[2] Krause F. & Raedler K.-H. 1980, Mean-field magnetohydrodynamics and dynamo theory (Pergamon Press, Oxford)

[3] Mestel L. 1999, Stellar Magnetism (Oxford Univ. Press, Oxford)

[4] Magnetohydrodynamics. In Wikipedia, the free encyclopedia. Retrieved August 5, 2009, from http://www.scholarpedia.org/article/Magnetohydrodynamics

Chapter 3

Dynamos in proto-neutron stars

In this Chapter we begin our journey through the magnetic field–plasma interaction. The stage here is the inside of a proto-neutron star (PNS), where we think that, because of the neutron finger instability, a large scale dynamo is active. We explore this dynamo within the mean field theory and the kinematic approximation, including quenching functions for both the mean electromotive force and the turbulent magnetic diffusivity.

We begin with a general introduction, afterwards we formulate the simplified model that we adopt to describe the PNS and derive the system of partial differential equations (PDEs) which apply to our specific case. Subsequently the numerical code used to solve these equations is briefly described. At this point we can delineate in detail the methodology used in our analysis and present the results. We use six different PNS configurations in order to grasp the effect of the parameters on the magnetic field evolution and final intensity. At the end we summarize our results.

3.1 Introduction

The present understanding of the processes that produce the large magnetic field strengths observed in neutron stars (NSs) is still far from being complete. Most of the information about their magnetic fields is in fact derived either from their X-ray spectra, or from their spin-down when these NSs are seen as pulsars. While the former reflects a measure of the local surface field $B_{\rm surf}$, the latter provides information on the global dipolar magnetic field $B_{\rm d}$, if the spin-down is assumed to be solely due to dipolar electromagnetic emission. These two measures are not always in agreement, showing that the measured magnetic fields may have very different length-scales and intensities. In particular, they seem to suggest the presence of more intense and small-scale surface magnetic fields, together with less strong globally dipolar ones. For the pulsar 1E 1207.4-5209, for instance, the dipolar magnetic field estimated from the spin-down rate is $B_{\rm d} \sim 2 - 4 \times 10^{12}\,{\rm G}$ (Pavlov et al. [20]), while the surface field estimated from the absorption features in its spectrum is $B_{\rm surf} \sim 1.5 \times 10^{14}\,{\rm G}$ (Sanwal et al. [26]). Similarly, observations of the pulsar

RBS B1821-24 (Becker et al. [1]) indicate that $B_{\rm d} \sim 10^9$ G, while $B_{\rm surf} \sim 10^{11}$ G.

The existence of magnetic fields with different strengths and distributed on different length-scales can be explained in terms of a dynamo mechanism driven by the simultaneous presence of rotation and turbulent motions. During the first ~ 40 s after their birth, PNSs are expected to develop hydrodynamical instabilities (Epstein [13]; Livio et al. [15]; Burrows & Lattimer [10]), which can excite a turbulent dynamo. Such instabilities could be essentially of two types. The first one, driven by the entropy gradient, is a Rayleigh-type convective instability (CI) that operates in the inner regions of the star. The second one is a double diffusive instability, driven by both the entropy and leptonic gradients. This is usually referred to as the neutron-finger instability (NFI); it operates in the outer regions of the PNS (Miralles et al. [17], [18]) and is expected to evolve by creating finger-like downflows when the neutrinos are still confined (Mezzacappa et al. [16]).

The principle that generates the NFI is of the same sort as that causing salt fingers in the ocean, and is related to having two physical quantities diffusing with different time scales. In the case of the salt fingers, the two quantities are temperature and salinity. Ocean water is stratified in such a way that deep water is colder and purer than surface water. If one perturbs downwards a surface fluid element, with temperature $T_{\rm s}$ and salinity $Y_{\rm s}$, this will be immersed in an anvironment characterized by a temperature $T < T_{\rm s}$ and a salinity $Y < Y_{\rm s}$. Given that heat diffuses faster than salt (the difference being about two orders of magnitude), the perturbed fluid element will adjust its temperature to the ambient one without changing its salinity, and consequently it will be heavier than the environment and will continue to go downwards (see figure 3.1). This is a typical example of double diffusive instability. Similarly in PNSs when the energy diffusion time is shorter than the lepton one, the NFI can be generated. In order to study the inside of a PNS and to understand whether a region can be neutron-finger unstable, convectively unstable or stable Miralles et al. [17] included within the standard Ledoux criterion[1] dissipative processes such as neutrino transport and viscosity. Doing this they shown that initially only a small region below the crust is unstable, but after about 10 s more than 90 per cent of the star is unstable, with the CI involving mainly the central part of the star and the NFI all the rest. The unstable regions then begin to shrink again and after about 40 s the star is completely stable (see figure 1 in [17]). Therefore if any dynamo action is activated by this kind of instability it can operate only for a maximum of 40 s. After that the star is stable, therefore in this picture the magnetic field that a neutron star has at birth is the one that a PNS has when the instabilities disappear.

Although some authors have recently raised doubts about the existence of the NFI (Buras et al. [9], Dessart et al. [12], Bruenn et al. [8]), no firm conclusion has yet been

[1] According to this criterion the unstable regions are those for which:

$$\left(\frac{\Delta(\nabla T)}{T}\right)_z - \frac{\delta}{\beta}\frac{dY}{dz} > 0\,,$$

where Y is the lepton to baryon ratio and δ and β are the coefficients of the chemical and thermal expansion.

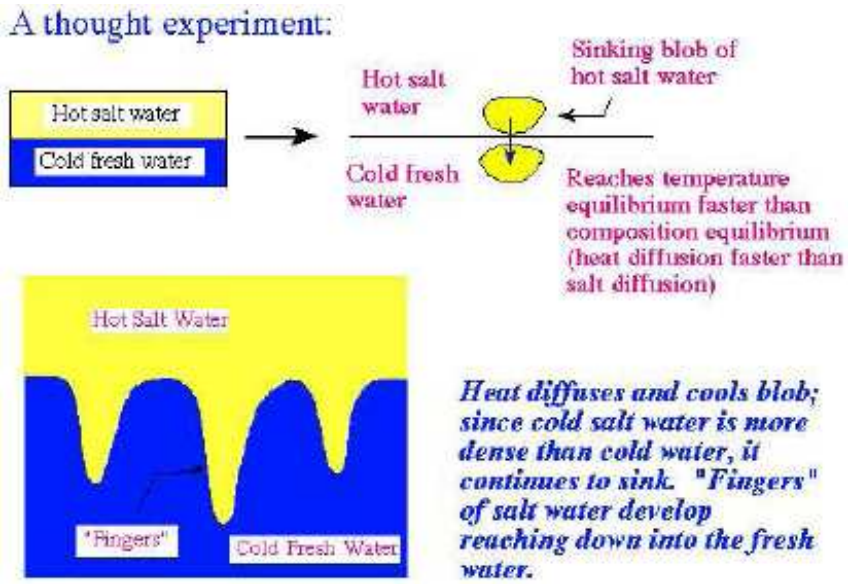

Figure 3.1: Schematic diagram for salt finger formation in the ocean.

reached, leaving the debate open. Here, we do not attempt to enter this debate but rather, because of the interesting astrophysical implications that it may have, we will consider the NFI as taking place and having the dynamical properties as described by Miralles et al. [17], [18].

We note that the co-existence of the two instability mechanisms produces both a local dynamo process (Thompson & Duncan [27]; Xu & Busse [29]) and a mean-field one (Bonanno et al. [4]). As shown in Miralles et al. [17], [18], the growth-times of the instabilities in the two regions differ by 2 or 3 orders of magnitude, being $\tau_{\rm CI} \sim 0.1\,{\rm ms}$ in the zone of the CI and $\tau_{\rm NFI} \sim 30 - 100\,{\rm ms}$ in the zone of the NFI. Since the typical spin period of a PNS is $P \sim 100\,{\rm ms}$, the turbulent eddies created by the CI are not influenced by the rotation and therefore they can only excite a local dynamo. On the other hand, the Rossby number in the zone of the NFI, defined as $R_{\rm o} \simeq P/\tau_{\rm NFI}$, is about unity and the turbulent motions can therefore be influenced significantly by the rotation, favouring the excitation of a global mean-field dynamo. Because of the large difference in the growth-rates of the two instabilities, the two processes, i.e. the local dynamo and the global mean-field one, are essentially decoupled.

Here, we focus our attention on the turbulent mean-field dynamo action that may be excited by the NFI. More specifically, we exploit a simple one-dimensional toy model that aims at capturing, at least qualitatively, the features of the dynamo action. The model, which includes the nonlinearities introduced by the feedback processes, which in turn tend to saturate the growth of the magnetic field, i.e. α-quenching (Bonanno et al. [5], [6]; Rüdiger & Arlt [23]), and suppress its turbulent diffusion, i.e. η-quenching (Rüdiger

& Arlt [23]), is evolved numerically with a very large variety of initial conditions. These include varying the spin period of the PNS, the strength of the differential rotation between the core and the surface, the intensity of the primordial (seed) magnetic field, and the extent of the zone of the NFI.

Overall, we find that increasing the extent of zone of the neutron-finger instability favours the dynamo excitation, and that the combined action of differential rotation and diffusion can produce an increase in the strength of the generated toroidal field by several orders of magnitude. We also confirm the existence of a critical spin-period below which the dynamo is always excited independently of the differential rotation strength, and whose value is related only to the size of the neutron-finger instability zone.

3.2 The model

In Chapter 2, Section 2.3, we have derived the induction equation for mean fields (see equation (2.32)), which we report here again:

$$\partial_t \mathbf{B} = \nabla \times (\mathbf{v} \times \mathbf{B} + \alpha \mathbf{B}) - \nabla \times (\eta \nabla \times \mathbf{B}) \tag{3.1}$$

where $\mathbf{B}$ is the mean magnetic field, $\mathbf{v}$ the mean velocity field, η the turbulent magnetic diffusivity, and α a pseudo-scalar measuring the efficiency of the dynamo α-effect (this is usually referred to as the α-parameter), which is responsible for regenerating a poloidal field from the toroidal field (see figure 3.2).

Our simplified model is inspired to Brandenburg et al. [7], Rüdiger et al. [25], and Rüdiger & Arlt [23]. It uses orthogonal Cartesian coordinates and the PNS is modeled as a cylinder with the z-axis being the axis of rotation. The cylinder has an infinite radial extension and is restricted by boundaries in the z direction, the semi-height H being the radius of the PNS. We assume that the magnetic field components depend on z only.

Clearly, this simplified model has the advantage of leading to a very simple expression for the induction equation (3.1) which, after making a suitable choice for the velocity and magnetic fields, can be recast into a system of two coupled PDEs that are of first order in time. This reduces the computational costs enormously and allows a parametric investigation to be performed, which would be impossible if it involved fully 3D simulations. Yet, despite the considerable simplifications, this simple geometry has been shown to yield instructive results that have opened the way for modern, realistic 3D models (Weiss et al. [28]). Our simplified model of the PNS is shown in figure 3.2, where we highlight the CI and NFI zones that are separated by a thin interface of thickness d, which is not shown in the figure. Note that despite the cylindrical appearance of the star, the system does not have a cylindrical symmetry but rather a planar one across the (x, y) plane.

As we have already mentioned we are under the kinematic dynamo approximation, in which the solution of the induction equation (3.1) is assumed to be decoupled from the Euler equations (i.e. the PNS is assumed to be in hydrostatic equilibrium at all times), and no feedback from the magnetic field is taken into account in the conservation of momentum and energy. As a result, the velocity field is taken as pre-assigned and time-

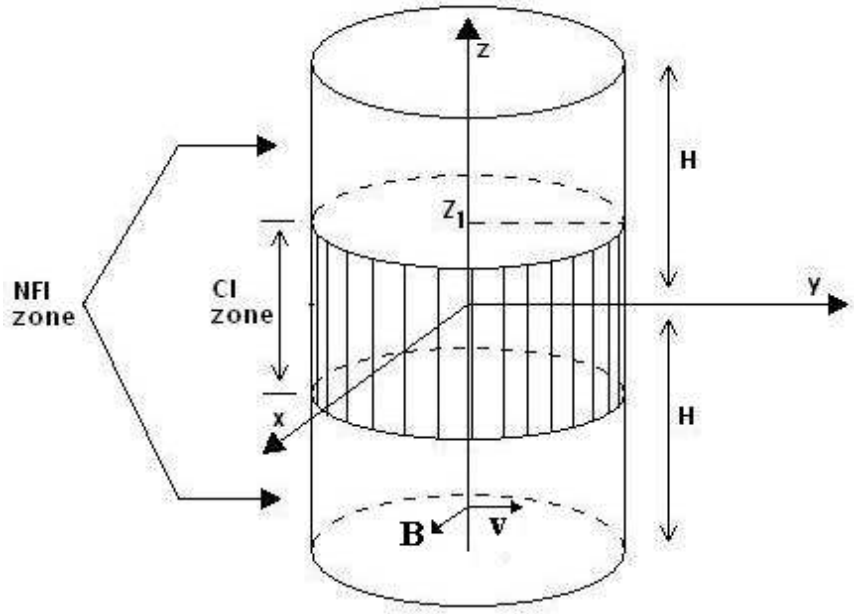

Figure 3.2: Schematic diagram of our model of the PNS.

independent. This approximation works quite well as long as the magnetic field strength is small (i.e. as long as the magnetic pressure and tension are negligible in the Euler equations), but has the drawback that nothing prevents the indefinite growth of the magnetic field once a dynamo action is present. In real systems, the velocity profile will adjust itself in such a way as to reduce the efficiency of the dynamo and here, as a way of mimicking this feedback, we introduce two quenching functions (described later in more detail) that suppress the amplification as the total field increases above a certain threshold, thus leading the system towards saturation even in the absence of a consistent feedback.

Our model for the kinematic dynamo follows the one proposed by Rüdiger et al. [25] and Blackman & Brandenburg [3] in that we use a linear shear for the velocity field:

$$\mathbf{v} = (0, kx, 0) \tag{3.2}$$

and consequently the mean field, which we take to be co-planar with the velocity, is one dimensional:

$$\mathbf{B} = (B_x(z), B_y(z), 0) \tag{3.3}$$

The α-parameter and the magnetic diffusivity η are both expressed as the product of

three terms

$$\alpha = \alpha_0\, \alpha'(z,t)\psi_\alpha(\mathbf{B}) \tag{3.4}$$
$$\eta = \eta_0\, \eta'(z,t)\, \psi_\eta(\mathbf{B}) \tag{3.5}$$

where α_0 and η_0 measure the strength of the α-effect and turbulent diffusion respectively, while $\alpha'(z,t)$ and $\eta'(z,t)$ represent the profiles of α and η in the two instability regions. More specifically, α' is chosen to be antisymmetric across the equatorial plane and different from zero only in the zone of the NFI , where the mean-field dynamo is at work. The turbulent diffusivity η', on the other hand, is set to be of the order of unity in the zone of the NFI and about an order of magnitude larger in the turbulent zone of the CI. We implement these prescriptions by making use of the error function as

$$\alpha'(z,t) \equiv \begin{cases} \frac{1}{2}\left[1+\mathrm{erf}\left(-(z+\lambda)/d\right)\right] & z \in [-H,0] \\ \\ -\frac{1}{2}\left[1+\mathrm{erf}\left((z-\lambda)/d\right)\right] & z \in [0,H] \end{cases} \tag{3.6}$$

$$\eta'(z,t) \equiv \frac{1}{10}\left\{10-\frac{9}{2}\Big[1+\mathrm{erf}\left[(z-\lambda)/d\right]\Big]\right\} \times \left\{10-\frac{9}{2}\Big[1+\mathrm{erf}\left[-(z+\lambda)/d\right]\Big]\right\} \tag{3.7}$$

where $\lambda \equiv z_1 + Vt$, with z_1 being the coordinate of the boundary between the CI and NFI zones and V the expansion velocity of the boundary layer. The quantity d represents the thickness of the interface between the two zones and is used to obtain a smooth change of the error function, with smaller values leading to sharper changes; for the results reported here we have chosen $d/H = 0.04$. The profiles of α' and η', as given by equations (3.6) and (3.7), are shown in figure 3.3, with the solid and dashed lines indicating the initial conditions and the final conditions after $40\,\mathrm{s}$, respectively. Finally, $\psi_\alpha(\mathbf{B})$ and $\psi_\eta(\mathbf{B})$ appearing in equations (3.4) and (3.5) represent the quenching functions for the α-effect and turbulent diffusion η, respectively. These terms are used to limit the otherwise unlimited growth of the magnetic field (α-quenching) and suppress its turbulent diffusion (η-quenching). In general they are expected to have a different dependence on the magnetic field strength, but we here consider a single expression for the two functions in terms of the equipartition magnetic field $B_{\mathrm{eq}} = \langle \mathrm{u} \rangle \sqrt{4\pi\rho}$, where $\langle \mathrm{u} \rangle$ is the mean velocity of turbulent eddies and ρ the mass-density (for typical values of PNSs $B_{\mathrm{eq}} \approx 10^{13}$ G, as will be shown at the end of this Section):

$$\psi_{\alpha,\eta}(\mathbf{B}) \equiv \left[1+\int_{-H}^{H}\left(\frac{B}{B_{\mathrm{eq}}}\right)^2 dz\right]^{-1} \tag{3.8}$$

Making use of these definitions, equation (3.1) can be split into the following two coupled

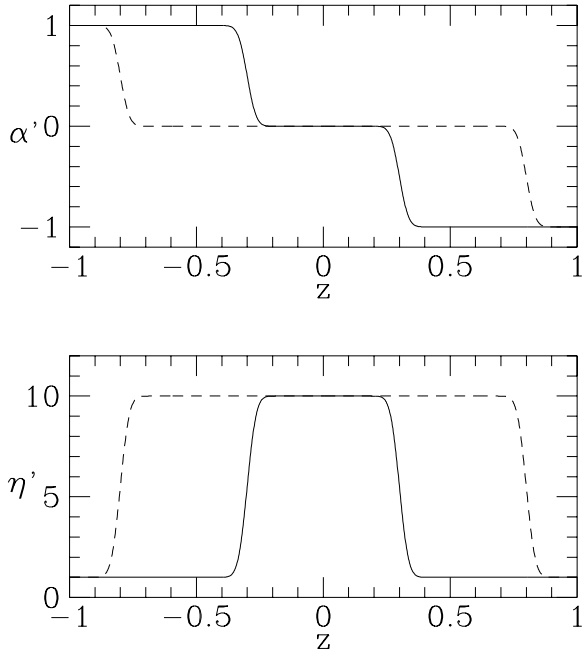

Figure 3.3: Top panel: profiles of the normalized function α' at the beginning of the numerical simulation for $t = 0$ (solid line) and at the end of the numerical simulation for $t = 40\,\tau_{\rm D}$ (dashed line); bottom panel: the same as in the top panel but for η'.

scalar PDEs:

$$\partial_t B_x = -\partial_z(\alpha B_y) + \partial_z\left(\eta \partial_z B_x\right) \tag{3.9}$$

$$\partial_t B_y = \partial_z(\alpha B_x) + B_x \partial_x v_y + \partial_z\left(\eta \partial_z B_y\right) \tag{3.10}$$

which can also be written in a dimensionless form by scaling lengths in units of the semi-height of the cylinder H, times in units of the diffusion time $\tau_{\rm D} = H^2/\eta_0$, and magnetic fields in units of $B_{\rm eq}$. We also find it useful to introduce the dimensionless parameters

$$C_\alpha \equiv \alpha_0 \frac{H}{\eta_0}\,, \qquad \text{and} \qquad C_\Omega \equiv \partial_x v_y \left(\frac{H^2}{\eta_0}\right) = k \left(\frac{H^2}{\eta_0}\right) \tag{3.11}$$

which represent the Reynolds numbers for the α-effect and the differential rotation, respectively. Furthermore, by introducing the standard vector potential $\mathbf{A} = [A_x(z), A_y(z), 0]$,

so that the poloidal component of the magnetic field is $\mathcal{B}_p \equiv B_x = -\partial_z A_y$, we obtain the following dimensionless equations for the vector potential $\mathcal{A} = A_y$ and the toroidal component of the magnetic field $\mathcal{B}_t \equiv B_y$:

$$\partial_t \mathcal{A} = C_\alpha \alpha(z,t)\psi_\alpha(B_{tot})\mathcal{B}_t + \eta(z,t)\psi_\eta(B_{tot})\partial_z^2 \mathcal{A} \tag{3.12}$$

$$\partial_t \mathcal{B}_t = -C_\alpha \partial_z \left[\alpha(z,t)\psi_\alpha(B_{tot})\partial_z \mathcal{A}\right] - C_\Omega \partial_z \mathcal{A} + \\ + \partial_z \left[\eta(z,t)\psi_\eta(B_{tot})\partial_z \mathcal{B}_t\right] \tag{3.13}$$

where $B_{tot} \equiv [\mathcal{B}_t^2 + (\partial_z \mathcal{A})^2]^{1/2}$. Once the initial conditions $\mathcal{B}_t(z,0)$ and $\mathcal{A}(z,0)$ are given, together with the parameters, C_α, C_Ω, α, η, ψ_α, ψ_η, and suitable boundary conditions at the stellar edges, it is possible to solve equations (3.12) and (3.13) to describe the time evolution of the magnetic field. Our choice for the boundary conditions reflects the fact that we are interested in an adiabatic evolution of the magnetic field in the stellar interior, thus neglecting the energy losses related to a Poynting flux. Because of this, we simply set the magnetic fields at these locations to zero.

A dynamo described by equations (3.12)–(3.13) is said to be an $\alpha^2\Omega$ dynamo, because in the governing equations there two terms representing the α-effect (the terms in C_α) and one term for the Ω-effect (the one in C_Ω). When in equation (3.13) the α term is negligible with the Ω term (i.e. the differential rotation is very large), then the dynamo is said $\alpha\Omega$. Finally when there is no differential rotation, one has the α^2 dynamo. The consequences of the α-effect are made clear by these two equations, in fact when $\alpha = 0$ from equation (3.12) one obtains that the poloidal component of the magnetic field is ruled by a diffusion equation (when η is constant in space) and is therefore doomed to decay to zero. Consequently, with α and the poloidal component being both zero, equation (3.13) also reduces to a diffusion equation and the toroidal component of the magnetic field decays as well. Similarly, the role of the Ω-effect can be grasped be looking at equation (3.13). In fact, should the α-term be negligible in this equation, it is the presence of the C_Ω term to ensure that a toroidal magnetic field is generated by the poloidal component. Therefore we can conclude that with a succession of α-effects only, or of α-effects and Ω-effects, one could be able to maintain a magnetic field via a dynamo action:

$$\cdots\ B_p \xrightarrow{\Omega\,\alpha} B_t \xrightarrow{\alpha} B_p\ \cdots \tag{3.14}$$

It is important to note that the parameters C_α and C_Ω are not linearly independent but can be related in terms of the strength of the differential rotation, the pressure scale-height and the radius of the PNS. To deduce this relation we recall that the $\alpha\Omega$-dynamo assumes that $\alpha_0 \sim \Omega L_p$, where Ω is the angular velocity and L_p the pressure scale-height, so that

$$P \sim \frac{\xi}{C_\alpha} = \frac{2\pi L_\mathrm{p} H}{C_\alpha \eta_0} \tag{3.15}$$

where $\xi \equiv 2\pi L_\mathrm{p} H/\eta_0$. For a typical PNS with mass $\sim 1 M_\odot$, $H \sim 15\,\mathrm{km}$ and $L_\mathrm{p} \sim 3\,\mathrm{km}$ (Bonanno et al. [4]), $\eta_0 \sim L_\mathrm{p}^2/\tau_{\mathrm{NFI}}$ ranges from $9 \times 10^{11}\,\mathrm{cm^2 s^{-1}}$ for NFI eddy turnover times of $100\,\mathrm{ms}$, up to $3 \times 10^{12}\,\mathrm{cm^2 s^{-1}}$ for NFI eddy turnover times of $30\,\mathrm{ms}$. Such values

of η_0 yield typical diffusion timescales $\tau_{\rm D}$ ranging from $0.75\,{\rm s}$ to $2.5\,{\rm s}$, respectively. As a result, the parameter ξ is expected to be roughly in the range $1\,{\rm s} \leq \xi \leq 3\,{\rm s}$ for all of the relevant parameter space considered here.

In a similar way, since $\partial_x v_y = k = v/x \sim \Delta\Omega$, and defining the relative differential rotation strength as $q \equiv \Delta\Omega/\Omega \simeq (\Omega_{\rm s} - \Omega_{\rm c})/\Omega_{\rm s}$, where $\Omega_{\rm s}$ and $\Omega_{\rm c}$ are the angular velocities of the surface and the core respectively, it is possible to conclude that

$$q \sim \zeta \frac{C_\Omega}{C_\alpha} \tag{3.16}$$

where $\zeta \equiv L_{\rm p}/H \simeq 1/5$. Here we use $\Delta\Omega$ as a global measure of the rotational stress instead of using a necessarily arbitrary function that describes the behaviour of $\Omega(z)$ in the region between $\Omega_{\rm c}$ and $\Omega_{\rm s}$. On the other hand we are severely limited by our ignorance of the detailed processes leading to the appearance of differential rotation in the zone of the NFI of PNSs.

For all of the calculations reported here we assume that the angular velocity of the core is larger than that of the surface, so that $q < 0$ and, conservatively, we limit our analysis to values of $|q|$ not exceeding 10^2, i.e. a core rotating 10^2 times faster than surface. Finally, by assuming a mass-density in the zone of the NFI of $\rho \sim 10^{13}\,{\rm g\,cm^{-3}}$ and eddy convective velocities $\langle {\rm u} \rangle \simeq L_{\rm p}/\tau_{\rm NFI} \sim 3 \times 10^6\,{\rm cm\,s^{-1}}$, it follows that $B_{\rm eq}$ is of the order of $10^{13}\,{\rm G}$. The parameters defined in equations (3.15) and (3.16) essentially determine the parameter space for the solutions of equations (3.12) and (3.13).

3.3 Numerical method and tests

In order to solve the mixed parabolic-hyperbolic system of PDEs (3.12) and (3.13), we discretize the continuum space-time by replacing it with a two dimensional grid, where the two dimensions represent the space and the time variables, z and t, respectively. We use constant spacing in both directions, with a typical grid of 50 zones. Tests were performed with a larger number of gridpoints (100, 200 and 400) and have revealed that a minimum of 50 gridpoints was sufficient to give convergence with errors of no more than a few percent.

The evolution algorithm chosen is the FTCS scheme (Forward-in-Time, Centered-in-Space), which gives a first-order approximation for the time derivatives and a second-order approximation for the space derivatives. Furthermore, stability requires the time-step to be $\Delta t = \mathcal{O}(\Delta z^2)$ (we typically use $\Delta t = 10^{-2}\Delta z^2$), thus making the whole algorithm second-order both in space and in time. According to this scheme the derivatives

are discretized in the following way:

$$\partial_t F^n = \frac{F^{n+1} - F^n}{\Delta t} \tag{3.17}$$

$$\partial_z F_i = \frac{F_{i+1} - F_{i-1}}{2\Delta i} \tag{3.18}$$

$$\partial_z^2 F_i = \frac{F_{i+1} - 2\,F_i + F_{i-1}}{\Delta i^2} \tag{3.19}$$

The discretized version of equations (3.12)–(3.13) is then:

$$\begin{aligned} \mathcal{A}_i^{n+1} &= \mathcal{A}_i^n + \Delta t\, d_i^n\, \mathcal{B}_i^n + \\ &\quad + k_1\, a_i^n\, \left(\mathcal{A}_{i+1}^n - 2\,\mathcal{A}_i^n + \mathcal{A}_{i-1}^n\right) \end{aligned} \tag{3.20}$$

$$\begin{aligned} \mathcal{B}_i^{n+1} &= \mathcal{B}_i^n + k_2\, c\, \left(\chi_{i+1}^n - \chi_{i-1}^n\right) + \\ &\quad + k_2\, b\, \left(\mathcal{A}_{i+1}^n - \mathcal{A}_{i-1}^n\right) + \\ &\quad + k_1\, a_i^n\, \left(\mathcal{B}_{i+1}^n - 2\,\mathcal{B}_i^n + \mathcal{B}_{i-1}^n\right) + \\ &\quad + k_2\, f_i^n\, \left(\mathcal{B}_{i+1}^n - \mathcal{B}_{i-1}^n\right) \end{aligned} \tag{3.21}$$

where

$$\chi_i^n = e_i^n\, \frac{\mathcal{A}_{i+1}^n - \mathcal{A}_{i-1}^n}{2\Delta z} \tag{3.22}$$

and

$$k_1 = \frac{\Delta t}{\Delta z^2}, \quad k_2 = \frac{\Delta t}{2\,\Delta z} \tag{3.23}$$

$$a_i^n = \eta_i^n\, \psi_\eta^n, \quad b = -C_\Omega, \quad c = -C_\alpha \tag{3.24}$$

$$d_i^n = C_\alpha\, \alpha_i^n\, \psi_\alpha^n, \quad e_i^n = \alpha_i^n\, \psi_\alpha^n, \quad f_i^n = \frac{\eta_{i+1}^n - \eta_{i-1}^n}{2\Delta z} \tag{3.25}$$

For the implementation of the boundary conditions we use the system of having ghost zones at the edges of the domain.

As a test of the code we have considered the equations when $C_\alpha = C_\Omega = 0$, $\psi_\eta = 1$ and $\eta(z,t) = 5 \cdot 10^{-2}$ so as to have two decoupled purely parabolic equations, for which an analytic solution can be calculated, and compared the numerical solution with the analytic one. The result of the comparison is that the maximum error is of the order of 2 per cent.

We have also checked the convergence of the method by comparing the numerical solutions obtained with different spatial grids at a given time. The same continuum function $u(z,t)$ is approximated in a different way according to the space-time discretization: $u(z,t) = u_i^n(h) + \epsilon_h$, where h is the chosen space-interval and ϵ_h is the truncation error. If we suppose that this error depends on h only, we can write: $\epsilon_h = k\, h^p$, with p being the order of convergence. It is then possible to deduce the following relation among the

values of different discretized functions calculated at the same grid location i:

$$\frac{u_i^n(h) - u_i^n(h/2)}{u_i^n(h/2) - u_i^n(h/4)} = 2^p \tag{3.26}$$

The value of p obtained as averaged over the spatial domain is 2.00 ± 0.01, thus demonstrating a second-order convergence.

3.4 Analysis and results

While this analysis aims at a better understanding of the behaviour of the dynamos operating in the first stages of the life of a PNS, it is a long way from reproducing realistic conditions. This is partly due to the simplicity of the model employed, and partly to the still poorly constrained physical conditions of a newly born PNS. We recall that, according to Miralles et al. [17], [18], the NFI is expected to last only about $40\,\mathrm{s}$, during which the zone of the NFI goes from occupying a large fraction of the envelope, to being confined to a small layer and then disappearing completely. We model this by assuming that the initial position of the NFI-CI boundary layer is at $z_1^i = 0.3H$ and the final one, after $40\,\mathrm{s}$, is at $z_1^f = 0.8H$ (cf. figure 3.2), with an average expansion velocity of the layer that is $V = (z_1^f - z_1^i)/t = 188\,\mathrm{m\,s^{-1}}$ for $H = 15\,\mathrm{km}$. In this case we also find it convenient to express all variables in terms of dimenionsless quantities after introducing $z' \equiv z/H$, $t' \equiv t/\tau_\mathrm{D}$, and $V' \equiv V\tau_\mathrm{D}/H$. As a result, the coordinate position of the CI-NFI border appearing in equations (3.6) and (3.7) can be written as $\lambda/H = z_1' + V't' = 0.3 + 0.0125\,(\mathrm{s^{-1}})\,t\,(\mathrm{s})$, where $-1 \leq z' \leq 1$, and $0 \leq t \leq 40\,\mathrm{s}$, corresponding to a number of diffusion times ranging from 16 to 53, depending on the turnover time of the eddies of the NFI.

3.4.1 Initial models

As a representative sample of initial data we have considered six different models, four of which have the size of the zone of the NFI being constant in time, with either $z_1' = 0.3$ (large instability zone) or $z_1' = 0.8$ (small instability zone), and are therefore referred to as static. For each of the two values of z_1' we have examined the behaviour with and without η-quenching. Besides the static configurations, which are useful for studying the extreme cases of thick and thin NFI zones respectively, we have also considered two cases, which are referred to as dynamical, in which the NFI zone is allowed to shrink in time from the initial value of $z_1' = 0.3$ to the final one of $z_1' = 0.8$, over the $40\,\mathrm{s}$ during which the instability is expected to be active. For these dynamical models we have also studied the effect of activating or not activating the η-quenching.

The static models are indicated as A, B, Aq and Bq, while the dynamical ones are indicated as AB and ABq; in all cases, the letter "q" is used to indicate whether or not η-quenching is taken into account. For all of these models we have carried out a large number of simulations by varying the seed magnetic field B_s, as well as the spin period

Table 3.1: The parameters z_1' (initial position of the boundary layer), V' (mean velocity of the boundary layer), and η-q (η-quenching activated or not) that define the configurations analyzed, and the ranges of values of $B_{\rm s}$, C_α and $|q|$ used for the simulations. As regards C_α, we mainly used values between 5 and 200, since for smaller values the dynamo is not excited and for larger values the spin period would be too short.

	z_1'	V'	η-q	$B_{\rm s}/B_{\rm eq}$	C_α	$\lvert q\rvert$
A	0.3	0.0	no	$10^{-7}-10^{-1}$	$\leq 10^3$	$10^{-8}-10^2$
B	0.8	0.0	no	$10^{-7}-10^{-1}$	$\leq 10^3$	$10^{-8}-10^2$
Aq	0.3	0.0	yes	$10^{-7}-10^{-1}$	$\leq 10^3$	$10^{-8}-10^2$
Bq	0.8	0.0	yes	$10^{-7}-10^{-1}$	$\leq 10^3$	$10^{-8}-10^2$
AB	0.3	0.0125	no	10^{-7}	$\leq 10^3$	$10^{-8}-10^2$
ABq	0.3	0.0125	yes	10^{-7}	$\leq 10^3$	$10^{-8}-10^2$

P and the strength of the differential rotation $|q|$; all of the models have been evolved for 40 diffusion times (i.e. between $30\,\mathrm{s}$ and $100\,\mathrm{s}$). A summary of the properties of the different initial models and of the parameters used in the simulations is presented in Table 3.1.

3.4.2 Time evolution and critical period

The time evolutions of the average toroidal field $\mathcal{B}_t$ and poloidal field $\mathcal{B}_p$ (calculated in terms of their 2-norms) are shown in figure 3.4 for the configuration Aq, with $|q| = 2$ and $C_\alpha = 4$ ($0.25\,\mathrm{s} \leq \mathrm{P} \leq 0.75\,\mathrm{s}$), and for different values of the seed magnetic field $B_{\rm s}$ in the range $10^{-7}B_{\rm eq} \leq B_{\rm s} \leq 10^{-1}B_{\rm eq}$.

For all of the configurations examined, the evolution of the magnetic field is rather similar and can be separated into two main stages: the first one is a transient phase during which the dynamo action amplifies the seed magnetic field exponentially; in the second phase the magnetic field instead reaches saturation around the equipartition value through the back reaction of the α-quenching. In general, the field reaches saturation within the $40\,\mathrm{s}$ lifetime of the zone of the NFI, except when the seed magnetic field is lower than $10^{-7}B_{\rm eq}$ and $|q| \leq 2$. Nevertheless, in these cases the final magnetic value is of the order of $10^{-2}\,B_{\rm eq}$, thus corresponding to 10^{11} G.

The two stages can easily be distinguished in figure 3.4, which shows the time-evolution of the average of the toroidal and poloidal magnetic fields. The secular slope of the curves in the exponential-amplification phase is clearly independent of $B_{\rm s}$ and constant in time, with $B = B_{\rm s}\ \mathrm{e}^{\,t/\tau_{\rm amp}}$ and $\tau_{\rm amp} \sim 0.6\,\tau_{\rm D}$, where $\tau_{\rm D} \simeq 25\,\tau_{\rm NFI}$ is the diffusion timescale. The growth-time however depends on $|q|$ and C_α, thus suggesting that the seed magnetic field determines only the time interval necessary to achieve the saturation, but not the final strength of the magnetic field. Clearly, if the initial field is too small, the dy-

namo cannot reach the saturation phase within $40\,\mathrm{s}$. Other values of the growth times are $\tau_{\mathrm{amp}} \sim 0.98\,\tau_{\mathrm{D}}$ for configuration ABq (with $C_\alpha = 4$ and $|q| = 3$) and $\tau_{\mathrm{amp}} \sim 2.19\,\tau_{\mathrm{D}}$ for configuration B (with $C_\alpha = 29$ and $|q| = 4$). Therefore the amplification rate ($1/\tau_{\mathrm{D}}$) grows with the size of the zone of the NFI (this is largest in configuration A, smallest in configuration B, and in between in configuration ABq). This aspect is considered in more detail in Section 3.4.3.

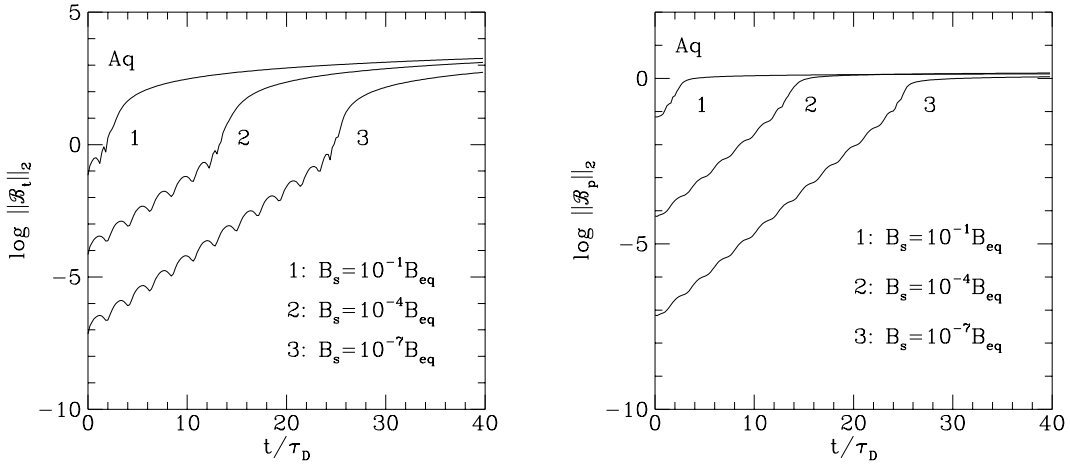

Figure 3.4: Behaviour of the 2-norm of the magnetic field ($\mathcal{B}_t$ left panel, $\mathcal{B}_p$ right panel) as a function of the number of diffusion times (t/τ_{D}) for the Aq configuration, $|q| = 2$, $C_\alpha = 4$ ($250\,\mathrm{ms} \leq P \leq 750\,\mathrm{ms}$), and for different seed magnetic field strengths, B_{s}. The growth-rate of the magnetic field during its amplification phase, before reaching the saturation, is almost independent of the seed magnetic field.

It is possible that the combination of the rotation rate and differential rotation is not adequate to excite the dynamo. In this case the magnetic field is not amplified but rather decays with time. For each value of $|q|$ it is possible to find a threshold value of C_α such that for higher rotation rates (shorter periods) the dynamo is excited, while for lower rotation rates (longer periods) it is not. This value of C_α defines a critical period $\widetilde{P}_c = P_c(|q|)$ through ξ (see equation (3.15)).

The presence of a critical period within the space of parameters is shown in figure 3.5 for the configuration A. The behaviour of the dynamo solutions is plotted as a function of the PNS spin period P and differential rotation strength $|q|$ for three different values of ξ (corresponding to different turnover times of the convective eddies in the zone of the NFI : $\xi = 1$, $\tau_{\mathrm{NFI}} \simeq 30\,\mathrm{ms}$; $\xi = 2$, $\tau_{\mathrm{NFI}} \simeq 65\,\mathrm{ms}$ and $\xi = 3$, $\tau_{\mathrm{NFI}} \simeq 100\,\mathrm{ms}$). The three curves represent the thresholds between the regions in which the solutions of the dynamo

equations grow in time (regions below the curves), thus allowing dynamo excitation, and the regions in which the solutions decay, thus preventing dynamo excitation. The lines in figure 3.5 define therefore the critical dynamo period as a function of $|q|$, and it is evident that the critical spin velocity above which the dynamo operates decreases with increasing differential rotation. The behaviour of these curves suggests that is possible to define a global critical period P_c as the minimum of $\widetilde{P}_c$, so that if a PNS is rotating with a period shorter than P_c then for that PNS the dynamo will be excited independently of the kind of rotation.

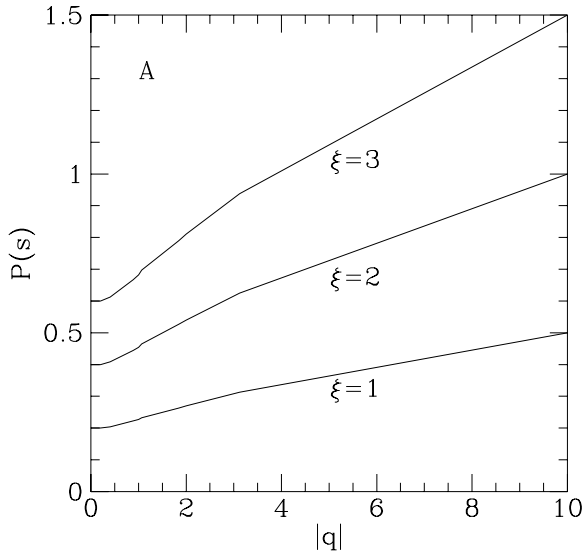

Figure 3.5: Behaviour of the dynamo solutions as a function of the PNS spin period P and of the differential rotation strength $|q|$ for three different values of ξ, related to the turnover time of the convective eddies in the zone of the NFI. The dynamo is activated when the point identified by the values of P and q is below the curve.

The values of the global critical period obtained for the four static configurations are summarized in Table 3.2. Note that for a fixed value of ξ these periods depend only on the thickness of the zone of the NFI and are thus independent of the presence of η-quenching. As a result, in PNSs with larger NFI zones, the dynamo action will be excited more easily, and thus at lower rotation rates, than for PNSs having smaller NFI zones.

Table 3.2: For each static configuration the critical value of C_α (C_α^C) and the corresponding global critical period of the PNS, $P_c = \xi/C_\alpha^C$ ms, for $\xi \in [1,3]$ are reported.

	C_α^C	P_c [ms]
A	5	$200-600$
B	30	$33-99$
Aq	5	$200-600$
Bq	30	$33-99$

3.4.3 The role of thickness of the NFI zone

Since the zone of the NFI is the region where the mean field dynamo is at work, it is natural to expect that by increasing the size of this part of the star the efficiency of the dynamo will also increase. To quantify this improved efficiency we can compare the results obtained for two configurations: one in which the zone of the NFI occupies 70 per cent of the star (configuration A) and another one in which it covers 20 per cent (configuration B). Reducing the extent of the active part of the star has two main effects: reducing the critical period and reducing the intensity of the final magnetic field.

The first of these effects has already been discussed in the previous section, and from Table 3.2 it is possible to note that reducing the size of the zone of the NFI by a factor of 3.5 decreases the critical period by a factor of 6. To quantify the second effect we consider the ratio between the final strength of the magnetic field in configurations A and B, as a function of the differential rotation parameter $|q|$ and of C_α. As expected, the total magnetic field for the configuration A is larger than that for configuration B, regardless of any other parameter. However if one considers the toroidal and the poloidal components separately, one notices that while the former is amplified by a factor $7-13$, the latter is instead reduced, but by a smaller factor ($\lesssim 3$). See Table 3.3.

Table 3.3: Ratio of the final intensity of the magnetic field in configurations A and B. The values in the table are calculated for $|q| > 10$. For $|q| < 10$ we still have $\mathcal{B}_t^{\rm fin}({\rm A})/\mathcal{B}_t^{\rm fin}({\rm B}) > 1$ and $\mathcal{B}_p^{\rm fin}({\rm A})/\mathcal{B}_p^{\rm fin}({\rm B}) < 1$, but the exact value depends on the differential rotation.

	C_α		
	50	100	200
$\mathcal{B}_t^{\rm fin}({\rm A})/\mathcal{B}_t^{\rm fin}({\rm B})$	13.4	6.6	13.0
$\mathcal{B}_p^{\rm fin}({\rm A})/\mathcal{B}_p^{\rm fin}({\rm B})$	0.38	0.37	0.37

3.4.4 Asymptotic states of the static configurations

The values of the magnetic field after $40\,\tau_{\rm D}$ for some representative cases of the static configurations are shown in figure 3.6, which reports the final intensities of the toroidal and poloidal components as functions of $|q|$ and for different values of C_α.

Figure 3.6 refers to configurations without η-quenching and shows that the qualitative evolution of the field is independent of the rotation rate of the star. Furthermore, for small values of the differential rotation, i.e., for $|q| \lesssim |q^*|$ (where $|q^*|$ is a representative threshold value) both the toroidal $\mathcal{B}_t$ and poloidal $\mathcal{B}_p$ components of the magnetic field are constant with $|q|$; while for $|q| \gtrsim |q^*|$, $\mathcal{B}_t$ begins to increase and $\mathcal{B}_p$ to decrease, following power-laws with exponents of the same magnitude but opposite signs (see Table 3.4). Note that the value of $|q^*|$ is smaller for high spin rates since the dynamo is more easily excited when the star is rapidly rotating.

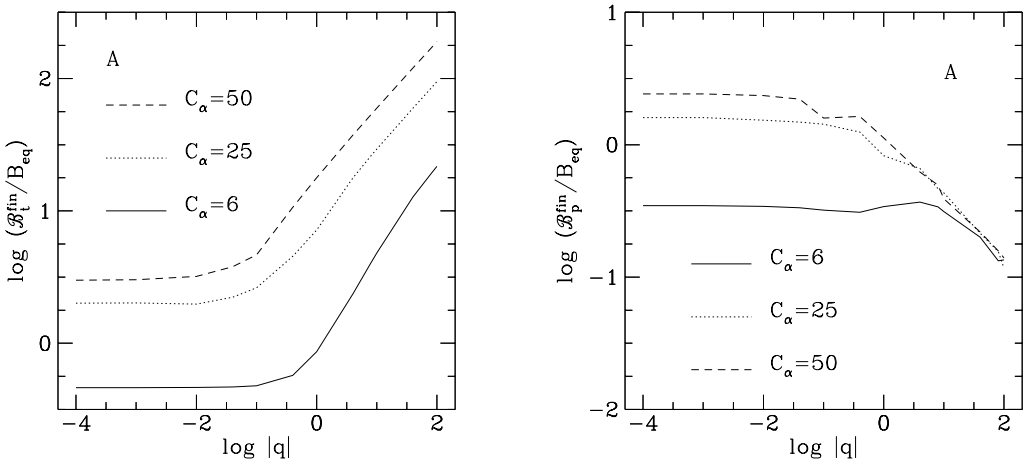

Figure 3.6: Intensity of the magnetic field ($\mathcal{B}_t$ left panel, $\mathcal{B}_p$ right panel) in units of $B_{\rm eq}$, at the end of the evolution, as a function of the differential rotation parameter $|q|$ for different values of C_α. The simulation refers to the configuration A, thus without η-quenching.

Figure 3.7, on the other hand, shows the influence of η-quenching on the mean-field dynamo by comparing the final intensities of the magnetic fields for configurations for which the quenching is either active or not, i.e., configurations Aq and A, respectively. It is quite evident that the main consequence of η-quenching is to increase the amplification factor of the dynamo by several orders of magnitude, leaving the qualitative behaviour of the magnetic field unchanged, but for a significantly smaller value of $|q^*|$.

A way of interpreting these results is to recall that the inclusion of η-quenching en-

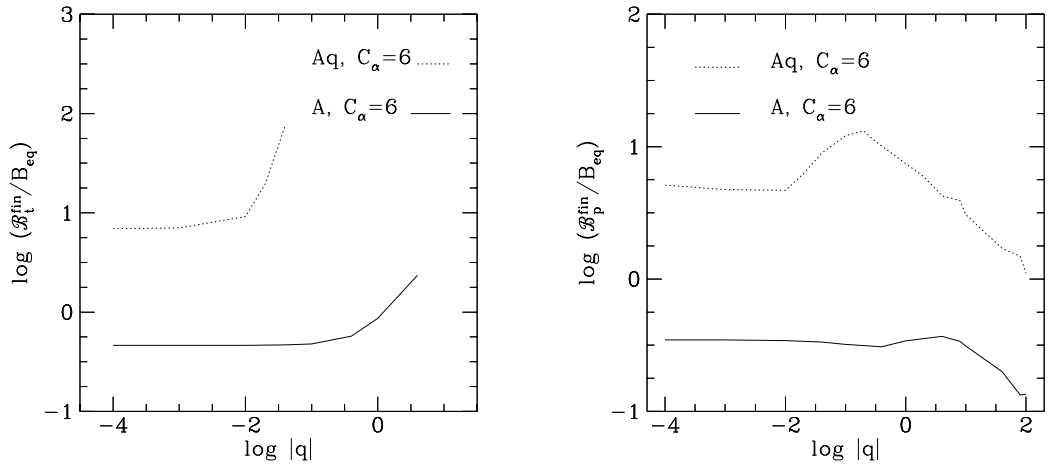

Figure 3.7: Intensity of the magnetic field ($\mathcal{B}_t$ left panel, $\mathcal{B}_p$ right panel) in units of $B_{\rm eq}$, at the end of the evolution, plotted as a function of the differential rotation parameter $|q|$ for $C_\alpha = 6$ ($167\,{\rm ms} < P < 500\,{\rm ms}$), and an initial seed magnetic field of $10^{-7}\,B_{\rm eq}$. The simulation shows the comparison between a configuration with η-quenching (Aq) and without η-quenching (A).

hances the transformation of the poloidal magnetic field into a toroidal one (i.e., Ω-effect) and therefore enhances the importance of differential rotation. In addition, by reducing the magnetic diffusion, η-quenching effectively favours the amplification of the magnetic field (which becomes essentially frozen with the fluid), increasing the duration of the exponential growth phase. In the case shown in figure 3.8 this phase lasts 4 more diffusion times and the growth-rate in this last bit of amplification is even larger than before ($\tau_{\rm amp} \sim 0.8\,\tau_{\rm D}$ vs $\tau_{\rm amp} \sim 0.6\,\tau_{\rm D}$).

A typical example of the spatial distribution of the magnetic field is shown in figure 3.9, where we show the behaviour of the toroidal field as a function of the z coordinate at different time steps for the configuration Aq. As expected, the field is mainly localized in the NFI regions (where $\alpha \neq 0$).

Two remarks are worth making at this point. Firstly, while the figures in this section refer only to the configurations A and Aq, the same behaviour has also been found for the configurations B and Bq, thus indicating that the results presented here are independent of the extent of the zone of the NFI. Secondly, the extreme magnetic-field amplifications obtained are a direct consequence of the idealized setup used in our modeling of the PNS. We expect that a more realistic description of the geometry of the star and a consistent treatment of the feedback of the magnetic field on the dynamics of the plasma will

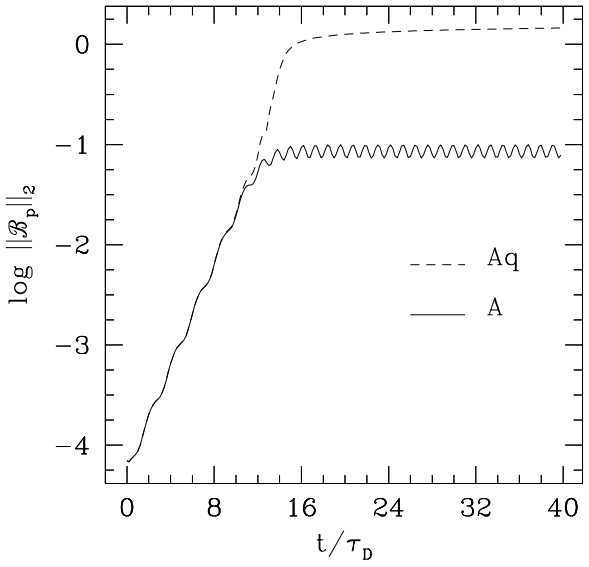

Figure 3.8: Behaviour of the 2-norm of $\mathcal{B}_p$ as a function of the number of diffusion times (t/τ) for the A and Aq configurations, $|q| = 2$, $C_\alpha = 4$ ($250\,\mathrm{ms} \leq \mathrm{P} \leq 750\,\mathrm{ms}$), and for seed magnetic field strengths of $B_\mathrm{s} = 10^{-4} B_\mathrm{eq}$. The growth-rate of the magnetic field during the initial amplification phase is the same for both configurations; at $t \sim 12\tau_\mathrm{D}$ the A configuration saturates, while the Aq one continues to grow until $t \sim 16\tau_\mathrm{D}$, and then is driven to saturation by the α-quenching .

lower these estimates, giving magnetic fields which are less strong but larger than the equipartition value or comparable to it.

3.4.5 Asymptotic states of the dynamical configurations

Although still idealized, the two dynamical configurations AB and ABq are expected to provide a better modeling of the first 40 s of life of the PNS, during which the thickness of the NFI region is assumed to vary from about 70 per cent of the PNS radius, down to about to 20 per cent of it (cf. the profiles of α and η in figure 3.3). However, besides the fact that for these configurations it is not possible to define a unique critical period, since it depends on the thickness of the NFI zone (cf. Sect. 3.4.2), we have found that the qualitative behaviour of the magnetic field for dynamical configurations is very similar to that discussed in the previous section for the static configurations.

More specifically the most salient difference is that, because of the shrinking of the in-

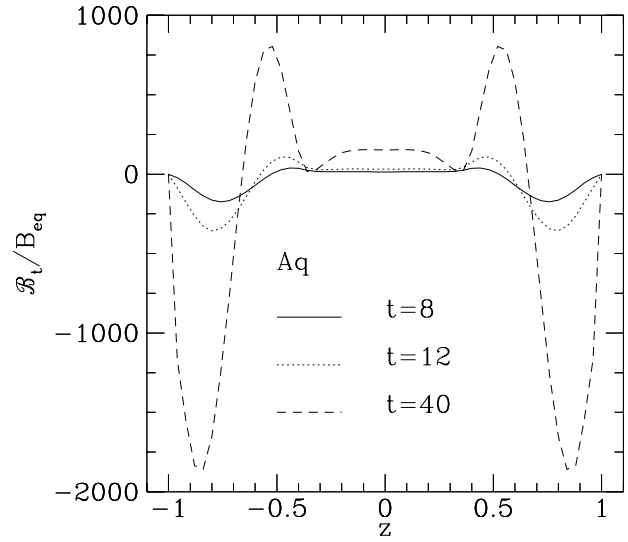

Figure 3.9: Spatial distribution of the toroidal component of the magnetic field at different time steps, for configuration Aq, with $C_\alpha = 10$ and $|q| = 0.1$. For this configuration α is different from zero only in regions with $|z| > 0.3$.

stability zone, the overall amplification is reduced with respect to the A configurations and increased with respect to the B configurations. Indeed, at the beginning of the evolution the zone of the NFI is as large as that of the A configurations, and at the end it is as small as that of the B configurations. Nevertheless, if one considers a spin rate and a differential rotation strength high enough to have the dynamo mechanism active during all of the instability period (i.e. C_α and $|q|$ larger than the critical values of the B configurations), then the final field is comparable to, or even larger than, that in the static A configurations.

3.4.6 The effect of Lorentz force backreaction on differential rotation

Several authors (e.g., Weiss et al. [28]; Belvedere et al. [2]; Roald & Thomas [22]; Moss & Brooke [19]; Gilman & Rempel [14]; Covas et al. [11]; Rempel [21]) investigated the effect of the backreaction generated by the Lorentz-force on the plasma motion; this is sometimes referred to as the Malkus-Proctor effect. These investigations indicate that the dynamo-intensified toroidal field interacts, via the Lorentz force, with the zonal flow (which is predominantly azimuthal), thus limiting the growth of differential rotation and reducing its strength. An obvious consequence of this effect is that the amplification of

the toroidal field itself is also diminished. All of the above mentioned studies, which were mainly devoted to the analysis of the Sun or solar-type stars, made use of an additional term in the Euler equation in order to include the Lorentz force consistently.

This is different from what is done in our simple, idealized model case, where we use the induction equation only, and assume that the rotational stress $\Delta\Omega$ remains constant in time for each configuration. As a result, any phenomenological, parameterized effect of the magnetic field on the already fixed $\Delta\Omega$ would not be consistent with our basic assumptions.

Nevertheless we performed some runs with a phenomenological quenching function applied to C_Ω (Ω-quenching), of the same type as those applied to α and η. The results of these runs show a moderate reduction of the final strength of the toroidal field for all of the examined cases.

A rough estimate of the importance of magnetic field backreaction on differential rotation can be made in terms of the Elsasser number $\Lambda_\mathrm{e} = B^2/8\pi\varrho\Omega\nu$ (Rüdiger & Hollerbach [24]), namely the ratio of magnetic to zonal flow energy. If $\Lambda_\mathrm{e} \ll 1$ the backreaction effect is negligible, while for $\Lambda_\mathrm{e} \gg 1$ it is of overwhelming importance, and should produce a strong reduction of differential rotation. If we define an equipartition $\Lambda_\mathrm{eq} = B_\mathrm{eq}^2/8\pi\varrho\Omega\nu$ and assume that the turbulent viscosity ν is of the same order of turbulent magnetic diffusion η_0 (i.e., both momentum and magnetic field are transported by the same eddies), we have $\Lambda_\mathrm{e} = h^2\Lambda_\mathrm{eq}$, where $h = \mathcal{B}_t/B_\mathrm{eq}$. For the typical values of our PNSs given in Sect. 3.2, $\Lambda_\mathrm{e} \simeq 0.05$ at equipartition, while for magnetic field strengths exceeding the equipartition value by two or three orders of magnitude, the effect of the Lorentz force on differential rotation cannot be neglected.

Our simplified model does not allow us to predict the intensity of this effect, even though we expect that the final magnetic field will be comparable to or slightly larger than the equipartion one. It is also worth pointing out that a reduction or suppression of differential rotation does not necessarily imply a suppression of the dynamo, since the $\alpha^2\Omega$ dynamo can shift to a pure α^2 one. Furthermore we also cannot predict whether the strong toroidal fields generated are stable against the magneto-rotational or Tayler instabilities, which would require an analysis beyond the scope of the present exploratory study.

3.4.7 A general expression for the final magnetic field

From the discussion about the time evolution of the magnetic fields (cf. Sect. 3.4.2) and about their asymptotic states (cf. Sect. 3.4.4 and 3.4.5), it is apparent that the configurations considered in this work have common features that we believe reflect a fundamental behaviour of the mean field dynamo process. Thus we expect these features to be present also when the toy model considered here is replaced by a more realistic one. In what follows we discuss how to summarize these analogies by presenting a general expression for the final magnetic field.

Using figure 3.6 as a guide, it is easy to recognize the existence of a transition value $|q^*|$ such that for $|q| \lesssim |q^*|$ the final magnetic field does not depend on the degree of

differential rotation, while for $|q| \gtrsim |q^*|$ it changes as a power-law. We therefore express this increase with a phenomenological relation of the type

$$\mathcal{B}_t^{\rm fin} = K_t \, (C_\alpha)^{\delta_t} \, |q|^{\gamma_t} \tag{3.27}$$

$$\mathcal{B}_p^{\rm fin} = K_p \, (C_\alpha)^{\delta_p} \, |q|^{\gamma_p} \tag{3.28}$$

where the indices t and p refer to the toroidal and poloidal components, respectively. Note that the threshold value $|q^*|$ may well be different in (3.27) and (3.28), and that the constants $K_{t,p}$ depend on the particular configuration, i.e. on the profile of α and η and on η-quenching.

Table 3.4: Indices of the power-law behaviour found in the dependence of $\mathcal{B}^{\rm fin}$ on the degree of differential rotation $|q|$ and the spin rate C_α. The errors, not reported in the table, are only of a few percent.

	γ_t	γ_p	δ_t	δ_p
A	0.53	−0.48	1.00	0.03
B	0.51	−0.49	1.00	0.00
AB	0.49	−0.48	0.94	0.09
Aq	0.77	−0.37	1.10	0.06
Bq	0.54	−0.48	1.09	0.07
ABq	0.56	−0.46	1.13	0.12

Using a power-law fit, we have calculated the values for the exponents in the phenomenological expressions (3.27) and (3.28) and collected them in Table 3.4 for both the static and the dynamical models, with and without η-quenching. The reported values of $\gamma_{t,p}$ have been computed using several configurations having different C_α (between 6 and 200), while those for $\delta_{t,p}$ have been derived from configurations differing in the amount of differential rotation ($|q|$ in the range $10^{-1} - 10^2$). For all of the configurations considered, the variance around the reported values is very small and of only a few percent.

Overall, the data in Table 3.4 show that $\delta_t \approx 1$, $\delta_p \approx 0$ and that both γ_t and γ_p are usually very close to either $1/2$ or $-1/2$ respectively. We can then rewrite expressions (3.27)–(3.28) simply as

$$\mathcal{B}_t^{\rm fin} \simeq K_t \, C_\alpha |q|^{1/2} \tag{3.29}$$

$$\mathcal{B}_p^{\rm fin} \simeq K_p \, |q|^{-1/2} \tag{3.30}$$

However there is a clear exception to this. For the configuration Aq, the γs are quite far from the common values obtained with all of the other configurations (while for the δs there are no significant differences). In particular we obtain a larger γ_t and a smaller γ_p, meaning that the Ω-effect is somehow more effective than in the other cases in producing toroidal field. This could be due to the η-quenching, in fact in Section 3.4.4 we have

already pointed out how this process has the main consequence of enhancing the Ω-effect, and we think that this effect is the strongest in configuration Aq, because this is the one with the largest NFI zone. Support for this picture is also given by the fact that all of the configurations with η-quenching have a value of γ_t slightly larger than the average.

The behaviour of the final toroidal and poloidal fields in the super-critical dynamo regime, as given by equations (3.29) and (3.30), can be understood in terms of the characteristic dynamo parameters, C_α and C_Ω. The first parameter represents the dynamo's ability to regenerate the poloidal field from the toroidal one (i.e. the α-effect), while the second parameter represents the dynamo's ability to regenerate the toroidal magnetic field from its parent poloidal field, via the action of differential rotation (i.e. the Ω-effect). Both parameters are important as they define the dynamo number, given by $N_{\alpha\Omega} \equiv C_\alpha C_\Omega$ for an $\alpha\Omega$ dynamo, and $N_{\alpha^2\Omega} = C_\alpha^2 C_\Omega$ for an $\alpha^2\Omega$ dynamo. In essence, below a certain critical number $N_{\rm c}$, which depends on the specific model considered, no dynamo action is possible, while the dynamo becomes increasingly efficient as N increases.

The relationships described by equations (3.29) and (3.30) have been derived in the super-critical regime region, where the mean field dynamo behaves as an $\alpha\Omega$ dynamo, and can be rewritten in terms of the dynamo number $N = N_{\alpha\Omega}$ as:

$$\mathcal{B}_t^{\rm fin} \simeq K_t \sqrt{N} \tag{3.31}$$

$$\mathcal{B}_p^{\rm fin} \simeq K_p \frac{C_\alpha}{\sqrt{N}} = K_p \frac{\sqrt{N}}{C_\Omega} \tag{3.32}$$

If one considers both panels of figure 3.6 for $\log|q| > 0$, $\mathcal{B}_t$ substantially increases and $\mathcal{B}_p$ decreases with increasing $|q|$ for each fixed C_α value (i.e. wth increasing C_Ω). Therefore, it is not surprising that $\mathcal{B}_t \propto N^{1/2}$, namely that the toroidal field increases with dynamo efficiency. On the other hand, the poloidal field $\mathcal{B}_p$ will necessarily decrease with increasing dynamo efficiency, since the increase of N is only due to the increase of C_Ω (C_α is kept fixed for each simulation) and the Ω-effect reduces the poloidal component of the field. This is consistent with the fact that, at high differential rotation rates, the zonal flow dominates with respect to the vertical motions (which are predominantly radial) thus reducing the strength of convection and therefore the efficiency of the α-effect, namely the regeneration of the poloidal field.

We expect that more sophisticated calculations will produce changes in the values reported in equations (3.29) and (3.30), especially in the transition between the $\alpha^2\Omega$ and the $\alpha\Omega$ dynamos, when the Lorentz-force feedback is properly taken into account. However, we expect that the overall behaviour of the magnetic field as given by these equations will remain unaltered.

3.5 Conclusions

In this Chapter we have presented a toy model to describe the amplification of the magnetic field inside a proto-neutron star (PNS) via a turbulent dynamo action. The model

assumes that a neutron-finger instability (NFI) develops in the outer regions of a PNS during the early stages of its life as discussed by Miralles et al. [17], [18], and that the conditions for the generation of a mean-field dynamo process are met. Although highly simplified because of being only one-dimensional and because of adopting the kinematic approximation, our model aims to capture the qualitative features of the dynamo action by including a moving boundary of the instability zone and the nonlinearities introduced by the feedback processes, which saturate the growth of the magnetic field (i.e. α-quenching) and suppress its turbulent diffusion (i.e. η-quenching).

In essence, the amplification of the magnetic field is described in terms of a system of coupled partial differential equations of mixed hyperbolic-parabolic type, which have been solved numerically for a very large range of initial conditions. These include varying the spin period of the PNS, the strength of the differential rotation between the core and the surface, the intensity of the primordial (seed) magnetic field, and the extent of the NFI zone.

Overall, we have found that, independently of whether the size of the NFI zone varies in time or not, the magnetic field undergoes a first exponential increase with a growth-time that is the same for both the toroidal and the poloidal components of the magnetic field. The exact value of the growth-time depends on several parameters and is roughly in the range $\tau_{\rm amp} \sim [0.5 - 2.5]\ \tau_{\rm D}$, with $\tau_{\rm D}$ being the diffusion timescale. The exponential growth then stops because of the back reaction given by the α-quenching and the magnetic field reaches saturation. The final magnetic field produced at the end of the evolution does not depend sensitively on the initial magnetic field, but it does depend on whether the η-quenching is active or not, becoming 2-3 orders of magnitude larger if the η-quenching is active.

Despite its simplicity, our model is also able to capture another important feature of the dynamo mechanism, namely the existence of a critical rotation period P_c, above which no dynamo action is possible and the magnetic field simply decays (Bonanno et al. [4]). For periods near to the critical one, on the other hand, the dynamo is just able to sustain the magnetic field close to its initial value, thus avoiding its decay. However, as the spin rate (or the degree of differential rotation) is increased, the dynamo becomes progressively more efficient, amplifying the magnetic field up to values several orders of magnitude larger than the equipartion magnetic field. These very high intensities ($10^{18}\,G$ for the toroidal component and $10^{14}\,G$ for the poloidal one) may seem unphysical at first sight; however, here we are considering magnetic fields still inside the neutron star and only the poloidal component is thought to emerge afterwards. Determining the critical period accurately is important for constraining the fraction of neutron stars that may undergo this magnetic-field amplification at birth, and we have found that P_c is in the range $33 - 600\,{\rm ms}$ for $C_\Omega = 0$, becoming larger as the degree of differential rotation (C_Ω) is increased. As a result, as long as we have no general constraints on the strength of the differential rotation, a lower limit of $P \simeq 30$ ms can be taken as the generic threshold below which a mean-field dynamo may be active in a newly born PNS.

Another interesting result of this investigation is that, despite the large parameter space considered, the final value of the magnetic field seems to follow a surprisingly robust

dependence on the spin period and the degree of differential rotation, both of which can be summarized in a phenomenological expression of the type

$$\mathcal{B}^{\rm fin} \propto (C_\alpha)^\delta |q|^\gamma \tag{3.33}$$

which holds only for $|q|$ larger than a transition level of differential rotation $|q^*|$, whose exact value depends on the configuration and on the other parameters (overall it is in the range $10^{-2} - 10^1$). The exponents $\delta,\ \gamma$ are different for the toroidal and poloidal magnetic field components and depend only very weakly on all of the parameters varied in this analysis. In particular, for the toroidal magnetic field component we have found $\delta \sim 1$ and $\gamma \sim 1/2$, while for the poloidal one $\delta \sim 0$ and $\gamma \sim -1/2$. The exact values of these exponents are likely to be modified by more realistic and multidimensional calculations, but we also expect that the scaling in expression (3.33) will persist in further refinements of this treatment.

The work presented here could be improved in a number of different ways. A first way is to give a more realistic description of the geometry of the problem, with a two or three-dimensional description of the PNS. A second way is to improve the treatment of the nonlinear feedback of the magnetic field on the dynamics of the matter. This could be done still by using the same geometry as adopted here, but coupling the mean field induction equation (3.1) with the solution of the MHD equations for the conservation of energy and momentum.

One could be tempted to take this last option, because it is computationally less expensive and even if it involves solving a number of additional equations, these would still be written in the ambit of a 1D model. However our ultimate aim is to model the magnetic field evolution self-consistently in a 3 dimensional model, thus solving the full set of the MHD equations. In order to do this we have decided to use the publically available ZEUS-MP code, and we considered it best to move on to this code as soon as possible. The next steps are then within the context of parallel computation and so the work takes on a different character. Before moving on to that, we will discuss in the next Chapter our work on accretion flows which follows more closely our approach in the present chapter. We will then return in Chapter 5 to discussing our modification of the ZEUS-MP code to include the additional terms necessary for our further studies. The modified code is then being used for studying the turbulent mean field dynamo in an axisymmetric model of a PNS, a model where we can use more realistic profiles for the differential rotation of the star, still retaining the kinematic approximation. The present status of these calculations is described in Chapter 6.

Bibliography

[1] Becker W., Swartz D., Pavlov W. et al. 2003, ApJ 594, 798

[2] Belvedere G., Pidatella R. M. & Proctor M. R.E. 1990, GAFD 51, 263

[3] Blackman E. G. & Brandenburg A. 2002, ApJ 579, 359

[4] Bonanno A., Rezzolla L. & Urpin V. 2003, A&A 410, L33

[5] Bonanno A., Urpin V. & Belvedere G. 2005, A&A 440, 199

[6] Bonanno A., Urpin V. & Belvedere G. 2006, A&A 451, 1049

[7] Brandenburg A., Krause F., Meinel R., Moss D. & Tuominen I. 1989, A&A 213, 411

[8] Bruenn S. W., Raley E. A. & Mezzacappa A. 2007, astro-ph/0404099

[9] Buras R., Janka H.-Th., Rampp M. & Kifonidis K. 2006, A&A 457, 281

[10] Burrows A. & Lattimer J. 1986, ApJ 307, 178

[11] Covas E., Moss D. & Tavakol R. 2005, A&A 429, 657

[12] Dessart L., Burrows A., Livne E. & Ott C. D. 2006, ApJ 645, 534

[13] Epstein R. 1979, MNRAS 188, 305

[14] Gilman P. A., & Rempel M. 2005, ApJ 630, 615

[15] Livio M., Buchler J. & Colgate S. 1980, ApJ 238, L139

[16] Mezzacappa A., Calder A.C., Bruenn S.W., Blondin J.M., Guidry M.W., Strayer M.R. & Umar A.S. 1998, ApJ 495, 911

[17] Miralles J., Pons J. & Urpin V. 2000, ApJ 543, 1001

[18] Miralles J., Pons J. & Urpin V. 2002, ApJ 574, 356

[19] Moss D. & Brooke J. 2000, MNRAS 315, 521

[20] Pavlov G., Zavlin V., Sanwal D. & Truemper J. 2002, ApJ 569, L95

[21] Rempel M. 2006, ApJ 647, 675

[22] Roald C. B. & Thomas J. H. 1997, MNRAS 288, 551

[23] Rüdiger G. & Arlt R. 1996, A&A 316, L17

[24] Rüdiger G. & Hollerbach R. 2004, The Magnetic Universe: Geophysical and Astrophysical Dynamo (Wiley)

[25] Rüdiger G., Kitchatinov L. L., Küker M. & Schultz M. 1994, GAFD 78, 247

[26] Sanwal D., Pavlov G., Zavlin V. & Teter M. 2002, ApJ 574, L61

[27] Thompson C. & Duncan R. 1993, ApJ 408, 194

[28] Weiss N. O., Cattaneo F. & Jones C. A. 1984, GAFD 30, 305

[29] Xu R. X. & Busse F. H. 2001, A&A 371, 963

Chapter 4

Accretion discs around magnetised neutron stars

The second stage of the magnetic field–plasma interaction considered here is an accretion disc around a magnetised neutron star. We concentrate on finding a stationary magnetic configuration inside the disc, given the neutron star magnetic field, the disc plasma velocity field and the turbulent magnetic diffusivity. Knowing the magnetic field profile is of great importance since magnetic fields play a pivotal role in accretion physics and most of the current models still assume the poloidal component to be dipolar and for the toroidal component analytic models constructed in the mid-80s are still used.

The most relevant literature about the topic that we are interested in is briefly reviewed in Section 4.1. In Section 4.2 we then describe our initial model. We propose a step by step approach, in which we begin by studying the system using a simplified model and we then progressively make it more elaborate. Our aim is to achieve a better understanding of the interplay between the physical quantities involved and for this reason we do not straight away solve the full set of the MHD equations. As for the dynamo in PNSs we work using the kinematic approximation, because as a first step we want to understand the effects of the plasma motion and magnetic diffusivity on the magnetic field configuration. In the subsequent model we will include the magnetic back reaction on the flow.

Even though we are interested in solving the same equation here as in the previous stage (i.e. the induction equation), in this case it is reduced to an elliptic partial differential equation (whereas in the previous case it gave a system of mixed hyperbolic-parabolic type), and therefore we need a different numerical algorithm to obtain the solution. This is described here in detail and afterwards we present and discuss the solutions that we obtain.

4.1 Introduction

Magnetic fields play a fundamental role in the physics of accretion discs. First of all they are thought to be the origin of the turbulence which makes the accretion itself possible: this turbulence is usually thought to be caused by the magneto-rotational instability MRI (Velikov 1959 [32], Chandrasekar 1960 [9], Balbus & Hawley 1991 [3]) although recently other important instabilities have been suggested that can operate even when MRI cannot (sheer-driven instability, Bonanno & Urpin 2006 [5], 2007 [6]; current-driven Tayler instability, Tayler 1973 [30], Rüdiger et al. 2007 [25]). Secondly they can also determine the geometric and kinetic structure of the disc. In addition, magnetic fields are invoked to explain several characteristic features of accreting systems, such as particle collimation (jets), radiation collimation (pulsar lighthouse effect) and spectral line production (cyclotron and synchrotron emission). There are hints that magnetic fields are active even in the dead zones of protoplanetary discs[1] where they transfer angular momentum outwards (Turner & Sano 2008 [31]). Overall, it seems that regardless of the particular kind of accreting system, from ones around supermassive black holes in the centres of galaxies to ones around protostars in star-forming regions, magnetic fields are almost always present and playing some role.

We focus here on studying the properties of accretion discs around magnetised neutron stars. In particular, we are interested in two kinds of system: X-ray pulsars and old neutron stars in the process of being spun-up (recycled) to become millisecond pulsars (MSPs).

X-ray pulsars are members of binary systems which accrete matter from their companion either via stellar winds or via accretion discs with the accretion being funnelled onto the magnetic poles, giving rise to the X-ray pulsing mechanism if the magnetic axis is misaligned with the rotational one. This kind of pulsar is very different from the standard radio pulsars, which radiate away their rotational energy in the form of relativistic particles and magnetic dipole radiation. In X-ray pulsars the accreted matter transfers angular momentum to or from the neutron star causing the spin frequency to increase or decrease at rates that are often hundreds of times faster than the typical spin-down rate in radio pulsars. Some of them are observed to be continuously speeding up or slowing down (with occasional reversals in these trends) while others show either little change in period or display erratic spin-down and spin-up behaviour (see, for example, the review by Bildsten et al. 1997 [4]). Exactly why the X-ray pulsars show such varied spin behaviour is still not clearly understood, but the magnetic field is probably playing an important role in this. X-ray pulsars typically have magnetic fields of $\sim 10^{12}$ G and rotation periods in the range $10^2 - 10^3$ s.

Old pulsars in the process of being "recycled" have lower magnetic fields (typically $\sim 10^8$ G) and are being spun up to millisecond periods by means of accretion from their binary companion via an accretion disc. These are basically radio pulsars but they may

[1] In protoplanetary discs it is thought that MRI drives turbulence only in active layers near the top and bottom surfaces of the disc, where stellar X-rays produce sufficient ionization for good coupling of the gas to magnetic fields. Much of the disc interior remains laminar and is a so-called "dead zone".

also be visible in X-rays during the spin-up. Their relatively weak magnetic fields allow the inner edge of the disc to be close to the surface of the star and this permits a large transfer of angular momentum from the disc to the central object. Once they become MSPs they continue to show some changes in period: timing analysis of MSPs shows that they can either spin-up or spin-down (Di Salvo et al. 2007 [11]) and an explanation for this can again be given in terms of magnetic torques. There has been recent evidence that the standard evolutionary model cannot explain the evolution of all MSPs, especially the young ones with relatively high magnetic fields, e.g. PSR B1937+21. Kiziltan & Thorsett (2009 [17]) showed that different MSPs must form by at least two distinct processes. But the nature of the other process remains a mystery.

In this work we focus mostly on these recycled pulsars, for which the distortions of the magnetic field are larger and at smaller distances from the central object, making the effects easier to see. The behaviour for the X-ray pulsars is expected to be mainly similar, although one must then scale quantities because of the larger inner radius of the disc and intensity of the magnetic field.

Historically our knowledge about systems of accretion discs around magnetized neutron stars took a big leap forward with the observations made by the *Uhuru* satellite (1970). This was the first satellite launched specifically for the purpose of X-ray astronomy and it performed the first comprehensive survey of the entire sky for X-ray sources. After *Uhuru* more than 40 satellites that could observe X-rays were launched, among the most important being *ANS*, *Copernicus*, *SAS-3*, *Ariel V*, *OSO 8*, *HEAO-1* and *HEAO-2*, *ROSAT*, *ASCA*, *RXTE*, *Chandra* and *XMM*.

One of the first important theoretical studies of accretion onto magnetised neutron stars was made by Ghosh, Lamb & Pethick (1977 [13]) who investigated the flow of accreting matter and the magnetic field configuration in the region inside the Alfven surface (taken to roughly coincide with the magnetospheric boundary). They assumed that the disc is completely screened from the field except in a very small transition region, where matter begins to leave the disc and follow the magnetic field lines. Inside the Alfven surface, the matter moves along field lines in the frame corotating with the star. By using the mass conservation equation, the induction equation and the momentum conservation equation, they were able to express the angular velocity Ω and the toroidal magnetic field strength B_ϕ as functions of the ratio between the poloidal velocity and the magnetic field strength $v_\mathrm{p}/B_\mathrm{p}$ for the case of a steady axisymmetric flow with infinite conductivity. In doing this, they assumed that B_p is very close to being a dipolar field and that v_p can be approximated with the free-fall velocity. The transition zone was then used to match this flow solution with the Keplerian flow further out; they could then calculate the rate of change of the rotational energy and angular momentum of the star, and estimate the total torque (spin-up or spin-down) exerted on it.

Applying this model to the case of Her X-1, however, gave a discrepancy, with the theoretically estimated spin-up torque being about 40 times larger than the observed one. This discrepancy can be overcome if the transition region is not thin, and in a subsequent paper Ghosh & Lamb (1979 [14]) noted that there are some mechanisms (Kelvin-Helmotz

instability, turbulent diffusion and magnetic field reconnection) that allow the magnetic field to thread the disc across a very large region. With respect to the previous model, the transition zone is here much wider and they divided it into two sub-regions: the inner boundary layer, where the magnetic stresses are dominant over the viscous ones and the matter begins to leave the disc vertically, and the broad outer transition zone, where the magnetic field is present but does not greatly influence the flow. They numerically solved the mass conservation equation, the momentum conservation equation, Ampere's law and Ohm's law, making a vertical average. Assuming that the disc is thin and that the system is axisymmetric, they looked for a steady solution using an ad hoc prescription for the azimuthal pitch angle ($\gamma_\phi \equiv B_\phi/B_z$). In particular, in the boundary layer they took $B_\phi \sim B_z$, while in the outer transition zone γ_ϕ was obtained by balancing the growth and decay terms for the toroidal magnetic field. They found that most of the screening of the magnetic field occurs in the boundary layer and then B remains almost dipolar throughout the transition region, at the end of which it is put to zero. In this region they found that the differences with respect to a standard α-disc are within factors of 0.5 to 3.

In a subsequent paper Ghosh & Lamb (1979 [15]) used these results to calculate the torque exerted on the neutron star by the accreting plasma. Here they wrote the total torque as the sum of three contributions, coming from the material, magnetic and viscous stresses. They then calculated the torques in the inner and outer transition regions ($N_{\rm in}$ and $N_{\rm out}$ respectively), finding that $N_{\rm in}$ is always positive, while $N_{\rm out}$ can have either sign, depending on the value of the fastness parameter[2] $\omega_{\rm s}$. The faster the star, the smaller is the corotation radius $r_{\rm c}$ and the smaller is $N_{\rm out}$. This is because the part of the outer transition region which contributes positively to the torque is being reduced in size with increasing $\omega_{\rm s}$. In some cases $N_{\rm out}$ becomes negative and can even exceed $N_{\rm in}$ so that the spin of the neutron star is slowed down, even with continuing accretion.

Another possible explanation for having a small total torque or even spin-down comes from the propeller model, where some of the matter is ejected from the disc (Davidson & Ostriker 1973 [10]; Illarionov & Sunyaev [16] 1975; Shakura 1975 [27]). Another possible mechanism for angular momentum loss is via gravitational wave emission, which would occur if the pulsar has some mass (or mass-current) asymmetry around its rotation axis (see Abbott et al. [1]). Searching for the gravitational waves coming from this is currently the subject of an extensive international collaborative effort.

The B_ϕ generation mechanism and the magnetic torque were re-considered by Wang (1987 [33]) and Campbell (1987 [7], 1992 [8]). Wang showed that the particular pitch angle distribution used by Ghosh & Lamb [14] is not consistent, since the resulting magnetic pressure would disrupt the disc beyond the corotation point. In the Wang and Campbell models, the induction equation was solved in order to find a steady solution for the magnetic field. The poloidal field was taken to be dipolar and the toroidal field was calculated assuming axisymmetry. The induction equation was greatly simplified by restricting the analysis to a region near the equatorial plane (where B_r and v_r can be neglected with

[2]The fastness parameter is defined as $\omega_s \equiv \Omega_s/\Omega_K(r_0)$, where $\Omega_{\rm s}$ is the angular velocity of the star and r_0 is radius of the boundary between the inner and outer transition zones, where the Keplerian flow ends.

respect to the other components) and by supposing that the disc is Keplerian[3] and that the vertical flow is negligible. As a result, the generation of toroidal field is then only due to the vertical gradient of the azimuthal velocity v_ϕ. Within these models, the magnetosphere above the disc is taken to corotate with the neutron star. The small region where the transition from corotation (outside the disc) to Keplerian rotation (inside the disc) occurs is where the toroidal field is generated. The magnetic torque is then calculated and, depending on the radii of the inner edge of the disc and of the corotation point $r_{\rm c}$, can either spin-up or spin-down the neutron star.

Miller & Stone (1997 [22]) performed 2D numerical simulations with the resistive MHD equations in order to study the evolution of the interaction region between the inner edge of the disc and the magnetosphere which was assumed to be initially in equilibrium, corotating with the neutron star, and threaded by one of three different initial magnetic field topologies. They found that regardless of the initial topology there is a rapid evolution of the disc, driven by the angular momentum transport. In most cases, equatorial accretion results, either because accumulation of matter makes the gas pressure exceed the magnetic pressure or because the magnetic field geometry is such that polar accretion is inhibited. Polar accretion only occurs when a strong global vertical magnetic field is included. Their simulations also confirmed the failure of total screening of the magnetic field from the accretion disc. In fact one of their initial magnetic field topologies was a dipole which was completely excluded from the disc by surface currents. In this case the disc would be pushed outward radially by the magnetic tension if the diffusivity were zero. However, if the disc is resistive, the field will diffuse into it before it is swept off, both relieving the tension force, and producing angular momentum transport in the disc. In this simulation the field penetration into the disc was solely due to magnetic diffusion, since the Kelvin-Helmotz instability excites non-axisymmetric modes and therefore cannot be modelled in a 2D simulation.

Many investigators after Miller & Stone have simulated the magnetosphere–disc interaction, solving the full set of the MHD equations (see e.g. Romanova et al 2002 [24] and Kulkarni & Romanova 2008 [20]). The work that we are carrying out here should not be seen as being in competition with these analyses, but rather as being complementary to them. As we mentioned in Chapter 1, Section 1.2, our approach here is to use a succession of simplified models, becoming progressively more sophisticated, and to proceed step by step so as to fully understand the effect of each successive additional feature as it is introduced. In large-scale numerical work, one sees the results of an interacting set of inputs within the scope of the adopted model assumptions and numerical techniques. Deconstructing this, so as to have a clear conceptual understanding of the role of each of the different components, remains a valuable thing to do and an approach which needs to be carried on alongside the large-scale simulations. The conceptual papers from the 1970s and 1980s, mentioned above, continue to be widely quoted and used as the basis for new research (see, for example, Kluzniak & Rappaport 2007 [18]) and our work here stands in the tradition of refining these approaches.

[3]Campbell also considered non-Keplerian discs.

Following a somewhat similar strategy to ours, Agapitou & Papaloizou (2000 [2]) looked for steady-state axisymmetric configurations of a force-free magnetosphere by means of simplified numerical calculations. They considered all of the region from the rotation axis to the equator, for several values of the radius of the outer edge of the disc and ignored the internal dynamics of the disc. In their model the disc is assumed to have only an azimuthal velocity; it is taken to be thin and therefore radial derivatives are neglected with respect to vertical ones. They found that the poloidal field can differ significantly from the dipole field of the central star. Within the corotation radius the differences are negligible, but immediately outside this, the poloidal field becomes smaller than the dipolar one, and then, at a larger radius (whose exact value depends on the position of the outer edge of the disc), it eventually becomes larger than the dipolar one. As regards the magnetic torque, they found that it can be much smaller than that estimated by assuming $B_z \sim B_{\rm dip}$. They also considered two different configurations for the magnetosphere, obtained with two different outer boundary conditions: in one case the field was tangential to the outer boundary (which is at a radius equal to the outer edge of the disc) while in the other case it was normal to the boundary. They showed that in cases favouring large field line inflation and open field lines (the ones with the normal field) the spin-down magnetic torque becomes very small.

Elstner & Rüdiger (2000 [12]) addressed the problem from a complementary viewpoint, considering the influence of a given stellar magnetic field on the structure of the accretion disc in terms of height and surface density. They also considered the back reaction on the magnetic field, solving both the induction equation and the disc-diffusion equation (using different time steps). The calculations were performed in 2D for the induction equation and in the 1+1D approximation for the disc equation. They fixed the disc rotation to be Keplerian and took zero-velocity in the corona (above and below the disc) while for the diffusivity they used the same value in the disc and in the corona. With this model, they showed that the expression obtained by Wang (1987 [33]) and Campbell (1987 [7]) for the toroidal magnetic field is still valid to within a factor of $0.5 - 1.5$ on average; this factor changes with radius and can be as small as 0.2 for large radii. They found that the outer disc is hotter, thicker and more massive than in the corresponding non-magnetic solutions, because of the magnetically-driven angular momentum flow from the central object to the outer disc. Their numerical calculations focussed on accretion in classical T-Tauri systems.

Shalybkov & Rüdiger (2000 [29]) and Rüdiger & Shalybkov (2002 [26]) studied the vertical structure of thin accretion discs by solving the momentum equation, the induction equation and the energy equation, which they expanded to lowest order in H/r. They gave results for the magnetic field strength, rotation speed, radial velocity and density as functions of z for an arbitrary value of the radius (in cylindrical coordinates). They saw no large departure of the angular velocity away from Keplerian, but found that the radial velocity could increase drastically in some specific configurations. Their main result concerned the inclination angle of the magnetic field lines to the rotation axis. They found that, when the radial infall velocity is large, a small magnetic Prandtl number can already produce inclinations exceeding the critical value of 30°, required for launching

cold jets.

Our aim in the present work is to find a stationary configuration of the magnetic field inside the disc and the surrounding corona (taken as a layer above and below the disc), without making any leading order expansion or vertical integration, i.e. using a fully 2D model. We want to study the effects of the important physical quantities (the radial, vertical and angular velocities, the diffusivity, the accretion rate, etc.) on the structure of the magnetic field, and in turn on the magnetic torque, in order to give an estimate for the field in the disc which is more realistic than the analytical ones developed by Wang and Campbell. As mentioned earlier, in our initial model presented in this Chapter we make use of the kinematic approximation and solve only for the induction equation, from which one can analyse how the plasma velocity and the turbulent diffusivity affect the magnetic field. As we will show later, since the system is taken to be axisymmetric and in a stationary state, the induction equation can be split into two parts, one in which only the poloidal component of the magnetic field appears and the other containing all of the components. Here we present results only for the poloidal field. The toroidal component will be calculated subsequently. Once the analyses with the initial model are complete we intend to improve the model by including the back reaction of the magnetic field on the plasma motion, thus solving for the Euler equation as well.

4.2 Our Model

In this study we consider disc accretion by a neutron star having a dipolar magnetic field with magnetic moment μ. We assume that the star is rotating around its magnetic axis, and that this axis is perpendicular to the disc plane; also, we assume that the fluid flow is steady and has axial symmetry everywhere. Of course, all pulsars must be oblique rotators in order to be observed as such, and so the system would not then be axisymmetric as a matter of principle. The inclination of the magnetic axis with respect to the rotation axis can have various consequences, e.g. the shape of the impact region on the stellar surface would be changed, the magnetic force would become time dependent, and the accretion torque could drive a precession of the star. However we are not concerned here with studying these aspects of accreting systems and moreover the principles of the interaction between the magnetic field and the plasma in the disc are not affected by the inclination. We therefore feel that retaining the assumption of the magnetic axis being perpendicular to the disc is satisfactory for our purposes. For our calculations, we use spherical coordinates (r, θ, ϕ), with the origin being at the centre of the neutron star.

The general flavour of our model is similar to that of Ghosh & Lamb (1979 [14], hereafter GL). We suppose that at large radii the magnetic pressure is negligible with respect to the gas pressure and the disc can be described as a standard α-disc. As one moves inwards however the magnetic field becomes progressively stronger, eventually dominating over the gas pressure so that most of the matter leaves the disc following magnetic field lines and the disc is disrupted. We note that some equatorial accretion continue to be possible even with a rather high stellar magnetic field, as shown by Miller & Stone

[22].

There are some differences between our model and that of GL. We are not assuming the existence of a wide transition zone where the field is progressively screened, eventually disappearing at the outer boundary of the zone. Also, we do not force the field to be zero at the outer boundary; we instead take it to be dipolar there and we do the same at all of the remaining boundaries too. We put the radial outer boundary very far away so that the solutions in the zone of interest, which goes from the inner edge of the disc out to the light cylinder, will not be very sensitive to the conditions at the outer edge. We note here that, if we take the innermost part of the disc to have very high diffusivity, we naturally find a narrow inner region followed by a broad outer one, however the behaviour of the field in these regions is quite different from that in the GL model. In their model the field is reduced by screening currents by a factor of about 80 per cent in the boundary layer and then decreases as a dipole field in the first third of the outer zone, after which it is forced by the boundary conditions to go to zero. In our model, instead, the field is almost dipolar in the region nearest to the star (which we define as the inner region), is amplified by a factor ~ 3 where the diffusivity changes value (we call this the transition region), then decreases to a value lower than the dipole one and finally decays almost as a dipolar field (we call this the main region).

As regards the inner edge of the disc, its precise location is still an open issue and several prescriptions have been suggested[4], however none of them differs very much from the Alfven radius calculated using a dipolar magnetic field (i.e. the radius where the dipolar magnetic field pressure equals the gas pressure). For our present model we adopt this as being the inner edge of the disc; for subsequent models, a possible improvement will be to calculate the Alfven radius using the stationary magnetic field obtained in this work instead of the dipolar one.

We suppose that all around the pulsar there is vacuum, except for where we have the disc and the corona (taken to be a layer above and below the disc), and that the field remains dipolar from the surface of the star until it reaches the matter in the corona. In reality, taking vacuum is not completely correct, both because the density in the magnetosphere is not zero and because between the star and the disc there is the matter which is accreting onto the neutron star. For the latter, we suppose that the flow of this material is perfectly aligned with field lines and that it has very low density, so that we can neglect its influence on the magnetic field structure. Furthermore we are introducing a low density corona in order to have a transition zone between the disc and the vacuum. We also allow the velocity and the diffusivity to have a different value in the corona (we will comment on this later in the present Section).

Summarizing, we model the system as being composed of 4 regions (see figure 4.1): (1) a central object, surrounded by (2) an accretion disc, on top of which there is (3) a corona; all of the rest is taken to be (4) vacuum. Each physical quantity is allowed to have different values in each of the regions. Our numerical domain covers regions (2) and

[4]The different suggestions can be divided into three types according to whether they assume that the inner radius is determined by energy, stress or pressure balance.

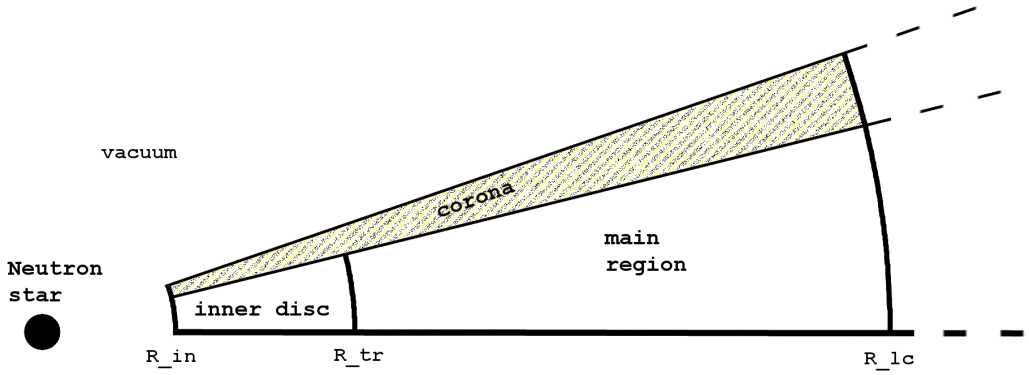

Figure 4.1: Geometrical representation of our model (the drawing is not exactly to scale). The radius values which we use are: $R_{\rm in} \sim 10\, r_{\rm g}$, $R_{\rm tr} \sim 22\, r_{\rm g}$ and $R_{\rm lc} \sim 115\, r_{\rm g}$ and the opening angles are about 8° for the disc alone and 10° for disc plus corona. The numerical outer boundary is much further out than the region of interest shown here; the grid continues until $r \sim 750\, r_{\rm g}$ (this is the reason for the dashed lines).

(3). Since these two regions are surrounded by vacuum and the stellar field is dipolar, we impose dipole boundary conditions at all of the boundaries. We are aware that in real astrophysical systems this dipole condition at the boundaries can be rather drastic since the region outside the neutron star is not vacuum and the field is distorted well before reaching the disc. However at our level of analysis the results are not thought to be very sensitively dependent on the precise profile chosen for the magnetic field at the boundaries, and we are here focusing on studying the influence on the magnetic configuration of the velocity field and diffusivity. That this is reasonable is confirmed by the fact that the magnetic configuration that we obtain is rather similar to that obtained by the numerical simulations of other authors [22] which had a different treatment of the boundary conditions. However this will be the subject of further investigation in an ongoing work. We take the ratio H/r to be constant (where H is the semi-thickness of the disc), and so the entire upper surface of the disc is located at a single value of the colatitude θ (as also is the case for the corona). In particular, we take an opening angle of 8° for the disc (measuring from the equatorial plane to the top of the disc), implying $H/r \sim 0.14$, and of 10° for the disc plus the corona.

As will be described in Section 4.3, we here consider only the poloidal component of the induction equation. Once the magnetic diffusivity η and the poloidal velocity $\mathbf{v_p}$ are specified, this can be solved to obtain the configuration of the poloidal field without entering into details of the toroidal component. As regards the turbulent magnetic diffusivity, we take this to have a constant value η_0 in the main disc region and to be $\eta_{\rm c} = 100 \cdot \eta_0$ in the corona and in the inner part of the disc (we join the different parts smoothly, using error functions). We take higher values there because these regions are

less dense and therefore we expect the effects of turbulence to be enhanced there. However as we move away from the corona into the vacuum the density drops to zero and turbulence eventually disappears[5].

As regards the velocity: for v_r we use the expression given for the middle region of α-discs[6] by Shakura & Sunyaev (1973 [28]); while we put v_θ to zero inside the disc, although allowing it to be non-zero in the corona as necessary in order to be consistent with the dipole boundary conditions. In Section 4.3.2, we find that whenever a dipole field is a solution of the induction equation, a precise relationship must hold between v_r and v_θ, subject to certain reasonable conditions. We use this relation to calculate v_θ in the corona.

Figure 4.1 shows a schematic representation of the geometry of our model, the corona and the two parts of the disc being shown (the transition region is thin and around $r = R_{\rm tr}$). The dashed lines indicate that in solving the induction equation we use a much larger numerical domain, so that in the zone of interest the solution is almost independent of the location of the outer boundary.

4.3 The Equations

As for the PNS case we are interested in solving the induction equation when there is a large magnetic diffusion due to turbulent motions. This equation has been derived in Chapter 2, Section 2.3, and but we report it again here:

$$\partial_t \mathbf{B} = \nabla \times (\mathbf{v} \times \mathbf{B} + \mathcal{E} - \eta_{\rm Ohm} \nabla \times \mathbf{B}) \tag{4.1}$$

where $\eta_{\rm Ohm} = c^2/4\pi\sigma$ is the Ohmic diffusivity and $\mathcal{E}$ is the turbulent electromotive force, that in the first-order smoothing approximation is written as $\mathcal{E} = \alpha\mathbf{B} - \eta_{\rm T}\nabla \times \mathbf{B}$. In the present model we are not considering any dynamo action, therefore we neglect the α term, which can however be included in a more elaborate subsequent model. This is in line with our approach, which is aiming at understanding, one at a time, the effects of the various elements which characterize the system of an accretion disc around a magnetised neutron star.

The induction equation then reduces to:

$$\partial_t \mathbf{B} = \nabla \times (\mathbf{v} \times \mathbf{B} - \eta \nabla \times \mathbf{B}) \tag{4.2}$$

where $\eta = \eta_{\rm Ohm} + \eta_{\rm T} \sim \eta_{\rm T}$, because the turbulent diffusivity is much larger than the Ohmic one in the disc and in the corona.

Since we are interested in stationary solutions, we put the time derivatives to zero, as

[5] It is only the turbulent diffusivity $\eta_{\rm T}$ which disappears, the Ohmic one $\eta_{\rm Ohm}$ will always be present, therefore in vacuum $\eta = \eta_{\rm Ohm} \ll \eta_{\rm T}$.

[6] In the α-disc model for accretion onto black holes, three regions are present: inner, middle and outer. Only the middle region is used in our case. For the parameter values which we are using, the magnetic field disrupts the disc within the boundary between the inner and middle regions, while the outer boundary of the middle region is much further out than our region of interest, at about $6.08\,10^2 \cdot \left(\frac{\dot{m}}{0.03}\right)^{2/3}$.

we do also for the ϕ derivatives since we are assuming axisymmetry. Then in spherical coordinates the three components of equation (4.2) are:

$$0 = \partial_\theta \left\{ \sin\theta \left[v_r B_\theta - v_\theta B_r - \frac{\eta}{r}[\partial_r(rB_\theta) - \partial_\theta B_r] \right] \right\} \tag{4.3}$$

$$0 = \partial_r \left\{ r \left[v_r B_\theta - v_\theta B_r - \frac{\eta}{r}[\partial_r(rB_\theta) - \partial_\theta B_r] \right] \right\} \tag{4.4}$$

$$0 = \partial_r \left\{ r \left[v_\phi B_r - v_r B_\phi + \frac{\eta}{r}\partial_r(rB_\phi) \right] \right\} - \partial_\theta \left\{ v_\theta B_\phi - v_\phi B_\theta - \frac{\eta}{r\sin\theta}\partial_\theta(B_\phi \sin\theta) \right\} \tag{4.5}$$

The first two of these equations have the same expression inside the large square brackets and we call this $\mathcal{F}$. We can then reduce these two equations to a single equation and write the entire system as:

$$\mathcal{F} = \frac{k}{r\,\sin\theta} \tag{4.6}$$

$$0 = \partial_r \left\{ r \left[v_\phi B_r - v_r B_\phi + \frac{\eta}{r}\partial_r(rB_\phi) \right] \right\} - \partial_\theta \left\{ v_\theta B_\phi - v_\phi B_\theta - \frac{\eta}{r\sin\theta}\partial_\theta(B_\phi \sin\theta) \right\} \tag{4.7}$$

where k is a generic constant.

We notice that $\mathcal{F}$ depends only on the turbulent magnetic diffusivity η and on the poloidal components of the velocity field and the magnetic field. It is clear therefore that equation (4.6) alone governs the poloidal part of the magnetic field and is independent of any azimuthal quantity, while to obtain the toroidal component of the magnetic field one has to solve the further equation (4.7).

In this thesis we concentrate only on solving equation (4.6). Subsequently we will use the results obtained here to solve equation (4.7) and calculate the toroidal field component.

In order to guarantee that the condition $\nabla \cdot \mathbf{B} = 0$ is satisfied and to be able to calculate the magnetic field lines easily, we write the magnetic field components in terms of the magnetic stream function $\mathcal{S}$, which is implicitely defined by the following two equations:

$$B_r = \frac{1}{r^2 \sin\theta}\,\partial_\theta \mathcal{S}(r,\theta) \tag{4.8}$$

$$B_\theta = -\frac{1}{r\sin\theta}\,\partial_r \mathcal{S}(r,\theta) \tag{4.9}$$

With this definition, the axisymmetric field $\mathbf{B}$ is always solenoidal and isolines of $\mathcal{S}$ represent magnetic field lines. Substituting these expressions into eq. (4.6), we obtain an elliptic partial differential equation (PDE) for $\mathcal{S}$ in terms of r and θ:

$$\partial_r^2 \mathcal{S} + \frac{1}{r^2}\partial_\theta^2 \mathcal{S} - \left(\frac{\cot\theta}{r^2} + \frac{v_\theta}{r\,\eta} \right) \partial_\theta \mathcal{S} - \frac{v_r}{\eta}\partial_r \mathcal{S} = \frac{k}{\eta} \tag{4.10}$$

where k is the constant introduced above in equation (4.6) and v_r, v_θ and η are non-constant coefficients. This equation can be solved once boundary conditions and values for the coefficients have been specified.

4.3.1 Velocity field and turbulent diffusivity

In Section 4.2 we qualitatively described the profiles of velocity and diffusivity that we are using. Here we give the precise expressions.

For the velocity, we use the expression given by Shakura & Sunyaev (1973 [28]) for their region b:

$$v_r(r) = 2\,10^6 \cdot \alpha^{4/5} \cdot \dot{m}^{2/5} \cdot m^{-1/5} \cdot (3/r)^{2/5} \left[1 - (3/r)^{0.5}\right]^{-3/5} \mathrm{cm\,s^{-1}} \tag{4.11}$$

where the radius r is expressed in units of the Schwarzschild radius, m is given in solar mass units, $\dot{m}$ is in units of the critical Eddington rate and α is the standard Shakura-Sunyaev viscosity coefficient. Using typical values ($\alpha = 0.1$, $\dot{m} = 0.03$ and $m = 1.4$) one obtains:

$$v_r(r) \approx 7.3\,10^4 \cdot (3/r)^{2/5} \left[1 - (3/r)^{0.5}\right]^{-3/5} \mathrm{cm\,s^{-1}} \tag{4.12}$$

For the other component of the poloidal velocity, v_θ, we set this to zero in the disc and use a non-zero profile in the corona. The formula for this is calculated in Subsection 4.3.2; we anticipate here the result:

$$v_\theta = \begin{cases} 0 & \text{in the disc} \\ \frac{1}{2}\, v_r\, \tan\theta & \text{in the corona} \end{cases} \tag{4.13}$$

For the diffusivity, we first construct two auxiliary functions, η_θ and η_r, giving the profiles along the θ and r directions respectively:

$$\eta_\theta = \left[1 + \mathrm{erf}\left(\frac{-\theta + \theta_\mathrm{c}}{\mathrm{d}_\theta}\right)\right] \tag{4.14}$$

$$\eta_r = \left[1 + \mathrm{erf}\left(\frac{-r + r_{\eta\,\mathrm{in}}}{d_r}\right)\right] + \left[1 + \mathrm{erf}\left(\frac{r - r_{\eta\,\mathrm{out}}}{d_r}\right)\right] \tag{4.15}$$

where θ_c is the colatitude of the upper surface of the disc, $r_{\eta\,\mathrm{in}}$ is the radius of the boundary between the inner region and the main disc region[7] and d_θ and d_r are the widths of the error functions used for the angular and radial profiles respectively. We then combine equations (4.14) and (4.15) to get the global η:

$$\eta(r,\theta) = \eta_0 \cdot \left[1 + \frac{1}{2} \cdot (\eta_\theta + \eta_r) \cdot \left(\frac{\eta_\mathrm{c}}{\eta_0} - 1\right)\right] \tag{4.16}$$

[7] $r_{\eta\,\mathrm{out}}$ appearing in the expression for η_r is located shortly before r_out and far away from the zone of interest.

where η_0 and η_c are dimensional quantities (with units of cm^2 s^{-1}), the former giving the value of the diffusivity in the main disc region and the latter giving the value in the corona and the inner disc region.

4.3.2 Dipolar solution, an analytic constraint

In order to obtain a profile for v_θ, we consider the situation when the stationary magnetic field is dipolar in some part of the disc. More precisely, we suppose that from the top surface of the corona, where $\theta = \theta_{\rm surf}$, down to some $\theta = \tilde{\theta}$ we have $\mathbf{B} = \mathbf{B}_{\rm dip}$, i.e. $(B_r, B_\theta, B_\phi) = \left(\frac{2\mu \cos\theta}{r^3}, \frac{\mu \sin\theta}{r^3}, 0\right)$ where μ is the magnetic dipole moment.

A magnetic dipole field is current-free (i.e. $\mathbf{J} = \nabla \times \mathbf{B} = 0$), therefore when $\mathbf{B} = \mathbf{B}_{\rm dip}$ is a stationary solution of the induction equation, equation (4.2) becomes:

$$\nabla \times (\mathbf{v} \times \mathbf{B}) = 0 \tag{4.17}$$

Following a procedure similar to that used for obtaining equations (4.6) and (4.7), we go to spherical coordinates, write out the three component equations and group the poloidal terms. This gives:

$$v_r\, B_\theta - v_\theta\, B_r = \frac{\tilde{k}}{r\, \sin\theta} \tag{4.18}$$

$$\partial_r (r\, v_\phi\, B_r) = -\partial_\theta (v_\phi B_\theta) \tag{4.19}$$

Since $\tilde{k}$ is a constant we can calculate it at any convenient location. We consider a path with constant θ, e.g. $\theta = \theta^* \in [\theta_{\rm surf}, \tilde{\theta}]$; along this path equation (4.18) gives:

$$v_r \left(\frac{\mu\, \sin\theta^*}{2}\right) - v_\theta\, (\mu\, \cos\theta^*) \;\; = \;\; r^2 \left(\frac{\tilde{k}}{\sin\theta^*}\right) \tag{4.20}$$

where all of the terms in the brackets are constant. To investigate further the properties of this equation, consider the situation if $v_\theta = 0$. Equation (4.20) would then imply that either $v_r \propto r^2$ (which is not reasonable for an accretion flow) or $v_r = 0$, i.e. $\tilde{k} = 0$, so that there is no accretion at all. This implies that if we have an accreting flow in a region with a dipole magnetic field then v_θ must be non zero. We do not know the exact profiles of v_r and v_θ, but it is not plausible that the left hand side increases as r^2 and so we need to choose $\tilde{k} = 0$. Therefore from the last equation we get:

$$v_r\, \frac{\sin\theta}{2} = v_\theta\, \cos\theta \rightarrow v_\theta = \frac{1}{2}\, \tan\theta\, v_r \tag{4.21}$$

Equation (4.21) implies not only that if there is a non-zero radial velocity then there must be a non-zero vertical velocity as well, but also that the vertical velocity is larger than the radial one (at $\theta = 81\,^\circ$ one has $v_\theta \sim 13\, v_r$).

From equation (4.19) one can obtain information about v_ϕ. As expected $v_\phi = 0$ is a pos-

sible solution but $v_\phi = v_{\rm Kep}$ is not, meaning that having a dipolar field is not consistent with having a Keplerian angular velocity profile, whereas it is consistent with having no rotation. It is interesting to notice that there are also some non trivial profiles which are solutions. For example $v_\phi \propto r^{-\alpha} \cdot \sin^{3+2\delta}\theta$, where δ is a positive integer, gives a set of possible solutions[8]. Therefore if one supposes that v_ϕ decreases with r as a power law, then it must have also a dependence on θ in order for the magnetic field to be dipolar. We recall that in the works of Campbell and Wang it is precisely the vertical gradient of the angular velocity that produces the toroidal field. Here we have shown that it is possible to have a non-zero vertical gradient of the angular velocity and still have a zero toroidal magnetic field. However, we stress that we are not giving physical explanations for having these kinds of velocity profile.

Summarizing: a dipolar magnetic field can be a stationary solution of the induction equation provided that the velocity satisfies equations (4.18) and (4.19), which then implies that, unless the plasma in the disc has zero radial velocity (i.e. is not accreting), an outflow away from the disc is unavoidable. Also, having the rotation velocity depending on r and θ is, in principle, allowed.

We should note here that equation (4.17) has been solved in the context of stellar winds by Mestel (1961 [21]); his result was that the poloidal magnetic field and velocity field need to be parallel. Our result that $v_r/B_r = v_\theta/B_\theta$ (from equation (4.18) with $\tilde{k} = 0$) is in agreement with his.

4.4 The Code

In the previous Section we have seen how finding the configuration of the magnetic field reduces to solving an elliptic PDE for the stream function $\mathcal{S}$ (equation (4.10)), whose non-constant coefficients are now all known. As regards the quantity k on the right hand side of the equation: at the boundary, where the magnetic field is dipolar[9], this must be zero. Then, since it is a constant, it must be zero everywhere. In this Section we first put the equation in a dimensionless form, then we describe the algorithm that we use to solve it, and finally we discuss some of the tests that we have performed on the code.

4.4.1 Dimensionless equation

In order to write equation (4.10) in a dimensionless form, we scale the quantities in the following way:

$$r = \hat{r}\, r_{\rm g} \qquad \theta = \hat{\theta} \qquad \mathcal{S} = \hat{\mathcal{S}}\, \mathcal{S}_0 \tag{4.22}$$

[8] This can be seen by writing v_ϕ as the product of a function of r and a function of θ and carrying out some simple algebra.

[9] Boundary conditions are imposed on the magnetic stream function: $\hat{\mathcal{S}} = \hat{\mathcal{S}}^{\rm dip} = r_0\, \sin^2 y/x$.

where the hat quantities are dimensionless, $r_{\rm g}$ is the Schwarzschild radius, η_0 is the value of the diffusivity in the main disc region and $\mathcal{S}_0$ is a reference value for the stream function, calculated as the value for a dipolar field on the equator of the neutron star. Substituting into equation (4.10) we get:

$$\frac{\mathcal{S}_0}{r_{\rm g}^2}\,\partial^2_{\hat{r}}\hat{\mathcal{S}} + \frac{\mathcal{S}_0}{r_{\rm g}^2\hat{r}^2}\,\partial^2_{\hat{\theta}}\hat{\mathcal{S}} - \left(\frac{\cot\hat{\theta}}{r_{\rm g}^2\hat{r}^2} + \frac{v_\theta}{r_{\rm g}\hat{r}\,\eta}\right)\mathcal{S}_0\partial_{\hat{\theta}}\hat{\mathcal{S}} - \frac{v_r}{\eta}\,\frac{\mathcal{S}_0}{r_{\rm g}}\partial_{\hat{r}}\hat{\mathcal{S}} = 0 \tag{4.23}$$

$$\partial^2_{\hat{r}}\hat{\mathcal{S}} + \frac{1}{\hat{r}^2}\partial^2_{\hat{\theta}}\hat{\mathcal{S}} - \left(\frac{\cot\hat{\theta}}{\hat{r}^2} + \frac{v_\theta\, r_{\rm g}}{\hat{r}\,\eta}\right)\partial_{\hat{\theta}}\hat{\mathcal{S}} - \frac{v_r r_{\rm g}}{\eta}\partial_{\hat{r}}\hat{\mathcal{S}} = 0 \tag{4.24}$$

where we go from (4.23) to (4.24) by dividing both sides by $\mathcal{S}_0/r_{\rm g}^2$. We rename the variables ($x = \hat{r}$ and $y = \hat{\theta}$) and obtain the following dimensionless form for the equation:

$$\partial^2_x\hat{\mathcal{S}} + \frac{1}{x^2}\partial^2_y\hat{\mathcal{S}} - \left(\frac{\cot y}{x^2} + \frac{v_\theta\, r_{\rm g}}{x\,\eta}\right)\partial_y\hat{\mathcal{S}} - \frac{v_r\, r_{\rm g}}{\eta}\,\partial_x\hat{\mathcal{S}} = 0 \tag{4.25}$$

where $[v_r] = [v_\theta] = \text{cm s}^{-1}$, $[r_{\rm g}] = \text{cm}$, $[\eta] = \text{cm}^2\ \text{s}^{-1}$, so that $v_r\, r_{\rm g}/\eta$ and $v_\theta\, r_{\rm g}/\eta$ are dimensionless coefficients.

As mentioned above, the reference value for the stream function is taken to be its value at the equator of the neutron star. If we call the star's radius $\hat{r}_0\, r_{\rm g}$ then $\mathcal{S}_0 \equiv \mathcal{S}^{\rm dip}(\hat{r}_0\, r_{\rm g},\, \pi/2) = \mu\,(\hat{r}_0\, r_{\rm g})^{-1}$. The solution of equation (4.25) gives the dimensionless stream function $\hat{\mathcal{S}}$. In order to calculate the magnetic field, we first calculate $\hat{B}_{\rm pol}$ using the dimensionless versions of equations (4.8) and (4.9), and then multiply by B_0 to go to physical units, where $B_0 \equiv B_\theta^{\rm dip}(r = \hat{r}_0\, r_{\rm g},\, \theta = \pi/2)$.

4.4.2 Description of the code

In order to solve the 2D elliptic PDE (4.25) we use the Gauss-Seidel relaxation method. If we call the elliptic operator $\mathcal{L}$ and the right hand side b, then the original equation becomes: $\mathcal{L}[\mathcal{S}] = b$. We turn this elliptic equation into a hyperbolic one by adding a pseudo time derivative; we can then consider the iterative procedure as a time evolution and write: $\partial_t\mathcal{S} = \mathcal{L}[\mathcal{S}] - b$. In our case $\mathcal{L} = \partial^2_x + \frac{1}{x^2}\partial^2_y - \left(\frac{\cot y}{x^2} + \frac{v_\theta\, r_{\rm g}}{x\,\eta}\right)\partial_y - \frac{v_r\, r_{\rm g}}{\eta}\,\partial_x$ and $b = 0$.

As in the PNS case. we use a finite difference technique, approximating the operators by discretizing the functions over a grid. The scheme that we use for discretizing the derivatives is as follows:

$$\partial_\theta\mathcal{S}|_{i,j} = \frac{\mathcal{S}_{i,j+1} - \mathcal{S}_{i,j-1}}{2\Delta j} \quad \text{and} \quad \partial^2_\theta\mathcal{S}|_{i,j} = \frac{\mathcal{S}_{i,j+1} - 2\mathcal{S}_{i,j} + \mathcal{S}_{i,j-1}}{\Delta j^2} \tag{4.26}$$

$$\partial_r\mathcal{S}|_{i,j} = \frac{\mathcal{S}_{i+1,j} - \mathcal{S}_{i-1,j}}{2\Delta i} \quad \text{and} \quad \partial^2_r\mathcal{S}|_{i,j} = \frac{\mathcal{S}_{i+1,j} - 2\mathcal{S}_{i,j} + \mathcal{S}_{i-1,j}}{\Delta i^2} \tag{4.27}$$

$$\partial_t \mathcal{S} = \frac{\mathcal{S}^{t+1} - \mathcal{S}^t}{\Delta t} \tag{4.28}$$

We use these expressions to discretize equation (4.25) and then, isolating the term $\mathcal{S}^{t+1}_{i,j}$, we get the iterative algorithm that we use in our code:

$$\begin{aligned} \mathcal{S}^{t+1}_{i,j} &= \mathcal{S}^t_{i,j} + \Delta t \left[\frac{\mathcal{S}^t_{i+1,j} - 2\mathcal{S}^t_{i,j} + \mathcal{S}^{t+1}_{i-1,j}}{\Delta i^2} + \frac{1}{x_i^2} \frac{\mathcal{S}^t_{i,j+1} - 2\mathcal{S}^t_{i,j} + \mathcal{S}^{t+1}_{i,j-1}}{\Delta j^2} + \right. \\ &\left. - \left(\frac{\cot y_j}{x_i^2} + \frac{v_\theta \, r_\mathrm{g}}{x_i \, \eta} \right) \frac{\mathcal{S}^t_{i,j+1} - \mathcal{S}^{t+1}_{i,j-1}}{2\Delta j} - \frac{v_r \, r_\mathrm{g}}{\eta} \frac{\mathcal{S}^t_{i+1,j} - \mathcal{S}^{t+1}_{i-1,j}}{2\Delta i} \right] \end{aligned} \tag{4.29}$$

We solve this proceeding outwards from $i = 1$, $j = 1$; on the right hand side the terms that have already been calculated (i.e. the terms at positions $i = i - 1$ and $j = j - 1$) are taken at the current iteration $t + 1$, as usual in the Gauss-Seidel method. We provide an initial estimate for $\mathcal{S}$ at iteration zero and the code then modifies this by relaxing the solution using the chosen profiles of $v_r(r, \theta)$, $v_\theta(r, \theta)$ and $\eta(r, \theta)$.

The magnitude of the central dipole field and the accretion rate do not enter this equation directly, but they are used to calculate the inner edge of the disc r_in. We recall that we have a radial numerical domain going from r_in to r_out, and a physical domain of interest which begins at the same radius but stops earlier, at the light cylinder radius r_lc. Along the θ direction the two domains coincide and go from θ_top, which is the top surface of the corona, to θ_eq, which is the equatorial plane (because of the symmetry of the system with respect to the equatorial plane, the solution below the equator will be the same as above it).

For the mass and radius of the neutron star, we use the canonical values, $1.4\,M_\odot$ and 10 km respectively. We fix the accretion rate as $\dot{m} = 0.03$ (in units of $\dot{M}_\mathrm{Edd}$), giving a magnetospheric radius of about $10\,r_\mathrm{g}$ when $B_0 \sim 3\,10^8$ G, as typical for a millisecond pulsar.

4.4.3 Testing of the code

In this subsection we describe some of the tests that we have performed with the code, before applying it to the cases of physical interest. These tests are needed in order to check the code for stability and convergence, to estimate errors and to optimize the iteration procedure by choosing an appropriate iteration step.

During this test phase we used the following values for the parameters:

- magnetic field at the stellar surface: $B_0 = 3\,10^8$ G;
- size of the domain: $r_\mathrm{in} = 10\,r_\mathrm{g}$, $r_\mathrm{out} = 750\,r_\mathrm{g}$, $\theta_\mathrm{top} = 80°$, $\theta_\mathrm{eq} = 90°$ and $\theta_\mathrm{c} = 82°$;
- radial inward velocity at inner edge: $v_r(r_\mathrm{in}) = v_0 = 10^5$ cm s^{-1}, which is the value obtained from equation (4.11) when $(\alpha, \dot{m})$ is equal to $(0.15, 0.03)$ or to $(0.1, 0.07)$;

- diffusivity: $r_{\eta\,\mathrm{in}} = r_{\mathrm{in}}$, $r_{\eta\,\mathrm{out}} = r_{\mathrm{out}}$, $\eta_0 = 10^{10}$ cm^2 s^{-1} and $\eta_{\mathrm{c}} = 10^{12}$ cm^2 s^{-1};
- initial estimate for the magnetic stream function: $\mathcal{S} = r_0 \cdot \sin\theta / r^{0.5}$ (for a dipolar field $\mathcal{S}^{\mathrm{dip}} = r_0\, \sin^2\theta / r$);
- iteration step: $\Delta t = 3\,10^{-2} \cdot \Delta x \cdot \Delta y$.

The tests can be divided into two main groups: with and without a known analytic solution. For the latter, we can estimate errors by calculating the residuals and by comparing the solutions obtained with different grid resolutions, while for the former we also have the analytic error.

Test with an analytic solution

There are two cases for which we can obtain an analytic solution. The first has dipolar boundary conditions and no poloidal motion ($v_r = v_\theta = 0$); in this case the poloidal component of the field must be dipolar everywhere (we refer to this test as D, for dipolar). In the previous section we showed that, in order to have a dipolar field as a stationary solution of the induction equation, the poloidal velocity has to fulfill the relation given by equation (4.21) and using $v_r = v_\theta = 0$ is consistent with that condition. Our second analytic test case has the boundary conditions for $\mathcal{S}$ set to zero. In this case, regardless of the profile used for the velocity, $\mathcal{S}(r,\theta) = 0$ is a solution in all of the domain (we call this test Z, for zero). Even if at first glance a test with an identically zero solution may seem to be of little importance, we think that it is useful, because in this way we can test the code by including all of the terms that will be present when solving for the cases of interest (i.e. including v_r, v_θ and η).

In both cases, we test two different configurations by changing the velocity profile. In test D we consider a case with zero velocity (test D1) and another one where v_θ is given by equation (4.21) and v_r is given by equation (4.11) in the corona and is zero in the disc (test D2). In test Z we consider the same velocity profile as the one that we will use for our cases of interest, given by equations (4.11) and (4.21) (test Z1), and a velocity profile which is the same as that used in test D2 (test Z2).

In all of these tests we follow the same procedure, we verify the stability of the code, we estimate the error and see if it scales correctly, checking the convergence of the solution. We do this by studying how the numerical solution changes when varying the number of grid points (N_i and N_j) and the number of iterations.

We use five grids in total. When testing the dependence on N_j we use: 200×20, 200×40 and 200×80; while when testing the dependence on N_i we use: 100×20, 200×20 and 400×20. For each of these grids we calculate: (i) the absolute difference and (ii) the relative difference, between the numerical solution and the analytic one at each point of the grid; and (iii) the root mean square (rms) of the numerical solution $\mathcal{S}$ at each iteration step. The results obtained are very similar for all of the five grids and for each of the four tests and can be summarized with the following four statements: (1) both the absolute error and the relative error have a maximum near to the inner edge r_{in} which

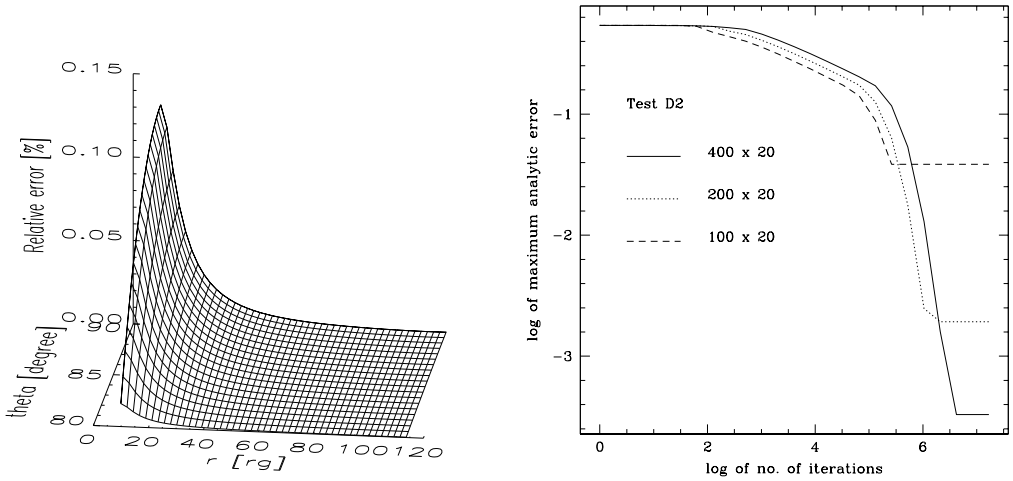

Figure 4.2: Both panels refer to the D2 test case. Left panel: relative error at each grid point of the region of interest with a 400×20 grid. For the other grids (and tests) the results have exactly the same qualitative behaviour, but the precise value of the error is different and increases when the number of grid-points decreases. For the 100×20 grid, the maximum relative error is ~ 15 per cent, while for the 200×20 grid it is about 0.8 per cent and finally for the 400×20 grid (shown in figure) it is 0.15 per cent. Right panel: maximum analytic error for with three grids, which differ only in N_i. Increasing N_j from 20 to 80 produces a very small decrease in the error (~ 7 per cent).

then decreases quite rapidly. With the 400×20 grid, the maximum relative error is about 0.1 per cent (see figure4.2 left panel); (2) changing N_j does not produce any visible effect: while increasing N_j by a factor of 4 (from 20 to 80) decreases the maximum relative error only slightly (by $\sim$ 7 per cent), changing N_i from 100 to 400 has a much greater effect, giving a decrease in the error of two orders of magnitude; (3) the reduction in the rms and of the maximum error becomes progressively smaller with increasing N_i, thus showing that we have convergence of the numerical solution; (4) using a sparser grid gives smaller errors at the beginning and during the relaxation process, however if one keeps iterating until the saturation level is reached, then the error with sparser grids is larger than with denser grids (suggesting that this problem could be suited for a multigrid approach). Regarding statements (2), (3) and (4), see figure 4.2 right panel.

Test with an unknown solution

We use now a configuration with dipolar boundary conditions and a velocity field given by equations (4.11) and (4.21). This is very similar to test D2, but in this configuration v_r

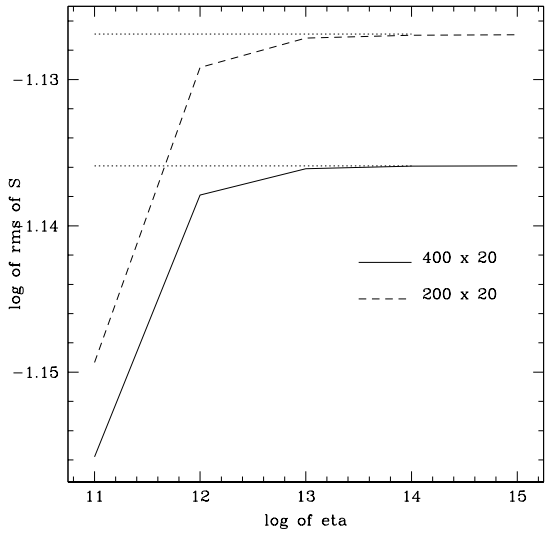

Figure 4.3: The rms of the numerical solution for different values of η after 2^{24} iterations. When $\eta \to \infty$, the rms should reach the value for a dipole, which is plotted with a dotted line for both grids.

is not taken to be zero in the disc. Even if we do not know the solution for this setup, we know from equation (4.10) that it has to approach a dipolar field when the coefficients $\frac{v_\theta}{r\,\eta}$ and $\frac{v_r}{r\,\eta}$ both go to zero. In order to test this we have considered five configurations, each with a different value of η_0 ranging between 10^{11} and 10^{15} cm^2 s^{-1} (η_c is always taken to be two orders of magnitude larger than η_0). Figure 4.3 shows clearly that for increasing η, the rms of the numerical solution is approaching that for a dipole calculated on the same grid.

For these five configurations we also performed the tests previously described, i.e. the ones regarding changing the grid and comparing the errors and the rms. The results are again similar and confirm the four statements made earlier.

Other tests

We next use the configuration of test D2 for checking three more aspects: determining the importance of the initial estimate for $\mathcal{S}$ and investigating which values to choose for the location of the outer radial boundary and for the iteration step.

The kind of algorithm which we are using to solve equation (4.10) needs an initial estimate for the solution. According to how good or bad this estimate is with respect to the correct solution, one needs a smaller or greater number of iterations for completing the process. In order to show this and also to demonstrate that the final solution does not depend on the initial profile, we used four initial estimates for the magnetic stream

function $\mathcal{S}$: (1) a constant value, (2) a Gaussian profile (centred on $r = 100\,r_{\rm g}$ and with a width of $20\,r_{\rm g}$), (3) a profile increasing with r^3 (this gives B_r and B_θ increasing linearly with r) and (4) the profile which gives a dipolar magnetic field (the analytic solution for this configuration is $\mathcal{S} = r_0 \cdot \sin\theta / r^{0.5}$). In all of the cases the final solution is the same, even for configuration (3), but the number of iterations required to reach it changes and goes from 0 for case (4) to 2^{20} for cases (1) and (2) and to 2^{26} for case (3).

As we mentioned previously (in Sections 4.2 and 4.4.2), our region of physical interest goes from the inner edge of the disc $r_{\rm in}$ out to the light cylinder $r_{\rm lc}$. Since we do not want the solution in this region to be influenced by the outer boundary condition, we ran some tests using different values for the radius of the outer edge $r_{\rm out}$ and then compared the numerical solutions in the region of interest. We used the same setup that we wanted to consider for our physical analysis, i.e. with dipolar boundary conditions, the velocity field given by equations (4.11) and (4.21) and the diffusivity given by equation (4.16). We used six values of $r_{\rm out}$ ($150\,r_{\rm g}$, $200\,r_{\rm g}$, $250\,r_{\rm g}$, $300\,r_{\rm g}$, $500\,r_{\rm g}$ and $750\,r_{\rm g}$) and we found that the difference within the region of interest between the numerical solutions obtained using two subsequent values of $r_{\rm out}$ became progressively smaller, until one could barely distinguish the different solutions. We decided to put the outer boundary at $750\,r_{\rm g}$ for the physical analysis; this gives results differing from those with $r_{\rm out} = 500\,r_{\rm g}$ by less than about 5 per cent.

Finally we considered varying the iteration step size, i.e. the Δt in equation (4.29), that is written as $c \cdot \Delta r \cdot \Delta\theta$. There is no simple argument of principle that can be used to determine the best value for c, therefore we determined it experimentally. We considered the same configuration as in test D2 and ran it several times varying only the value of c, going from 0.025 upwards. We found that the final error was the same, but that the number of iterations required to relax to the final solution was changing, decreasing as c increased. However there is an upper limit: when $c > c_{\rm max} = 1.25$ the solution diverges. Transferring this condition to Δt, we obtain $\Delta t_{\rm Max} = 8.5\,10^{-3}$. We can then change the way in which the iteration step size is calculated in the code and write: $\Delta t = n \cdot \Delta t_{\rm Max}$, with n always smaller than 1. We find that using the value $n = 0.95$ is a good compromise in minimizing the number of iterations and preserving the code stability.

All of the results presented in the next Section have been obtained using a 1000×20 grid and with $2^{24} \sim 1.7 \cdot 10^7$ total iterations, which were always enough to get residuals of the order of, or less than, 10^{-14}.

4.5 Results

From equation (4.25), we see that in order to calculate the stream function $\mathcal{S}$, and hence the poloidal magnetic field, we have to specify the following three functions: $v_r(r,\theta)$, $v_\theta(r,\theta)$ and $\eta(r,\theta)$. For the vertical velocity we follow the prescription given by equation (4.21), therefore we are left with needing to specify the other two functions. The profiles that we use for them have been described previously (see equation (4.11) for v_r and Sec-

tion 4.2 for η). Here we describe how the magnetic field configuration depends on these two functions.

In figures 4.4 and 4.5 we show the magnetic field lines calculated with four values of v_0, i.e. with different accretion rates[10]. For facilitating the comparison we show also a dipolar magnetic field (dashed). The field lines are labelled with the radial coordinate where the dipolar field imposed at the top boundary would cross the equatorial plane if not distorted. In this way the amount of distortion can be seen just by comparing the label of a given field line and the radius where it, in fact, reaches the equatorial plane. We can see that if v_r were zero, the field would not be distorted at all from the dipolar configuration and increasing the velocity then creates progressively more distortion. In the inner part of the disc, where the field is strongest, it is most able to resist distortion; further out, the field is weaker and it becomes progressively more distorted. For example, if one focusses on line 45, one can see that when $v_0 = 10^4$ this line crosses the equatorial plane at $r = 40\, r_{\rm g}$: we then say that this line has a distortion on the equatorial plane of $5\, r_{\rm g}$; when $v_0 = 10^5$, the distortion is $17\, r_{\rm g}$; and when $v_0 = 10^6$, it is about $20.5\, r_{\rm g}$. The degree of distortion depends on the location in the disc; from the figure we can see that it increases with distance. For example if one considers only the configuration with $v_0 = 10^4$, then one sees that the distortion on the equatorial plane at $r = 15\, r_{\rm g}$ is roughly zero, at $r = 25\, r_{\rm g}$ it is slightly larger than $1\, r_{\rm g}$ and at $r = 45\, r_{\rm g}$ it is about $5\, r_{\rm g}$.

According to the behaviour of the magnetic field lines, we can divide the disc into three regions: (1) an inner region, where the lines are not distorted very much away from the dipole; (2) a main region, where the distortion is very large and (3) the region in-between the two, which we call a transition region, where there is an accumulation of field lines. This means that in the transition region there is a magnification of the magnetic field (see figure 4.6).

In addition to varying the radial velocity, we also consider the role of the diffusivity. The results show that when we change η_0, we get the opposite behaviour to that seen when varying the velocity, i.e. a larger η_0 gives a smaller distortion. Moreover, when we use $v_0 = 10^5$ cm s^{-1} and $\eta_0 = 10^{11}$ cm^2 s^{-1} we obtain exactly the same result as when we use $v_0 = 10^4$ cm s^{-1} and $\eta_0 = 10^{10}$ cm^2 s^{-1} (the differences are of the order of 10^{-14}). Similarly using $v_0 = 10^6$ cm s^{-1} and $\eta_0 = 10^{11}$ cm^2 s^{-1} gives the same result as using $v_0 = 10^5$ cm s^{-1} and $\eta_0 = 10^{10}$ cm^2 s^{-1}, and $v_0 = 10^7$ cm s^{-1} and $\eta_0 = 10^{11}$ cm^2 s^{-1} gives the same as $v_0 = 10^6$ cm s^{-1} and $\eta_0 = 10^{10}$ cm^2 s^{-1}. This is telling us that what really matters is not the velocity or the diffusivity alone but their ratio. This is not surprising since in the equation which we are solving (equation (4.25)) the quantities only appear in this ratio (bearing in mind that v_θ is taken to be either zero or proportional to v_r). In fact, in Section 2.2 we have already seen that there is an important dimensionless number, the magnetic Reynolds number $R_{\rm m}$, which describes the general solution of the induction equation (4.2) and which is built from them. This is defined as: $R_{\rm m} \equiv l_0 \cdot v_0/\eta_0$, where l_0, v_0 and η_0 are respectively a characteristic length, velocity and diffusivity. Here we recall that this

[10] According to the solution for the Shakura-Sunyaev model, for fixed mass of the central object and viscosity α, the radial velocity is proportional to $\dot{m}^{2/5}$.

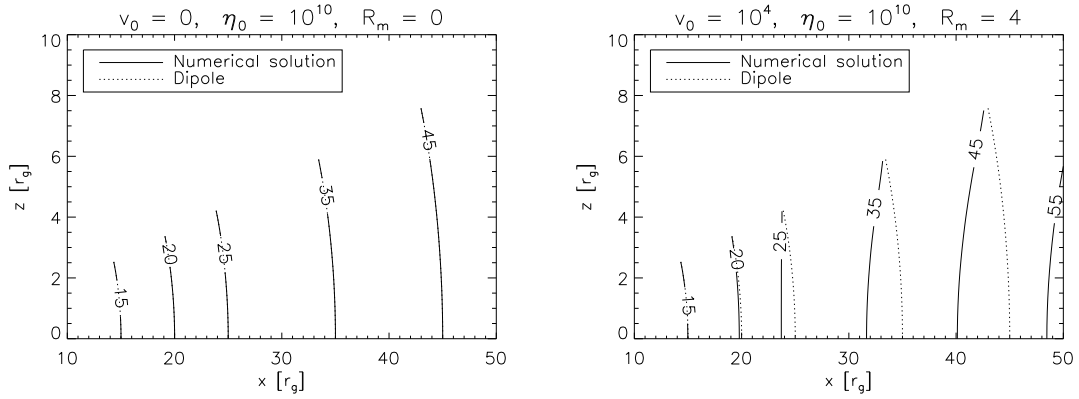

Figure 4.4: Magnetic field lines from the numerical solution (solid lines) and those for a dipole (dotted lines) for comparison. The left panel refers to a case with no accretion, where the field remains exactly dipolar, while in the right panel $v_0 = 10^4$ cm s^{-1}, and the field is distorted. The diffusivity η_0 has the same value in both panels (10^{10} cm^2 s^{-1}). If we use $\eta_0 = 10^{11}$ cm^2 s^{-1} and $v_0 = 10^5$ cm s^{-1}, we obtain the same result as shown in the right panel ($R_{\rm m} = 4$ for both).

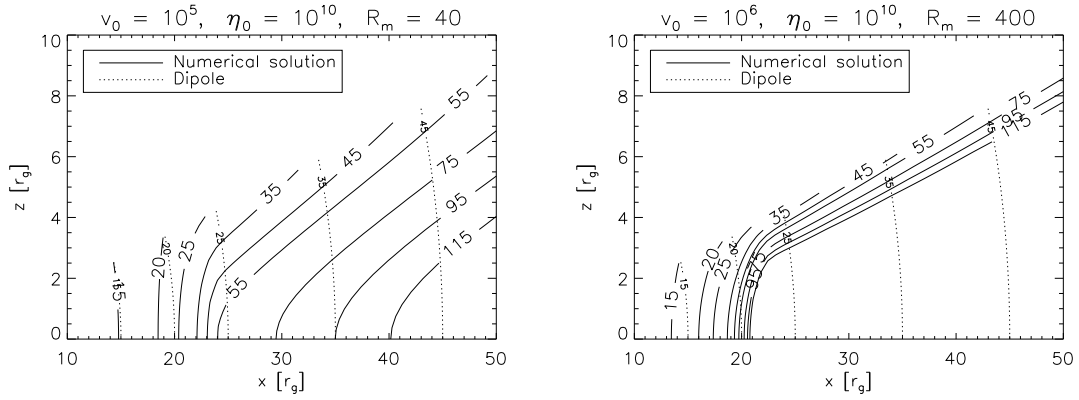

Figure 4.5: The same as in figure 4.4, but with different values of v_0. The left panel is for a case with $v_0 = 10^5$ cm s^{-1} while the right one is for $v_0 = 10^6$ cm s^{-1}. If we use $\eta_0 = 10^9$ cm^2 s^{-1} and $v_0 = 10^5$ cm s^{-1}, we obtain the same as in the right panel ($R_{\rm m} = 400$ for both).

parameter gives the relative importance of the two terms on the right-hand side of the induction equation. For large $R_{\rm m}$, we are in the regime of ideal MHD with the magnetic field and plasma being frozen together, for low $R_{\rm m}$, instead, the field and plasma are almost decoupled and the field simply diffuses[11]. The value of $R_{\rm m}$ reported in figures 4.4 and 4.5 is calculated taking the characteristic velocity to be the radial velocity, since $v_\theta = 0$ in the disc and proportional to v_r in the corona, while v_ϕ does not appear in the equation that we are solving now. The panels in these figures are clearly showing that the distortion of the field is proportional to the magnetic Reynolds number calculated in this way. This happens because with increasing $R_{\rm m}$ the freezing condition gets progressively stronger so that any fluid motion perpendicular to the magnetic field lines encounters more and more resistance. Therefore, since the velocity field is fixed, the magnetic field has to change. Figures 4.4 and 4.5 not only show that modifications in the magnetic field lines increase with $R_{\rm m}$, but also that their shape is consistent with that expected from considering the flux freezing condition in the case of a conical flow (which is what we have in the disc).

However the actual value of the magnetic Reynolds number is somewhat arbitrary, because in general there is no unambiguous way of defining the characteristic length, velocity and diffusivity of a given system. In our case we choose l_0 to be the radius of the inner edge of the disc, v_0 to be the radial velocity at the inner edge of the disc and η_0 to be the value of the diffusivity in the main disc region. We then obtain the values 0, 4, 40 and 400 for the panels of figures 4.4 and 4.5. One could also make a different choice for the characteristic length l_0, such as taking this to be the radius of the star or the average height of the disc; the trend of having larger distortions for larger values of $R_{\rm m}$ would of course be seen in all cases, but the switching on of the distortions would occur at different threshold values of $R_{\rm m}$.

We have already noted that the distortion varies with position, and so it is clear that a single global parameter cannot give a sufficiently detailed description in all parts of the system. It is therefore convenient to introduce a new quantity which we call the "magnetic distortion function" $D_{\rm m}$. We define this in the same way as the magnetic Reynolds number but, instead of taking characteristic values for the velocity and diffusivity, instead take the local values:

$$D_{\rm m}(r,\theta) = \frac{l_0 \cdot |\mathbf{v}(r,\theta)|}{\eta(r,\theta)} \tag{4.30}$$

This function gives the relative importance of the two terms on the right-hand side of the induction equation at every point of the disc, rather than giving just a global measure as with the standard magnetic Reynolds number. We then expect the advection term ($\nabla \times (\mathbf{v} \times \mathbf{B})$) to dominate in the regions where $D_{\rm m} > 1$ and the diffusion term ($\nabla \times (\eta \nabla \times \mathbf{B})$) to dominate when $D_{\rm m} < 1$. This then explains why we find three regions inside the disc: the inner region corresponds to the zone where $D_{\rm m} \ll 1$, the main region to $D_{\rm m} \gg 1$, and the transition region to intermediate values of $D_{\rm m}$. This correspondence is made clear in

[11] This does not mean that the field disappears, this is the case only when one uses zero field boundary conditions.

figure 4.6, where we show the θ component of the magnetic field, the dipolar profile and the magnetic distortion function. We recall that the jump in $D_{\rm m}$ follows from the profile chosen for η, i.e. we use a larger value of the diffusivity in the inner part of the disc, where we expect the density to be smaller, than in the main part of the disc.

Another important aspect of the magnetic distortion function is that the degree of arbitrariness in its definition is smaller than for the standard magnetic Reynolds number, since it is defined using only one characteristic value, l_0, while the actual profiles are used for the velocity and diffusivity[12]. In addition there is a quite natural way for choosing l_0. By looking at equation (4.25) one can see that, if $l_0 = r_{\rm g}$, the magnetic distortion function is already there in the equation (it is the coefficient of the partial derivative of $\mathcal{S}$ with respect to x). The value $r_{\rm g}$ is coming from the way in which we are scaling the lengths. If we had chosen a different unit for the lengths, say $\tilde{r}$, then we would have had to choose $l_0 = \tilde{r}$ if we wanted $D_{\rm m}$ to appear directly in equation (4.25). We can then think of l_0 as a quantity needed to make the ratio v/η dimensionless, and the most natural choice for this is the characteristic scale being used as the unit length.

Summarizing, we can describe the magnetic field configuration in the accretion disc by saying that magnetic field lines that enter the disc in the main region ($D_{\rm m} \gg 1$) are pushed towards the central object as soon as they enter the disc, whereas those which enter the disc in the inner region ($D_{\rm m} \ll 1$) are almost unmodified. The result is that in between these two regions there is an accumulation of field lines, and so there is a magnification of the magnetic field there, as can be seen in figure 4.6.

In order to understand better the influence of the magnetic distortion function on the magnetic field structure, we varied $D_{\rm m}$ and saw how the field changed. We used three new profiles for $D_{\rm m}$ different from the previous one which we then considered as a reference. In the first profile we increased the value of $D_{\rm m}$ in the inner part of the disc and left the rest unmodified, in the second one instead we lowered $D_{\rm m}$ in the main region of the disc and did not change the inner part, and in the last one we just changed the width of the transition between the low and high values of $D_{\rm m}$. We then calculated the poloidal magnetic field and the results are presented in figure 4.7, where the left panel shows the different profiles of the magnetic distortion function and the bottom one shows the θ component of the magnetic field, referring to the equatorial plane in both cases.

Considering this figure, we can summarize the influence of the magnetic distortion function with four comments: (1) changing the value of $D_{\rm m}$ in the inner part by a factor of 5 leaves the magnetic field almost unchanged, (2) on the other hand, the magnetic field is very sensitive to the width of the transition in $D_{\rm m}$ and to its value in the main region, in particular (3) the position of the peak in B_θ is related to the width of the transition and (4) the deviations away from the dipolar field are mainly governed by the value of $D_{\rm m}$ in the main region. We can go further and consider the radial derivative of $D_{\rm m}$, which is shown in figure 4.8 for all of the profiles used. From this we can see that the position of the peak of B_θ is strongly connected with the position of the minimum in $\partial_r D_{\rm m}$, and that the maximum amount of magnetic distortion is related to the depth of the dip in the

[12]For the velocity we use $|\mathbf{v}| = |v_r|$, following the earlier discussion

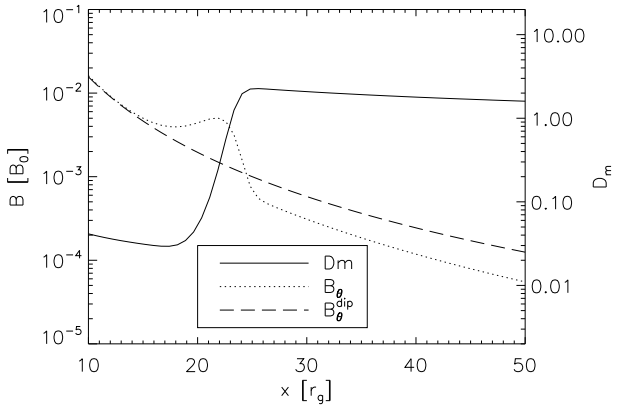

Figure 4.6: The Magnetic field B_θ as obtained from the numerical simulations for the configuration with $R_{\rm m} = 40$ (dotted) compared with those for a perfect dipolar field (dashed) at the equatorial plane. The solid line is the magnetic distortion function. The scale for $D_{\rm m}$ is shown on the right vertical axis. The magnetic field is measured in units of the stellar field, $B_0 = 3 \cdot 10^8$ G, as shown on the left vertical axis.

derivative of $D_{\rm m}$.

Finally we comment on the behaviour of the magnetic stream function in the equatorial plane. In order for the magnetic field to have a local minimum or maximum, its first radial derivative must, of course, be zero. This condition can be written in terms of $\mathcal{S}$ as:

$$\partial_r^2 \mathcal{S} - \frac{1}{r} \partial_r \mathcal{S} = 0 \tag{4.31}$$

For a dipolar field, $\mathcal{S} \propto 1/r$ which is a decreasing function of r with positive concavity (for positive r). In our case, we see that in the numerical simulations $\mathcal{S}$ is always decreasing, also when B_θ increases. Therefore the only way to get a local minimum or maximum is for $\mathcal{S}$ to go through a region where its concavity is reversed and becomes negative. An example of this is shown in figure 4.9, where we plot the stream function for the reference case. We can see that for $r < 16\, r_{\rm g}$ and $r > 22.5\, r_{\rm g}$ $\mathcal{S}$ has a positive concavity, while between these two values it is negative. The dotted lines in the figure delimit the regions of positive and negative concavity, while the open circles are drawn at the locations where B_θ has a minimum or a maximum. As expected these points are in the region of negative concavity.

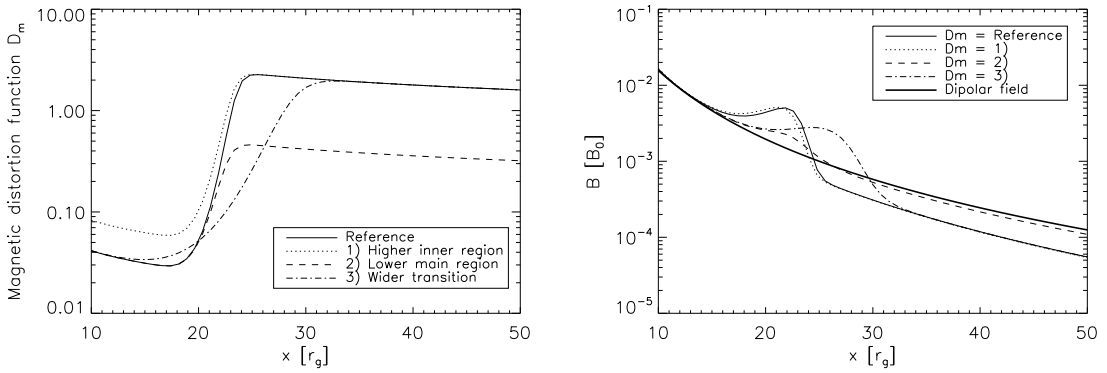

Figure 4.7: Left panel: magnetic distortion function in the equatorial plane. Right panel: θ component of the magnetic field in the equatorial plane. For both panels: the solid line shows results from the previous analysis (in the right panel the dipolar field is shown with a thick solid line); the dotted lines refer to profile 1 (larger value of $D_{\rm m}$ in the inner region only); the dashed lines refer to profile 2 (lower value of $D_{\rm m}$ in the main region only); the dot-dashed lines refer to profile 3 (same values of $D_{\rm m}$ in inner and main region, but the transition region is wider).

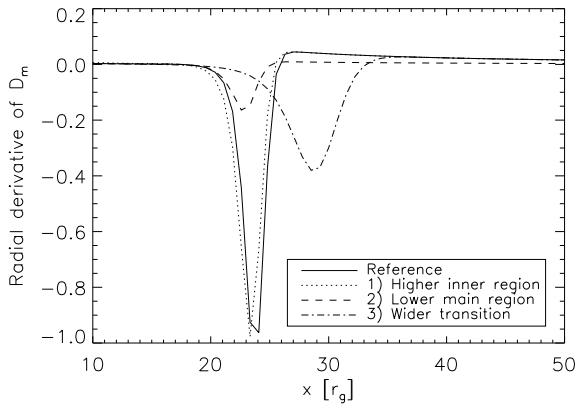

Figure 4.8: Radial derivative of the magnetic distortion function in the equatorial plane. The profiles refer to the same case as in figure 4.7. Comparing with the right panel of figure 4.7 one can see that the peaks in the magnetic field B_θ occur at almost the same locations as where $\partial_r D_{\rm m}$ has a minimum, and that the amplitudes of the distortions are proportional to the absolute values of the minimum of $\partial_r D_{\rm m}$.

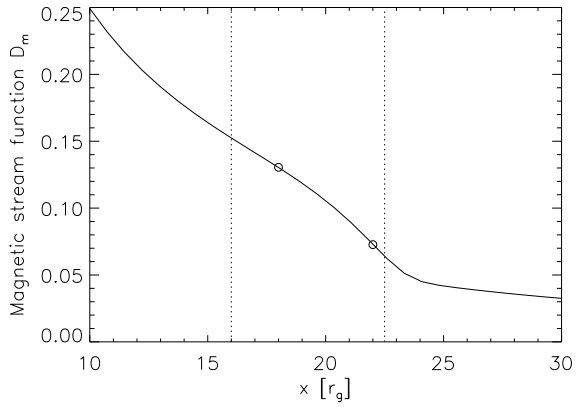

Figure 4.9: The magnetic stream function $\mathcal{S}$ for the reference profile. The dotted lines are drawn where $\mathcal{S}$ changes concavity, while the open circles mark the locations where B_θ has a minimum or a maximum, i.e. at $r \sim 18\, r_{\rm g}$ and $r \sim 22\, r_{\rm g}$; they are in the region where the concavity of the magnetic stream function is negative.

4.6 Conclusions

In this Chapter we have presented the beginning of a systematic study of the magnetic field configuration inside accretion discs around magnetised neutron stars. We have assumed that the star itself has a dipolar magnetic field, that it is rotating around its magnetic axis and that this axis is perpendicular to the disc plane. We have also assumed that the flow is steady and has axial symmetry everywhere. Our strategy was to start the analysis with a very simple model, where we made the kinematic approximation and solved the induction equation numerically in full 2D, without making any leading order expansion. This initial model will subsequently be improved by including the magnetic backreaction on the fluid flow.

We have shown that it is possible to separate the calculation for the configuration of the poloidal magnetic field from any azimuthal quantities. We have here considered only the poloidal component; the toroidal one will be addressed in a subsequent work. In particular, we have studied here how the magnetic field is influenced by the turbulent diffusivity and the velocity field, including discussion of an outflow starting at the top and bottom surfaces of the disc.

We have modelled the system as being composed of four regions (see figure 4.1): the central neutron star, the disc, the corona (taken to be a layer above and below the disc) and all of the rest is taken to be vacuum. We suppose that the stellar magnetic field remains dipolar until it reaches the corona. At that point it begins to feel the presence of the fluid flow and the magnetic field lines are pushed inwards, thus creating distortions

away from the purely dipolar field.

We have studied the response of the magnetic field to changes in the velocity and the diffusivity, finding distortions away from dipolar increasing with the radial infall velocity and decreasing with increasing diffusivity. The underlying behaviour is that the distortions increase together with the magnetic Reynolds number $R_{\rm m}$ (which governs the flux freezing condition) where the ratio v_0/η_0 appears.

However a single value of $R_{\rm m}$ cannot take into account any large changes in the magnitudes of the velocity and the diffusivity through the disc, since it is defined using single characteristic values. Therefore in order to have a sufficiently detailed description of the system, we have introduced a magnetic distortion function $D_{\rm m} = \frac{l_0 \cdot |\mathbf{v}(r,\theta)|}{\eta(r,\theta)}$, based on local values of the quantities concerned, so that in the regions where $D_{\rm m} \gg 1$ or $D_{\rm m} \ll 1$ one should expect to have large or small distortions respectively. We expect the turbulence to be enhanced in the regions of lower density (the corona and the inner part of the disc), therefore in our model we use a larger value of η in these regions, giving a smaller value for $D_{\rm m}$. As clearly shown in the panels of figures 4.4 and 4.5, the disc can be divided into three parts: (1) an inner region, where $D_{\rm m} \ll 1$ and the distortions are negligible; (2) a transition region, where $D_{\rm m}$ is rapidly increasing and magnetic field lines accumulate; (3) a main region, where $D_{\rm m} \gg 1$ and the the distortions are very large.

Comparing our results with previous literature, we can confirm the idea of dividing the disc into two principle regions: a narrow inner part, where the magnetic field is strongest, and a broad outer part, where the magnetic field is smaller and gently decaying. However the behaviour that we find for the field in these regions is very different from that of the Ghosh & Lamb model (1979 [14]) and we find it convenient to include a third zone, to be considered as a transition between the two principle ones (see figure 4.6). In the inner boundary layer of the GL model, the magnetic field is reduced by screening currents by a factor of 80 per cent, while in our case the field is barely modified in the first region, and then is amplified in the transition region. The behaviour in the outer zone is instead quite similar, and the field there is always smaller than the dipole one.

As regards the magnetic field geometry, our results resemble very much those obtained by Miller & Stone [22] (compare our figure 4.5 with their figure 2 top panel), despite the fact that they solved the full set of MHD equations whereas we have solved just the induction equation and with different boundary conditions.

The immediate next step will be that of calculating the toroidal magnetic field component, by solving equation (4.7), and consequently the magnetic torque. After that we will move to the next model, by releasing the kinematic approximation and solving the Euler equation as well as the induction equation. By comparing the results of that calculation with the ones presented here we will be able to understand the effects of the magnetic backreaction.

Bibliography

[1] Abbott B. et al., 2007, Phys.Rev.D, 76, 042001

[2] Agapitou V. & Papaloizou J.C.B. 2000, MNRAS, 317, 273

[3] Balbus S.A. & Hawley J.F. 1991, ApJ, 376, 214

[4] Bildsten L., Chakrabarty D., Chiu J. et al. 1997, ApJS, 113, 367

[5] Bonanno A. & Urpin V. 2006, Phys. Rev. E, 73, 066301

[6] Bonanno A. & Urpin V. 2007, ApJ, 376, 214

[7] Campbell C.G. 1987, MNRAS, 229, 405

[8] Campbell C.G. 1992, GApFD, 63, 179

[9] Chandrasekhar S. 1960, Proc. Natl. Acad. Sci., 46, 253

[10] Davidson K. & Ostriker J. P. 1973, ApJ, 179, 585

[11] Di Salvo T., Burderi L., Riggio A., Papitto A. & Menna M. T. 2007, preprint (astro-ph/0705.0464v2)

[12] Elstner D. & Rüdiger G. 2000, A&A, 358, 612

[13] Ghosh P., Lamb F.K. & Pethick C.J. 1977, ApJ, 217, 578

[14] Ghosh P. & Lamb F.K. 1979, ApJ, 232, 259

[15] Ghosh P. & Lamb F.K. 1979, ApJ, 234, 296

[16] Illarinov A. F. & Sunyaev R. A. 1975, Astr. Ap., 39, 185

[17] Kiziltan B. & Thorsett S.E. 2009, ApJ, 693, L109

[18] Kluzniak W. & Rappaport S. 2007, ApJ, 671, 1990

[19] Kueker M., Henning T. & Rüdiger G. 2003, ApJ, 589, 397

[20] Kulkarni A. K. & Romanova M. M. 2008, MNRAS, 386, 673

[21] Mestel L. 1961, MNRAS, 122, 473

[22] Miller K. A. & Stone J. M. 1997, 489, 890

[23] Rekowski M.v., Rüdiger G. & Elstner D. 2000, A&A, 353, 813

[24] Romanova M. M., Ustyugova G. V., Koldoba A. V. & Lovelace R. V. E. 2002, ApJ, 578, 420

[25] Rüdiger G., Hollerbach R., Schultz M. & Elstner D. 2007, MNRAS, 377, 1481

[26] Rüdiger G. & Shalibkov D. 2002, A&A, 393, L81

[27] Shakura N.I. 1975, Soviet Astr. Letters, 1, 223

[28] Shakura N.I. & Sunyaev R.A. 1973, A&A, 24, 337

[29] Shalibkov D. & Rüdiger G. 2000, MNRAS, 315, 762

[30] Tayler R.J. 1973, MNRAS, 161, 365

[31] Turner N.J. Sano T., 2008 ApJ, 679, L131

[32] Velikov E.P. 1959, Sov. Phys. JETP, 9, 995

[33] Wang Y.-M. 1987, A&A, 183, 257

Chapter 5

The ZEUS code

As we have mentioned in the General Introduction (Chapter 1) there are two working levels in this thesis. On the one hand there is the Physics level and on the other the Numerics one. Up to now we have mainly described the topics within the ambit of Physics, with the exception of two Sections (3.3 and 4.4) where we have described the numerical codes used to study the problem of the mean field dynamos in proto-neutron stars and the problem of the magnetic field configuration in accretion discs around magnetised neutron stars.

In Section 3.5 we have also mentioned that in order to continue our analysis of the dynamos in PNSs, we want to use a suitably modified version of the ZEUS-MP code. In this Chapter, we first describe the history of the code, outlining the developments made from the first version up to the current one, and then explain the new modifications which we have now made.

5.1 History

ZEUS is a family of codes for astrophysical fluid dynamics simulations developed at the Laboratory for Computational Astrophysics (LCA) of the National Center for Supercomputing Applications (NCSA) at the University of Illinois. ZEUS has its roots in a 2D Eulerian hydro code developed by M. Norman for simulations of rotating protostellar collapse (Norman, Wilson & Barton 1980 [15]) while he was a student at the Lawrence Livermore National Laboratory. The hydrodynamics algorithm, which has changed little in subsequent versions, is based on a simple staggered-grid finite-difference scheme (Norman 1980 [12]; Norman & Winkler 1986 [16]). Shock waves were captured within a few cells with a von Neumann-Richtmyer type of artificial viscosity. A powerful and essential feature of the code, which has been retained in subsequent versions, was that the equations for self-gravitating hydrodynamics were solved on a moving Eulerian grid permitting accurate simulation over a range of scales.

A significant improvement to the hydrodynamics algorithm came with the incorporation of the second order-accurate, monotonic advection scheme (van Leer 1977 [20]). This code version was vectorized for the Cray-1 supercomputer at the Max-Planck-Institut für Astrophysik in Munich, and extensively applied to the simulation of extragalactic radio jets (Norman et al. 1982 [14]).

The first code actually called ZEUS was developed by David Clarke as a part of his Ph.D. thesis on MHD simulations of radio jets (Clarke 1988 [2]; Clarke, Norman, & Burns 1986 [3]) under Norman's supervision. One of the principal challenges in numerical MHD simulations is satisfying the zero-divergence constraint on B. In axisymmetric simulations, this was ensured by evolving the toroidal component of the magnetic vector potential from which divergence-free poloidal field components can be derived, as well as evolving the toroidal magnetic field component directly. Third order-accurate monotonic advection was used for evolving A_ϕ in order to improve the quality of the derived current densities.

The next development was a major rewrite and significant extension of ZEUS by James Stone as a part of his Ph.D. thesis at the University of Illinois. The resulting code, named ZEUS-2D, solves the equations of self-gravitating radiation magnetohydrodynamics in two or 2.5 dimensions (2.5D denotes a problem computed in 2 spatial dimensions involving the 3-component of a vector quantity, such as velocity, that is invariant along the third axis but variable along the 1- and 2-axes). Many new algorithms were developed and incorporated into ZEUS-2D including: (1) a covariant formulation, allowing simulations in various coordinate geometries; (2) a tensor artificial viscosity; (3) a new, more accurate MHD algorithm (MOC-CT) combining the Constrained Transport algorithm (Evans & Hawley 1988 [4]) with a Method Of Characteristics treatment for Alfven waves; and (4) a variable tensor Eddington factor solution for the equations of radiation hydrodynamics. ZEUS-2D's algorithms and tests are described in detail in an often-cited series of three papers (Stone & Norman 1992a [18]; Stone & Norman 1992b [19]; Stone, Mihalas & Norman 1992 [17]).

The MOC-CT algorithm for numerical MHD was specifically designed to be extendable to 3D, and work on a 3D version of ZEUS began in 1989 when David Clarke went to Illinois as Norman's postdoc. Written for the Cray-2 supercomputer, ZEUS-3D physics options included hydrodynamics, MHD, self-gravity, and optically thin radiative cooling. This version of the code was the first of the ZEUS family with parallel capability, accomplished using Cray Autotasking compiler directives. Novel features of the code included the use of a custom source code pre-processor which handled a variety of source code transformations. Another useful feature of ZEUS-3D was an extensive set of inline graphics and diagnostic routines, as well as the ability to run in 1D and 2D modes. The ZEUS-3D MHD module differed from that used in ZEUS-2D with regard to both dimensionality and method: the MOC treatment of Alfven waves was modified to incorporate the improvements introduced by John Hawley and James Stone (Hawley & Stone 1995 [7]) for enhanced stability in weakly magnetized, strongly sheared flows. This modified HS-MOC-CT method is the basis for the MHD module adopted in ZEUS-MP.

Work was begun on ZEUS-MP in the fall of 1996 by Robert Fiedler and subsequently

by John Hayes and James Bordner with support from the US Department of Energy to explore algorithms for parallel radiation hydrodynamics simulations in 3D.

5.2 Zeus-MP

ZEUS-MP is a portable, parallel rewrite of ZEUS-3D. MP stands for: Multi Physics, Massively Parallel, and Message -Passing. 3D simulations are by their nature memory– and compute– intensive. The most powerful computers available today are parallel computers with hundreds to thousands of processors connected into a cluster. While some systems offer a shared memory view to the applications programmer, others, such as Beowulf clusters, do not. Thus, for the sake of portability, developers have assumed "shared nothing" and implemented ZEUS-MP as a SPMD (Single Program, Multiple Data) parallel code using the MPI message-passing library to effect interprocessor communication.

The first public release of ZEUS-MP included HD, MHD and self-gravity, but was written exclusively for 3D simulations. The new version of the code[1], which is the one we are using here, offers a substantially extended menu of physics, algorithm and dimensionality options. There are four main physics modules: HD, MHD, radiation transport, and self-gravity, and they accommodate solutions in 1, 1.5, 2, 2.5 and 3 dimensions. The hydro and MHD modules are time-explicit, and thus require no linear algebra libraries for their solution. The hydro algorithm is a straightforward 3D extension of the algorithm described in (Stone & Norman 1992a [18]). The MHD algorithm is the HSMOC-CT algorithm as mentioned in the previous section. Arbitrary equations of state are supported, though only gamma-law and isothermal equations of state are provided. The radiation transport implements a time-implicit flux-limited diffusion algorithm developed by Stone. The radiation and gas energy equations are solved as a coupled, implicit system, resulting in a large, sparse, banded system of linear equations which must be solved within an outer nonlinear Newton iteration. Two linear system solvers are built into ZEUS-MP: a conjugate gradient solver (CG/BiCG) with diagonal preconditioning, and a multigrid solver (MGMPI). Self-gravity is included in several ways: spherical gravity is adopted for one-dimensional problems and can be used also in two dimensions; two parallel Poisson solvers are included for problems with Neumann and Dirichlet boundary conditions; and a fast Fourier Transform package is provided for problems with triply-periodic boundaries. In addition to self-gravity, a simple point-mass external potential may be imposed in spherical geometry.

As in earlier versions of ZEUS, the equations solved by ZEUS-MP are formulated on a covariant, moving Eulerian grid. Problems in Cartesian, cylindrical, and spherical polar coordinates can be run with a variety of boundary conditions and types (periodic, Dirichlet, Neumann). The linear system solvers are designed to handle all cases.

ZEUS-MP utilizes domain decomposition for parallelization, wherein the computational domain is subdivided into a number of equally-sized regions, each of which is assigned to a different processor for execution. Depending on the problem size and

[1] ZEUS-MP2 can be downloaded from http://lca.ucsd.edu/portal/software/zeus-mp2.

the number of processors targeted, the user can specify a 1D "slab", 2D "pencil", or 3D "block" decomposition. A region is represented in processor memory as arrays of data storing the solution vector for a specific subdomain. The arrays are dimensioned so as to include two layers of buffer zones on each face of the block for the purpose of transferring boundary conditions from neighbouring processors. Data transfer between neighbouring blocks, as well as collective operations and global reductions are handled via MPI function calls.

5.3 Modification strategy

Our object here is to include in the induction equation solved by the ZEUS code both the resistivity term, $\eta\nabla\times\mathbf{B}$, and the $\alpha\mathbf{B}$ term, i.e. we want to use ZEUS for solving the mean field induction equation:

$$\partial_t\overline{\mathbf{B}} = \nabla\times\left(\overline{\mathbf{v}}\times\overline{\mathbf{B}} + \alpha\overline{\mathbf{B}} - \eta\nabla\times\overline{\mathbf{B}}\right) \tag{5.1}$$

where barred vectors are used to indicate that we are considering only the mean components. If one groups all of the terms inside the parentheses on the right hand side as an electromagnetic force $\mathcal{E}$ (EMF)[2], then this equation has the same form as in ideal MHD, the difference being in the expression for the EMF. In fact for the ideal MHD induction equation:

$$\mathcal{E} = \mathbf{v}\times\mathbf{B} \tag{5.2}$$

while for the mean field case:

$$\mathcal{E} = \overline{\mathbf{v}}\times\overline{\mathbf{B}} + \alpha\overline{\mathbf{B}} - \eta\nabla\times\overline{\mathbf{B}} \tag{5.3}$$

Our strategy is to modify the way in which ZEUS calculates the EMFs, which are fundamental quantities in this code. As mentioned in the previous Section, the magnetic field is calculated using the CT alogorithm, which guarantees that any initial divergence free magnetic field remains solenoidal at all times, provided that no magnetic monopoles are introduced through the boundaries. Therefore the magnetic field at the new time step is calculated using the magnetic flux. This is done in the `ct` subroutine. The magnetic flux is in turn calculated from the EMFs, which are obtained with the HS-MOC method in the `hsmoc` subroutine, therefore globally the magnetic field is updated in terms of the EMFs. Here is an extract of the code from the `ct` subroutine, where $\mathbf{B}_\phi$ is updated:

```
b3(i,j,k) = ( b3(i,j,k) * qty1(i) * dx2a(j)
            + dt * ( emf2(i+1,j  ,k) - emf2(i,j,k)
                   - emf1(i  ,j+1,k) + emf1(i,j,k) ) )
```

[2]We note here the rather incorrect use of the term "electromagnetic force". The quantity in parentheses is in fact an electric field and, in order to obtain the EMF, one should then integrate $\mathcal{E}$ over a closed circuit. However we follow this convention of calling $\mathcal{E}$ the electromagnetic force, because it is the standard approach used in the papers describing the ZEUS codes.

```
* qty1ni(i) * dx2ai
```

where the "qty" terms include some metric and differential factors. We have created a new subroutine (`current`) where we calculate the two additional terms to be included in the EMFs. This subroutine is called in `hsmoc` after that the $\overline{\mathbf{v}} \times \overline{\mathbf{B}}$ term has been calculated and the boundary conditions (BCs) have been called; afterwards the complete EMFs are computed.

Given that the BCs are not applied to the magnetic field directly, but instead to the EMFs, we have to modify them as well. In the original subroutine for setting the BCs (`bvalemf`), only the $\mathbf{v} \times \mathbf{B}$ part of the EMF is considered. We have decided to create a new subroutine (`jbvalemf`) which contains all of the original one plus the conditions for the additional terms. Whenever a call to the BCs is made we substitute the call to the original subroutine with a call to the new one.

In doing all of the modifications outlined here we have always taken great care to include the correct metric factors, in order to obtain a code that can be used also with other coordinate systems. So far we have performed tests only in spherical coordinates, but we plan to make tests also in oter coordinate system.

5.3.1 The two meshes

The ZEUS codes use a system of two staggered meshes, which we call the a-mesh and the b-mesh, and we refer to the points of the a-mesh as $x_{1\mathrm{a}}, x_{2\mathrm{a}}, x_{3\mathrm{a}}$ and to the points of the b-mesh as $x_{1\mathrm{b}}, x_{2\mathrm{b}}, x_{3\mathrm{b}}$.

One can first think of the entire discretised volume as being covered by just one grid, the a-grid. The mesh of grid lines defines a system of zones in between them and the centres of these zones are taken as the gridpoints of the b-grid. In this picture the positions of the zone boundaries in each direction are specified by the a-mesh, while zone centers are specified by the b-mesh. Consequently all along the boundaries of the entire domain there are only a-mesh points, this will obviously have consequences for the implementation of the boundary conditions (see Section 5.3.2). Grid spacing in each direction is arbitrary and independent and the coordiante mesh can be moved with respect to a stationary background using grid velocities, although we have never used this option.

Finite differencing the evolution equations near to the boundaries of the grid requires values for the dependent variables to be specified outside the computational domain and, at each boundary, we have two rows of "ghost zones". Values for the dependent variables in the ghost zones are specified using boundary conditions (see Section 5.3.2) appropriate for the physics of the problem being solved. The evolution equations are not solved for the ghost zones. The presence of two additional rows of zones at each boundary implies that the number of a- and b-mesh points is increased by 4 along each direction.

In general, scalars and the diagonal components of tensors of even rank are defined at zone centres, while the components of tensors of odd rank are defined at the appropriate zone interfaces. The off-diagonal components of tensors of even rank are defined at zone

corners and the magnetic field components are then defined as follows:

$$\mathbf{B_1} = \mathbf{B_1}(x_{1\mathrm{a}}, x_{2\mathrm{b}}, x_{3\mathrm{b}}) \tag{5.4}$$
$$\mathbf{B_2} = \mathbf{B_1}(x_{1\mathrm{b}}, x_{2\mathrm{a}}, x_{3\mathrm{b}}) \tag{5.5}$$
$$\mathbf{B_3} = \mathbf{B_1}(x_{1\mathrm{b}}, x_{2\mathrm{b}}, x_{3\mathrm{a}}) \tag{5.6}$$

Velocities are defined it the same points as the magnetic field, while the EMFs are the opposite of this (as for the vector potential):

$$\mathcal{E}_{\mathbf{1}} = \mathcal{E}_{\mathbf{1}}(x_{1\mathrm{b}}, x_{2\mathrm{a}}, x_{3\mathrm{a}}) \tag{5.7}$$
$$\mathcal{E}_{\mathbf{2}} = \mathcal{E}_{\mathbf{2}}(x_{1\mathrm{a}}, x_{2\mathrm{b}}, x_{3\mathrm{a}}) \tag{5.8}$$
$$\mathcal{E}_{\mathbf{3}} = \mathcal{E}_{\mathbf{3}}(x_{1\mathrm{a}}, x_{2\mathrm{a}}, x_{3\mathrm{b}}) \tag{5.9}$$

When one is taking a derivative along a certain direction for a quantity defined e.g. on the a-mesh, the result will be located on the b-mesh, along the same direction. Consider, for example, the first component of the magnetic field calculated using the vector potential in spherical coordinates:

$$B_r = \frac{1}{r^2 \sin\theta} \left[\partial_\theta \left(r \sin\theta A_\phi\right) - \partial_\phi \left(r A_\phi\right)\right] \tag{5.10}$$
$$= \left\{ \frac{\partial_\theta \left(\sin\theta A_\phi\right)}{r} - \frac{\partial_\phi \left(A_\phi\right)}{r} \right\} \frac{1}{\sin\theta} \tag{5.11}$$

If one considers the $\partial_\theta(\cdots A_\phi)$ term, then the quantity in the paretheses has to be defined on the a-mesh, so that the derivative is defined on the b-mesh, i.e. at the same place as B_r. Here we write the code instruction related to (5.11):

```
b1(i,j,k) = ( ( g32a(j+1)*A3(i,j+1,k) - g32a(j)*A3(i,j,k) )
              * dx2ai(j) * g2ai(i)
          -  (           A2(i,j,kp1) -         A2(i,j,k) )
              * dx3ai(k) * g31ai(i)   ) * g32bi(j)
```

where the g-terms account for the coordinate dependent coefficients which appear when one takes a derivative in a curvilinear coordinate system[3]. These terms are in fact all 1 for a Cartesian coordiante system, while in a spherical coordinate system, which is the one in which equation 5.11 is written, $g_2 = g_{31} = r$ and $g_{32} = \sin\theta$. These factors are related to the specific metric tensor used. Since we are interested only in orthogonal coordinate systems the metric tensor is diagonal:

$$m_{ij} = \begin{pmatrix} h_1^2 & 0 & 0 \\ 0 & h_2^2 & 0 \\ 0 & 0 & h_3^2 \end{pmatrix}$$

[3]In writing the code we followed the convection of adding an "i" at the end of variable name, to indicate the inverse of that quantity. Therefore for example g2ai is equal to $1/$g2a.

and the h are in general functions of the coordiantes, $h_i = h_i(x_1, x_2, x_3)$, however for Cartesian, cylindrical and spherical coordinate system, which are the ones we are intrested in, this dependence is very simplified, and the "g" factors are introduced:

$$h_1 = h_1(x_1) = g_1(x_1) \tag{5.12}$$
$$h_2 = h_2(x_1) = g_2(x_1) \tag{5.13}$$
$$h_3 = h_3(x_1, x_2) = g_{31}(x_1) \cdot g_{32}(x_2) \tag{5.14}$$

Here are the values for the three systems:

1. Carteisan coordiantes $(x_1, x_2, x_3) = (x, y, z)$
   in this case all of the "g" and "h" factors are 1;

2. Cylindrical coordiantes $(x_1, x_2, x_3) = (z, r, \phi)$
   $(h_1, h_2, h_3) = (1, 1, r)$, with $g_{31} = 1$;

3. Spherical coordiantes $(x_1, x_2, x_3) = (r, \theta, \phi)$
   $(h_1, h_2, h_3) = (1, r, r\sin\theta)$, where $g_2 = g_{31} = r$ and $g_{32} = \sin\theta$.

Calculating the full EMFs requires introducing quantities which are not present in the original ZEUS code: the coefficient of the α-effect and the magnetic diffusivty η. The former has to be defined in the same place as the magnetic field, while the second has to be placed at the same location as $\nabla \times \mathbf{B}$ (see the induction equation). The $\alpha\mathbf{B}$ term requires further manipulation, because being part of the EMF it has to be defined on the same mesh, while at the moment it is defined in the same place as the magnetic field is. For doing this we perform an average over neighbouring points.

5.3.2 Boundary conditions

As we have described in the previous Section, the computational domain used in ZEUS can be divided into two parts: the active zones, where the evolution equations are solved, and the ghost zones, where boundary conditions (BCs) are used. These BCs are explicit relations which give the values of the dependent variables in the ghost zones as a function of the values in the active zones of the grid. There are four types of BCs built into the ZEUS code:

1. Reflecting BC:
   Perfect conductor – The normal components of velocity and magnetic field are reflected, while the tangential components are taken to be continuous. This implies that the EMFs in the ghost zones are equal to the negative of the EMFs in the equivalent active zones;
   Pseudo vacuum – As for the perfect condutor but with reflection of the tangential components of the magntic field, instead of the normal component, which is instead continuous;

2. Inflow BC:
   The EMFs in the ghost zones are set to some predetermined value, which may be allowed to vary in time;

3. Outflow BC:
   The EMFs in each ghost zone are set equal to the EMF in the first active zone;

4. Periodic BC:
   The EMFs in the ghost zones are set equal to the EMFs in the corresponding active zones on the opposite side of the grid.

These BCs can be applied independentely for each ghost zone in the mesh. We do not need to introduce new BCs for our modified version, but we do have to implement the existing ones also for the additional terms that we have added into the EMFs. For the set-up which we are intrested in, the θ boundaries coincide with the axis, i.e. $\theta_{\rm in} = 0$ and $\theta_{\rm out} = \pi$; for the ϕ boundaries we use $\phi_{\rm in} = 0$ and $\phi_{\rm out} = 2\,\pi$, while for the radial direction we only require $r_{\rm in} \neq 0$ to avoid singularities at the centre of the coordinate system. For the axis we use the reflecting perfect conductor condition with inversion of the 3-component; for the ϕ boundaries we use, of course, periodic BCs; while for the radial boundaries we use both of the two reflecting conditions.

All of the BCs that we are interested in are implemented by using two different conditions: symmetric and antisymmetric. Here is an example of the symmetric condition for a quantity defined on the a-mesh (e.g. the θ component of the additional EMF at the inner radial boundary):

```
jalp(is  ,j,k) = jalp(is+1,j,k) * g2a(is+1)  * g2ai(is)
jalp(is-1,j,k) = jalp(is+1,j,k) * g2a(is+1)  * g2ai(is-1)
jalp(is-2,j,k) = jalp(is+2,j,k) * g2a(is+2)  * g2ai(is-2)
```

where the g-factors have to be included because the EMFs are multiplied by these factors (in `hsmoc`) before being used for updating the magnetic field (in `ct`). Here, instead, is an example of the antisymmetric condition for a quantity defined on the b-mesh (e.g. the r component of the additional EMF at the outer radial boundary):

```
jalp(ie+1,j,k) = - jalp(ie  ,j,k)
jalp(ie+2,j,k) = - jalp(ie-1,j,k)
```

In order to have working BCs on the axis, we set the angular velocity to be zero there; for the additional terms in the radial component of the EMF, we compute a ϕ average for the mesh-points which are exactly on the axis, while the other ghost zones are updated with a symmetric relation. At this point we should stress that because of the presence of the staggered meshes, not all of the quantities are defined on the axis. In fact only the a-mesh points lies on the axis, for the b-mesh instead the first active grid-point is the centre of the first zone and so is $0.5\,\Delta\theta$ away from the axis, where $\Delta\theta$ is the angular resolution in θ. For example $\mathcal{E}_1$ and $\mathcal{E}_3$ are defined on the axis, while $\mathcal{E}_2$ is not.

We now want to describe in some more detail the two reflecting BCs and we consider the case of the radial boundaries. For both of them the condition on the velocity is the same, i.e. the normal component is zero, while the other components are symmetric:

$$v_r = 0 \quad \text{and} \quad \partial_r v_\theta = \partial_r v_\phi = 0 \tag{5.15}$$

There is a difference, however, for the electromagnetic field:

- Perfect conductor – The perfect conductor boundary can be imagined as a conducting metal plate and so the tangential component of the electric field ($\mathcal{E}_\theta$, $\mathcal{E}_\phi$) and the normal component of the magnetic field (B_r) are required to vanish at the boundaries, while the normal component of the electric field is symmetric. Consequently, the tangential component of the magnetic field also has to be symmetric. Summarizing:

$$\partial_r \mathcal{E}_r = \mathcal{E}_\theta = \mathcal{E}_\phi = 0 \tag{5.16}$$
$$B_r = \partial_r B_\theta = \partial_r B_\phi = 0 \tag{5.17}$$

- Pseudo vacuum – In this case the normal component of the electric field ($\mathcal{E}_r$) and the tangential components of the magnetic field (B_θ, B_ϕ) all vanish, while the tangential components of the electric field are symmetric:

$$\mathcal{E}_r = \partial_r \mathcal{E}_\theta = \partial_r \mathcal{E}_\phi = 0 \tag{5.18}$$
$$\partial_r B_r = B_\theta = B_\phi = 0 \tag{5.19}$$

In order to conserve magnetic flux across a boundary, the Poynting vector normal to the boundary has to vanish. For example for the radial boundaries one has:

$$S_r = \mathcal{E} \times B|_r = \mathcal{E}_\theta B_\phi - \mathcal{E}_\phi B_\theta \tag{5.20}$$

This component is zero with both of the two BCs just described, with the difference that with the pseudo vacuum condition the normal magnetic field is allowed to extend outside the domain, while with the perfect conductor it is not.

5.3.3 Visualisation

For visualising the solutions we have mainly used the IDL routines develped by Detlef Elstner at AIP-Potsdam, Germany. With these tools we are able to visualise all of the magnetic field components in different ways. We can take a slice of the 3D domain by fixing one of the three coordinates and then making a surface plot with respect to the other two (see figure 5.1 for an example), or we can fix two of the three coordinates and then plot the magnetic field components with respect to the free one (see figure 5.2). The same can be done for the velocity components.

These plots can be produced at any timestep of the simulations and can also be seen in sequence as an animation. The frequency of the dumping of data during a simulation can be chosen from the input file, and therefore changes do not require recompilation of the code. We found it very useful to be able to make contour plots also of the toroidal magnetic field and we have therefore added this option to the routines, this is shown in figure 5.3 for the same field as that in the figures 5.1 and 5.2. Finally, we can also plot the energy of the system, including magnetic, kinetic and gravitational energy.

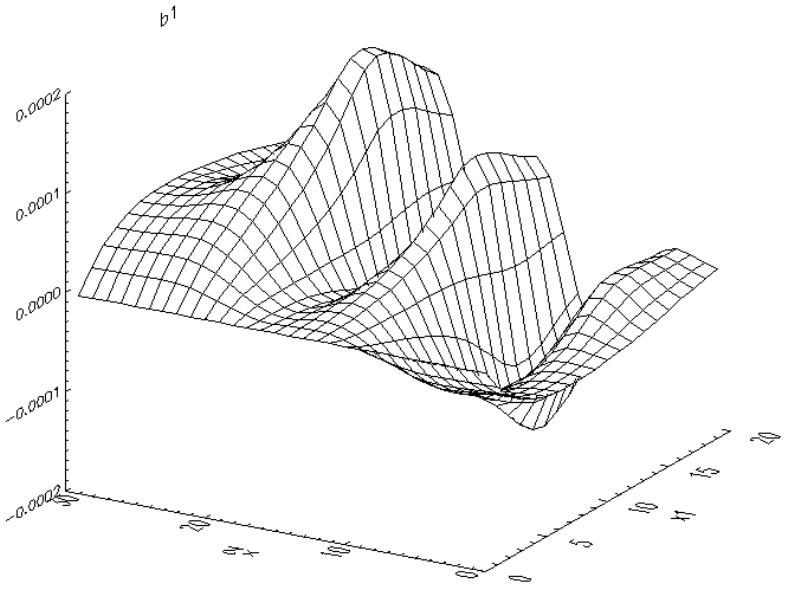

Figure 5.1: Surface plot of the magnetic field. In this case we are plotting the B_r component for a fixed value of ϕ with respect to r (x_1 in the figure) and θ (x_2 in the figure). Note that along the axes the number of grid point are shown.

5.4 Tests of the modified ZEUS-MP code

The first thing that we tested for with the modified vesion of the ZEUS-MP code was that the divergence of the magnetic field was really remaining zero at all times. By doing this we have assured that (1) the calculation of the initial magnetic field is correct (we calculate B by taking the curl of the vector potential) and that (2) the modifications to the boundary conditions are not introducing any magnetic monopoles.

All of the other main tests aimed at reproducing the results of some particular stellar dynamos. We started with the α^2 dynamo, putting the velocity field to zero. In this case we tried to obtain the critical value of the C_α dynamo number for symmetric and antisymmetric initial magnetic field configurations, and we compared our result with

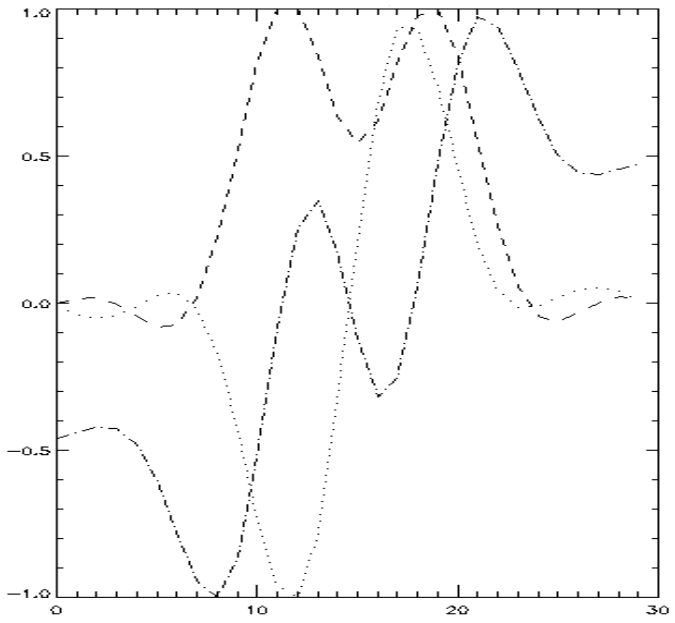

Figure 5.2: One dimensional plot of all of the magnetic field components (B_r is the dot-dashed line, B_θ the dashed line and B_ϕ the dotted one) with respect to θ for fixed value of r and ϕ. On the axis the gridpoint number along the θ direction is shown. The field is the same as the one shown in figure 5.1

those obtained with a pseudospectral eigenvalue code, the CTDYN (Catania Dynamo) code. This family of tests was performed in 3D, even if the problem has axial symmetry. As regards the BCs, we tested both of the two reflecting conditions. For the pseudo vacuum case we had to resort to a particular stratagem in order to impose the condition $B_\phi = 0$. We increased the computational domain to include also a shell beyond the surface of the star, and in this shell we put the α term to zero, and the diffusivity to a large value, usually between 10 and 100 times that inside the star. In this way we inhibited the dynamo action in the shell where instead the field decays. The overall results are very satisfying, not only because they differ from the reference ones by only about 2 per cent, but also because they showed that exciting the antisymmetric mode is easier than exciting the symmetric one, i.e. the critical C_α value for the A-mode is smaller than that for the S-mode.

After this we have introduced an angular valocity depending only on the spherical distance r: we took the profile used by Bonanno et al. 2003 [1]: $\Omega = \Omega_0 + \Omega_1 \cdot r^2$, and varied C_Ω in the range $[0,\, 10^3]$ in order to be in the regime of both the α^2 dynamo (when C_Ω is zero) and the $\alpha^2\Omega$ dynamo. In this case we mainly concentrated on the magnetic field evolution. For the $\alpha^2\Omega$ dynamo, we in fact expect to have an oscillating magnetic field because of the combined action of the α- and Ω-effect. This is indeed what we

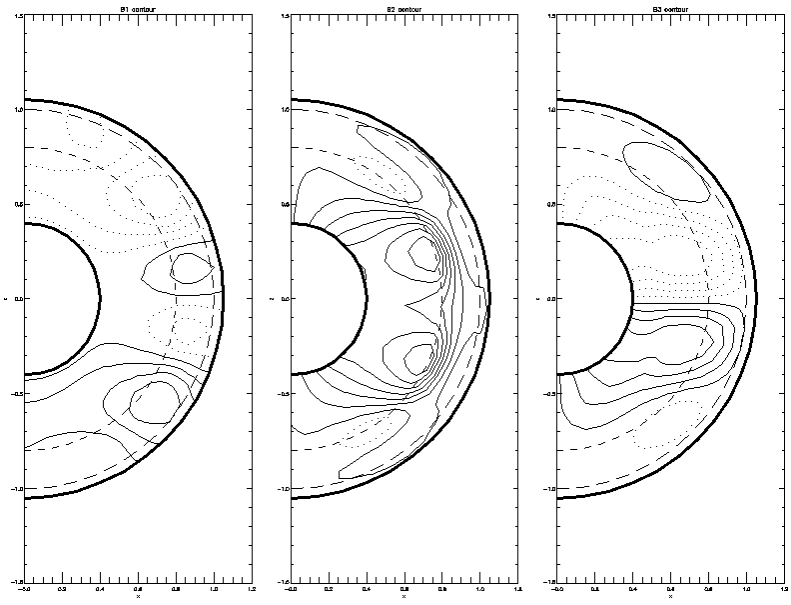

Figure 5.3: Contour plots of all of the three components of the magnetic field. Each panel refers to a different component: from left to right they are B_r, B_θ and B_ϕ. Dotted lines are used when the components become negative, i.e. pointing in the opposite direction of the versor relative to that component. The thick lines are the boundary of the numerical domain, the dashed lines represent internal structure of the model.

have obtained and we have also seen a migration of the magnetic field maximum from the poles to the equator, for negative Ω_1, and from the equator to the poles, for postive Ω_1. Finally we have considered the change in the critical C_α as a function of C_Ω and have obtained the same behaviour as that found by Bonanno et al., i.e. C_α has a local minimum for $C_\Omega \sim 50$ and then increases as C_Ω increases, reaches a maximum at about $C_\Omega \sim 150$ and then decreases again, the C_α curve being symmetric with respect to $C_\Omega \sim 50$.

We then tested a completely different setup, considering the solar dynamo studied in the benchmark work by Jouve et al. 2008 [1]. The parameter range in this case is such that the dynamo is of the $\alpha\Omega$ type, with C_Ω being as large as 10^5, moreover the rotational profile now depends also on the colatitude, as it should do for the Sun. We considered case A of Jouve et al., i.e. with constant η. In this case we compared the critical value of C_α and the frequency of the magnetic field oscillations. In the Jouve et al work these are 0.387 ± 0.002 and 158.1 ± 1.5 respectively. At this point it is worth describing the procedure which we follow to calculate the critical value of C_α. We fix a value of C_Ω, run a simulation with some initial value of C_α and then plot the magnetic energy. If we see that it is following an increasing trend, then we consider that particular value of C_α as overcritical, and redo the calculation with a smaller value. If instead the energy is

following a decreasing trend, then we consider that value of C_α as subcritical and redo the calculation with a larger value. Unfortunately as one gets progressively nearer to the critical value, it is necessary to make longer and longer simulations, to see whether the stationary state has been reached or not. All of this is done for each value of C_Ω. Our final results for these tests are that the critical C_α value is 0.375 ± 0.25, and for the frequency we obtain 155 ± 4, both of which are in agreement with the values obtained by Jouve et al. [1].

At this point we terminated the testing phase and started preparing the set-up to use for our first application of the modified version of the code, i.e. simulating the mean field dynamo in an axisymmetric model of proto-neutron stars.

Bibliography

[1] A. Bonanno, L. Rezzolla & V. Urpin 2003, A&A, 410, L33

[2] Clarke D. A. 1988, Ph.D. Thesis, Univ. New Mexico

[3] Clarke D. A., Norman M. L. & Burns J. O. 1986, ApJ, 311, L63

[4] Evans C. R. & Hawley J. F. 1988, ApJ, 332, 659

[5] Garca-Segura G., Langer N., Rozyczka M. & Franco J. 1999, ApJ, 517, 781

[6] Hayes J. C., Norman M. L., Fiedler R. A. et al. 2006, ApJS, 165, 188

[7] Hawley J. F. & Stone J. M. 1995, Comp. Phys. Comm., 89, 127

[8] Jouve L., Brun A.S., Arlt R. et al. 2008, A&A, 483, 949

[9] Low B. C. & Manchester W. 2000, ApJ, in press

[10] Mac Low M.-M. 1999, ApJ, 524, 169

[11] Mouschovias T. & Spitzer L. 1976, ApJ, 210, 326

[12] Norman M. L. 1980, Ph.D. Thesis, Univ. California, Davis, UCRL-52946

[13] Norman M. L. 2000, RevMexAA, 9, 66

[14] Norman M. L., Smarr L., Winkler K.-H. & Smith M. D. 1982, A&A, 113, 285

[15] Norman M. L., Wilson J. R., & Barton R. 1980, ApJ, 239, 968

[16] Norman M. L. & Winkler K.-H. 1986, in Astrophysical Radiation Hydrodynamics, ed. K.-H. Winkler & M. Norman (Dordrecht: Reidel), 187

[17] Stone J. M., Mihalas D. & Norman M. L. 1992, ApJS, 80, 819

[18] Stone J. M. & Norman M. L. 1992, ApJS, 80, 753

[19] Stone J. M. & Norman M. L. 1992, ApJS, 80, 791

[20] van Leer B. 1977, J. Comp. Phys., 23, 276

Chapter 6

Dynamos in axisymmetric proto-neutron stars

At the end of Chapter 3, Section 3.5, we have mentioned our strategy to use the publically available ZEUS code to improve our one dimensional model for studying mean field dynamos in proto-neutron stars (PNSs). However before applying the code to our case of interest we had to modify it, in order to include the α term and the resistivity term in the induction equation. The modification process has been described in the previous Chapter and now we use the modified version of the code to simulate the magnetic field evolution in the case of an axisymmetric PNS.

This analysis is still ongoing and in this Chapter we are mainly introducing the model, desribing our strategy and presenting some preliminary results.

6.1 The model

The Physics behind mean field dynamos in PNSs and our approach for studying them have already been described in Chapter 3, Sections 3.1 and 3.2. We are now modelling the PNS as being a sphere where the border between the regions of the two instabilities, i.e. the convective instability (CI) and the neutron finger instability (NFI), is a spherical surface placed at $r = R_{\rm inst}$. The CI zone is at $r < R_{\rm inst}$, while the NFI zone is at $r > R_{\rm inst}$.

As regards the velocity field, we suppose that the star is differentially rotating with an angular velocity that depends both on radius r and colatitude θ. We consider the profile introduced by Komatsu et al. in 1989 [2] and then used in many studies of PNSs (see e.g. Miralles et al. 2004 [3] and Villain et al. 2004 [5]):

$$\Omega(r,\theta) = \Omega_0 \cdot \frac{R_{1/2}^2}{R_{1/2}^2 + (r\sin\theta)^2} \tag{6.1}$$

where Ω_0 is the limit of the angular velocity on the axis and $R_{1/2}$ is used as a free pa-

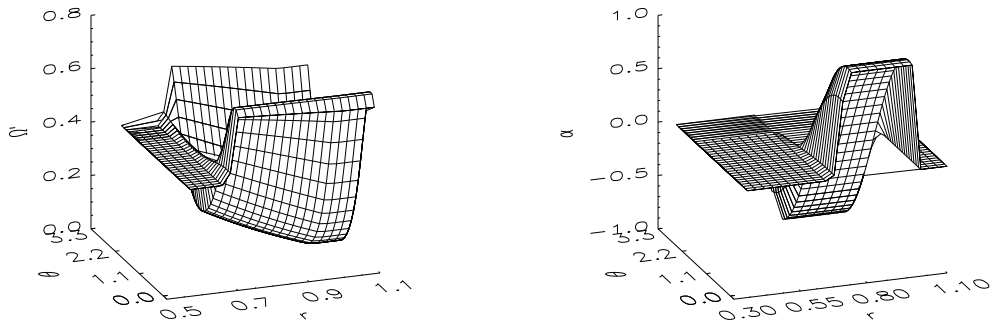

Figure 6.1: The angular velocity $\Omega^{'}$(left panel) and α term (right panel) used in the simulations. These functions are plotted against the spherical coordinates r and θ, so that the lines parallel to the θ axis represent spherical surfaces (i.e. constant r), while lines parallel to the r axis represent cuts of the sphere by a surface at constant θ. In particular the lines at $\theta = 0$ and π represent the rotation axis.

rameter, it represents the radius at which, on the equatorial plane, the angular velocity is reduced by a factor 2 with respect to Ω_0. We note that this particular Ω profile is depending on the square of the cylindrical distance $\varpi = r \cdot \sin\theta$.

Following the Raedler approach [4] we have rewritten the fluid velocity in a frame of reference which is comoving with the equator of the PNS, whose own velocity in the original static frame is $\tilde{\Omega} = \Omega^{\rm eq}_{\rm surf} = \Omega(1, \pi/2)$, where we have used 1 for the radius of the star because we use the stellar radius as the unit of length. The fluid velocity in the new frame is then $\Omega^{'} = \Omega - \tilde{\Omega}$. Finally, we have modified this profile by adding a region of rigid rotation near to the inner radial boundary (this region was introduced mainly for numerical reasons). The profile used is shown in the left panel of figure 6.1.

As regards the α term we use an angular profile proportional to $\cos\theta$, which ensures the change of sign between the northern and southern hemisphere and at the same time has a non zero value on the axis, as happens instead in the solar dynamo model, where α is taken to be proportional to $\cos\theta \cdot \sin^2\theta$ (see e.g. Jouve et al. [1]). For the radial dependence of the α term we use a simple combination of error functions in order to have a non zero α only in the NFI zone. The profile that we use for α is shown in the right panel of figure 6.1.

Finally we have to specify the diffusivity in order to complete the model. For η we use a profile which does not depend on θ, while along the radius we three different zones, using one value of η for the CI zone, another value for the NFI zone, and third one for the additional shell that we put outside the stellar surface (see the discussion at the end of the previous Chapter, in Section 5.4).

6.2 The strategy

Once the set-up is ready we plan to run several simulations, exploring the two dimensional phase space (C_α, C_Ω) in order to find what is the minimum threshold value of C_α for dynamo excitation, which are the zones where the dynamo gives a constant magnetic field or an oscillating one, what is the final intensity of the magnetic field outside the star, what is the ratio between the toroidal and poloidal components and how does this vary in space and time. We also want to analyse the difference between using local and global quenching for the α-effect.

Some of these things have already been analysed in our one dimensional model (see Chapter 3) and therefore for these we will also make a comparison between the two models, paying attention to comparing similar set-ups. In fact in this version of the axisymmetric PNS calculation we are not using the η-quenching and we are not considering a moving boundary between the two instability zones, therefore we should compare only with configuration A and B of the one dimensional model (see table 3.1 in Section 3.4.1).

6.3 Preliminary results

As mentioned previously, this analysis is still ongoing and no definitive results have been obtained yet, nevertheless we want to present here some preliminary results, even if these only concern one configuration.

In this configuration the boundary between the CI zone and the NFI zone is placed at $R_{\rm inst} = 0.8$; the diffusivity has the same value in these two zones: $\eta_{\rm CI} = \eta_{\rm NFI} = 1.0$, while $\eta = 10.0$ in the outer shell; with α being non zero only in the NFI zone. As regards the Ω profile we choose $R_{1/2} = 0.7$ and we place the central rigid rotation zone at $r \leq 0.6$. Therefore there are four regions in total along the radial direction. The inner edge is placed at $r = 0.4$ and from there until $r = 0.6$ there is rigid rotation, zero α and $\eta = 1$; then from $r = 0.6$ to $r = 0.8$ the star begins to rotate differentially, this is the CI zone still with $\alpha = 0$ and $\eta = 1$; from $r = 0.8$ to $r = 1.0$ there is the NFI zone where $\alpha = 1$ and $\eta = 1$; finally in the range $r \in [1,\, 1.05]$ there is the additional shell where $\alpha = 0$, $\eta = 10$ and Ω is frozen to its value at the surface of the star.

We ran the simulation with $C_\alpha = 13$ and $C_\Omega = 10^3$. For these values of the parameters the dynamo is excited and in fact in figure 6.2 we can see that the total magnetic energy is increasing. Moreover we can see that the dynamo produced is an oscillating one. In figure 6.3 we show the evolution of the maximum of the magnetic field for each of the three components and it can be seen that all of the components are being amplified, the amplification factor however is quite modest and the final maximum field is 3 orders of magnitude smaller than the equipartition value. However we should remark here that the amplification process has not finished by the end of the run, in fact the simulation ends at $0.8\,\tau_{\rm D}$, where $\tau_{\rm D}$ is the diffusion time, whose value is in the range $0.75 - 2.5$ s for typical PNSs (see Chapter 3, Section 3.2). Therefore the magnetic field evolution is followed for about $0.6 - 2.0$ s, while the instabilities should only disappear after 40 s and

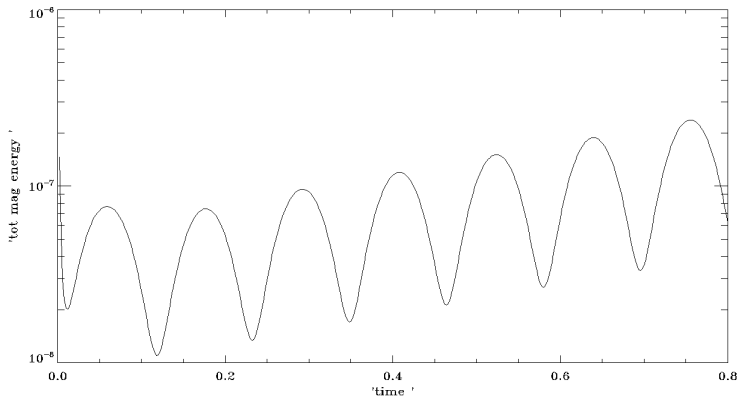

Figure 6.2: Time evolution of the total magnetic energy. The dynamo is excited immediately after the beginning of the simulations; the magnetic field is oscillating but secularly increasing.

so we expect to have a larger amplification factor if we run a longer simulation, although with this configuration the growth remains slow.

In figures 6.4–6.7 we show contour plots of each of the magnetic field components at different times. In the figures we also show the boundary between the two instability zones (with a dashed line) and the stellar surface (with a long dashed line); the two thick solid lines show the edges of the computaional domain. We can see that during each cycle, the magnetic field maxima move from the pole towards the equator. In particular for the r component they remain inside the NFI zone, for the θ component they are located along the boundary between the two zones and for B_ϕ they appear in the NFI zone at high latitudes, and then as time passes, they move towards smaller latitudes and radii, eventually overshooting into the CI zone.

This analysis will continue as outlined in the previous Section, firstly by repeating these calculations for other values of C_α and C_Ω and subsequently by studying the magnetic field topology and intensity, in order to confirm or refute the idea that the observed range in neutron star magnetic field intensity is due to different dynamo actions during the PNS phase.

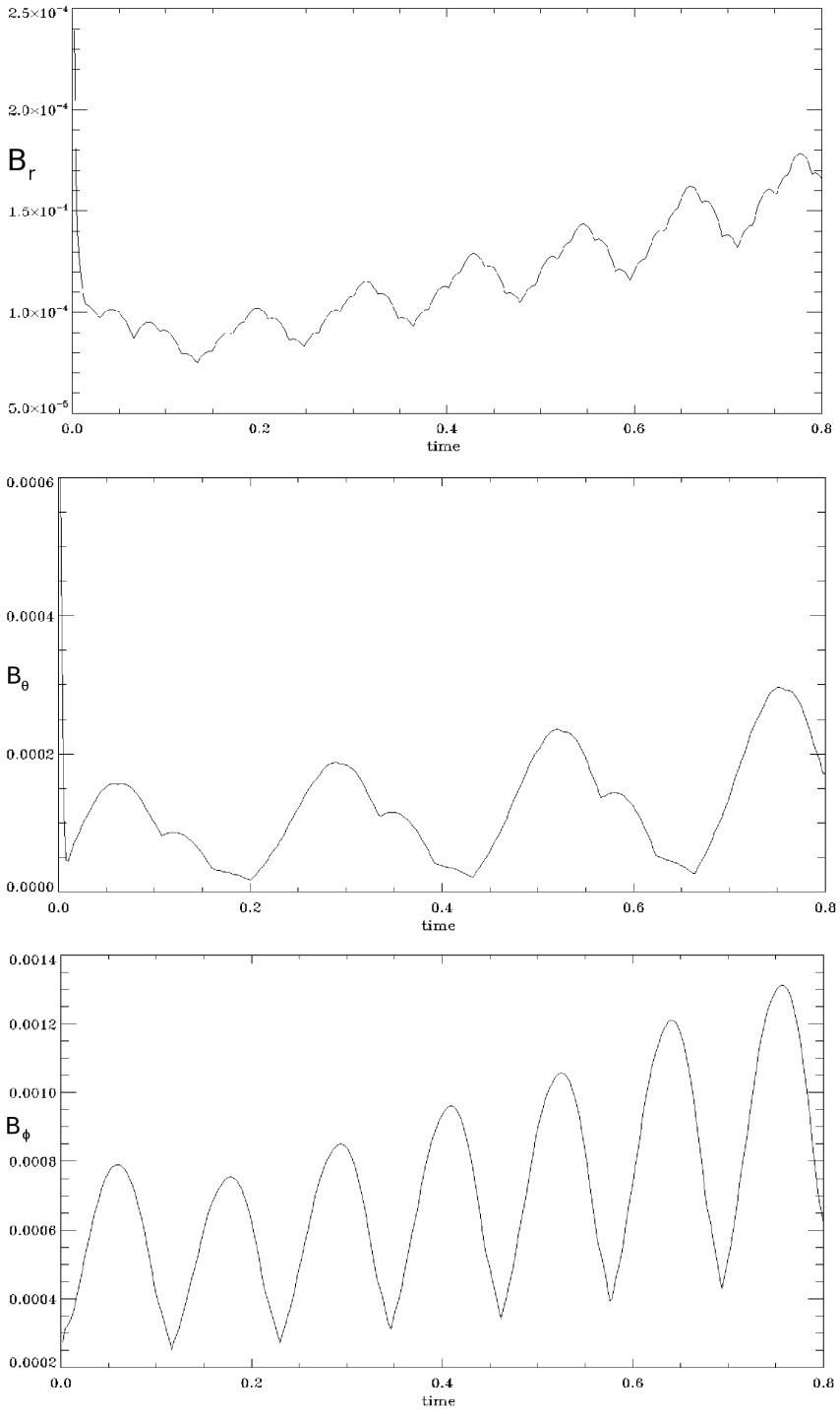

Figure 6.3: Maximum of the magnetic field for each of the three components: B_r, B_θ and B_ϕ, from top to bottom. As for the total magnetic energy, the oscillations are superimposed on an increasing trend which has a much longer timescale.

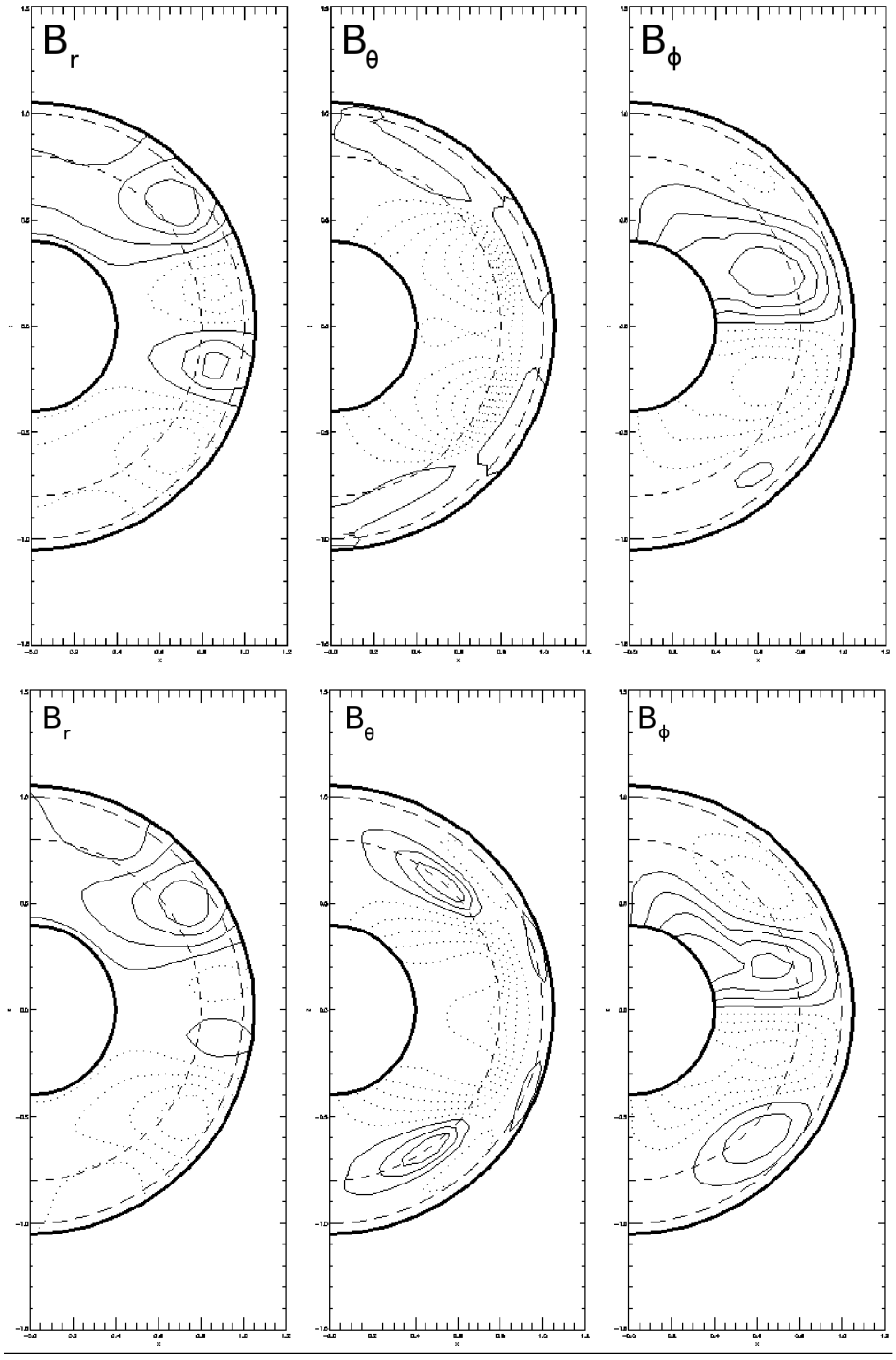

Figure 6.4: Contour plots of the magnetic field at succesive times ($0.430\,\tau_{\rm D}$ for the top panel and $0.454\tau_{\rm D}$ for the bottom one). Dotted lines represent vectors pointing in the negative direction, while continuous lines represent vectors pointing in the positive direction. E.g. a dotted line for B_r means that at that location B_r is directed inwards, while a continuous line for B_θ means that at that location B_θ is directed downwards.

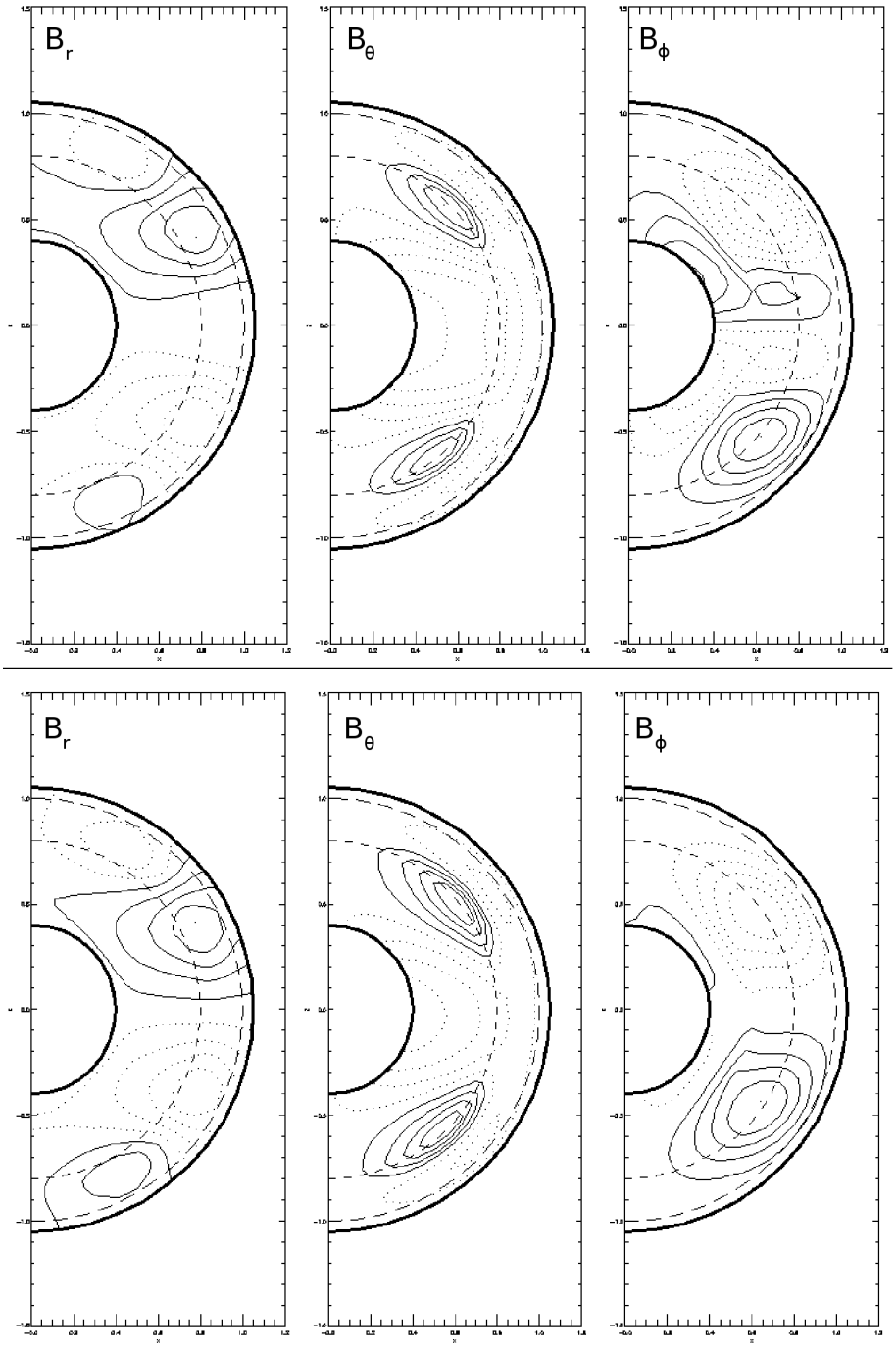

Figure 6.5: Continuation of figure 6.4 for time $0.466\,\tau_{\mathrm{D}}$ (top panel) and $0.478\,\tau_{\mathrm{D}}$ (bottom panel).

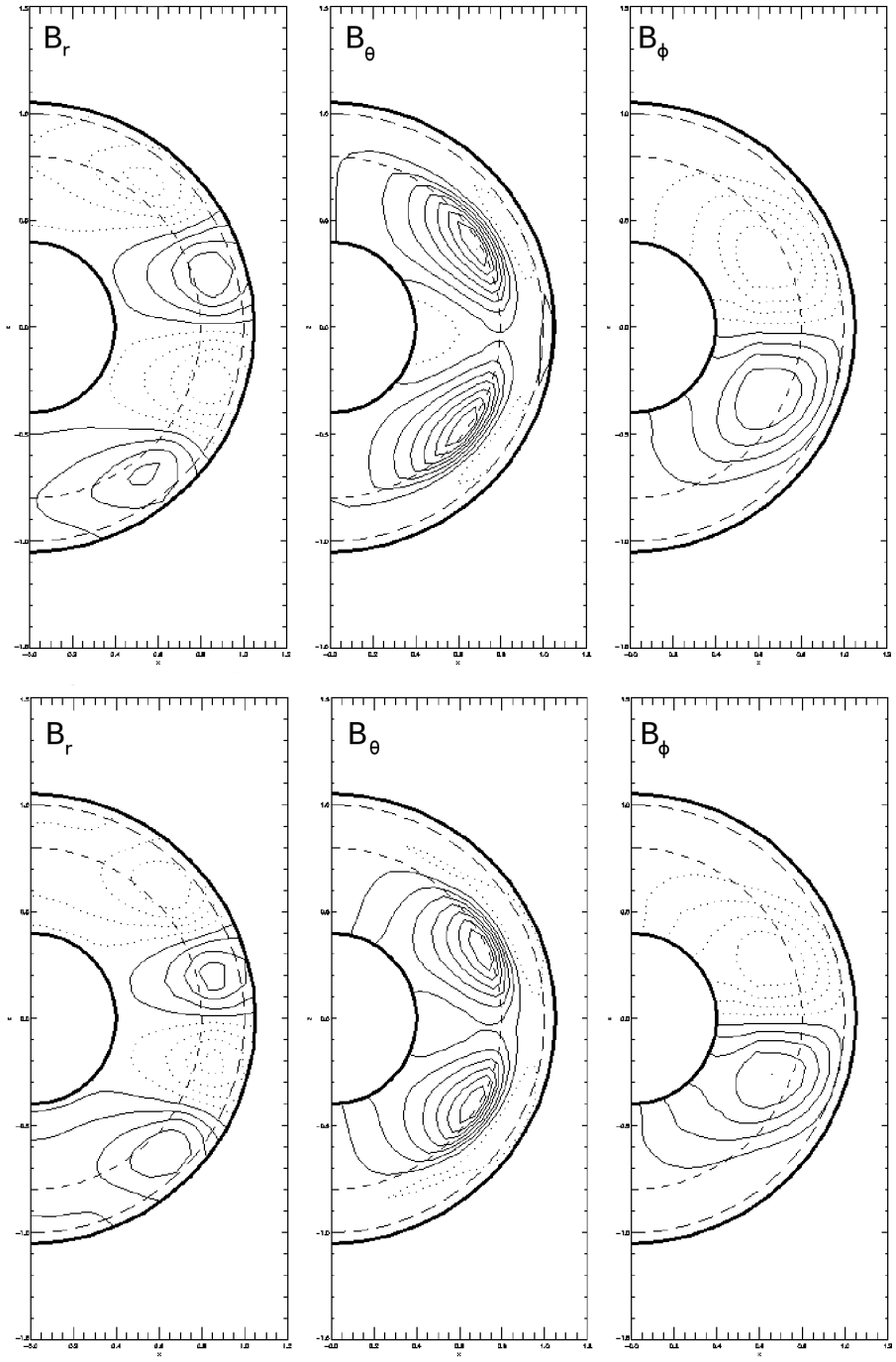

Figure 6.6: Further continuation of figure 6.4 for time $0.512\,\tau_{\rm D}$ (top panel) and $0.576\,\tau_{\rm D}$ (bottom panel).

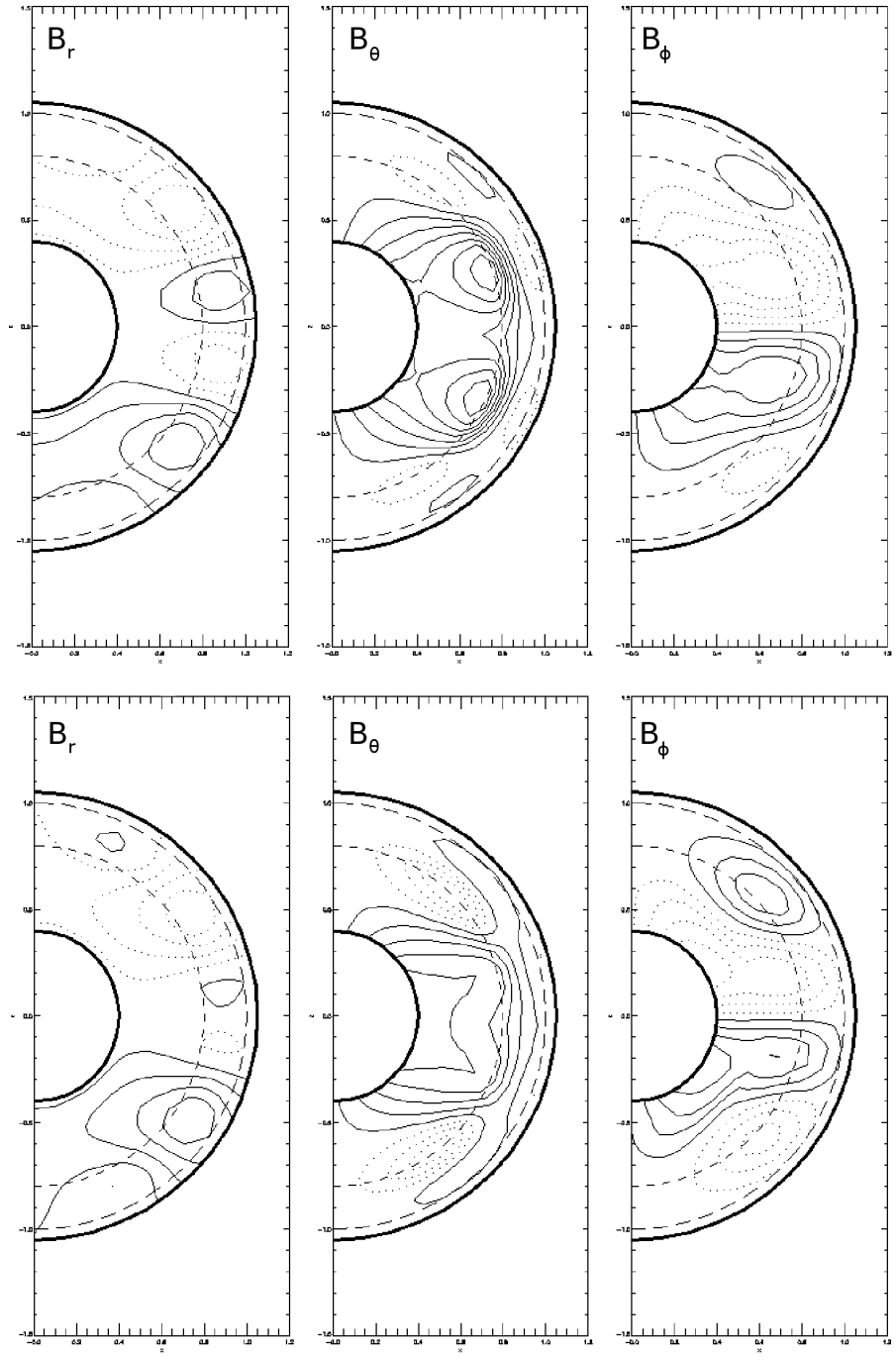

Figure 6.7: Further continuation of figure 6.4 for time $0.560\,\tau_{\mathrm{D}}$ (top panel) and $0.580\,\tau_{\mathrm{D}}$ (bottom panel).

Bibliography

[1] Jouve L., Brun A.S., Arlt R. et al. 2008, A&A, 483, 949

[2] Komatsu H., Eriguchi Y. & Hachisu I. 1989, MNRAS, 237, 355

[3] Miralles J.A., Pons J.A. & Urpin V. 2004, A&A, 420, 245

[4] Raedler K.-H. 1986, AN, 307, 89

[5] Villain L., Pons J.A., Cerda-Duran P. & Gourgoulhom 2004, A&A, 418, 283

Chapter 7

Conclusions

In this thesis we have treated the problem of magnetic field–plasma interaction applied to two different astrophysical systems: proto-neutron stars (Chapter 3) and accretion discs around magnetised neutron stars (Chapter 4). In both cases we have considered the plasma to be collisional and we have described the interaction in the context of the MHD single fluid model (hapter 2). The equations have then been simplified according to the way in which we have decided to describe these systems and have then been solved by means of numerical simulations. In particular the main approximation which we have made in both of the two cases is the kinematic approximation, in which the plasma motions are not evolved in time and the effect of the Lorentz force on the fluid is neglected. However we plan to remove this approximation for the next steps of our analysis. We are planning to continue the studies described in this thesis with more elaborate models. As part of this project we have modified a sophisticated parallel code, ZEUS-MP (Chapter 5), which we plan to use for analysing mean field dynamos in proto-neutron stars and we have already started this new study (Chapter 6).

The results obtained in the two stages of this work have already been described in Section 3.5, for the mean field dynamos in proto-neutron stars (PNSs), and in Section 4.6, for accretion discs around magnetised neutron stars. Here we just want to highlight the most important points.

Dynamos in PNSs

The mean field dynamos in PNSs have been studied in a one dimensional model. Using such a simplified model has the advantage of leading to a very simple expression for the induction equation, allowing us to include the non-linearities related to α- and η-quenching and a moving boundary for the instability which is generating the dynamo, as well as performing a parametric investigation which would have been impossible if it involved fully 3D simulations.

We have found that the dynamo is active whenever the C_α dynamo number is larger

than a certain threshold value or, in terms of the spin period of the PNS in our model, when $P > P_{\rm c} = 0.6$ s, with the critical period being decreased for increasing differential rotation. When the dynamo is active, the magnetic field is initially exponentially amplified and then subsequently saturates to a constant value, or oscillates in the case of an oscillating dynamo. We have found that the final intensity of the magnetic field can be written in terms of the dynamo numbers, one related to the spin period and the other to the differential rotation, and in all of the cases considered here the functional form of this dependence was a power law. Furthermore the coefficients of this power law were the same for all but one of the analysed configurations. These results suggest to us the idea that the different magnetic fields observed at the birth of neutron stars can be explained in terms of basic quantities like the rotation period and the differential rotation and are therefore promising for building up a piece of the puzzle in the unification of different classes of neutron stars.

Accretion discs

Nowadays there are spectacular three dimensional simulations of the full MHD equations describing the accretion process. However in this kind of analysis the output of the simulations is the result many complex and interacting mechanisms. Our kind of work aims at providing conceptual tools for decomposing such complex results. For doing this we follow the approach of using a succession of simplified models, becoming progessively more elaborate, introducing at every step a new feature. Here we have presented our first model where we have studied the influence of the velocity field and the magnetic diffusivity on the poloidal component of the magnetic field, by solving the induction equation in order to find a stationary solution.

With our two dimensional numerical calculations we have found that the poloidal component of the magnetic field is very different from a pure dipole field, being dragged inwards by the plasma motion. By extending the concept of the magnetic Reynolds number, we have introduced a magnetic distortion function, which measures the local amount of distortion of the magnetic field away from dipolar. We have further found that when the magnetic distortion function has a jump through the disc, because of a large change in the velocity or in the diffusivity, we observe a completely new feature, i.e. at the same location the magnetic field is amplified. We are now aiming at solving also the equation for the toroidal field and when all of the magnetic field components will be at hand it will be possibile to calculate important quantities like the location of the inner edge of the disc and the total magnetic torque. This in turn will help in getting a better understanding of such intricated topics as the spin history of millisecond pulsars and X-ray pulsars.